FELDSPAR POLYMORPHS: DIVERSITY, COMPLEXITY, STABILITY

© 2020 г. S. V. Krivovichev[1, 2, *]

[1]*Nanomaterials Research Centre, Kola Science Centre RAS, Fersman st., 14, Apatity, 184209 Russia*
[2]*Saint Petersburg State University, University Emb., 7/9, Saint Petersburg, 199034 Russia*
**e-mail: s.krivovichev@ksc.ru*

Received May 26, 2020; Revised June 11, 2020; Accepted June 17, 2020

The various aspects of polymorphism in the feldspar family of minerals are considered with special emphasis upon their structural diversity and complexity. The feldspar family is defined as consisting of valid minerals and unnamed or conditionally named mineral phases with the general formula $M^{n+}[T_4^{k+}O_8]$, where n is the average charge of the M^{n+} cation (n = 1–2; $M^{n+} = Na^+$, K^+, Rb^+, $(NH_4)^+$, Ca^{2+}, Sr^{2+}, Ba^{2+}), k is the average charge of the T^{k+} cation ($k = 4 - n/4$; $T^{k+} = Be^{2+}$, Zn^{2+}, Al^{3+}, B^{3+}, Fe^{3+}, Si^{4+}, As^{5+}, P^{5+}). There are twenty-nine valid mineral species known to date that can be assigned to the feldspar family. Maskelynite is the natural X-ray amorphous feldspar polymorph (glass) with the plagioclase composition. All feldspar polymorphs can be classified into two groups: those containing T atoms in tetrahedral coordination only and those containing T atoms in non-tetrahedral coordination. There are four basic topologies of the feldspar-family tetrahedral networks: **fsp** (3D; feldspar *sensu stricto*; eleven mineral species), **pcl** (3D; paracelsian; seven mineral species), **bct** (3D, svyatoslavite; two mineral species), and **dms** (2D; dmisteinbergite; six mineral species). There are three minerals that contain T atoms in exclusively octahedral (sixfold) coordination and crystallize in the hollandite structure type. The high-pressure polymorphism for the structures with the **fsp** and **pcl** topologies is controlled by the distinction of these topologies as flexible and inflexible, respectively. The analysis of structural complexity by means of the Shannon information theory indicates the following general trends: (i) structural complexity decreases with the increasing temperature; (ii) kinetically stabilized metastable feldspar polymorphs are topologically simpler than the thermodynamically stable phases; (iii) the high-pressure behavior of feldspar-family structures does not show any obvious trends in the evolution of structural complexity. The feldspar polymorphism includes a number of structural phenomena: (i) coordination changes of intra- and extraframework cations; (ii) topological reconstructions, including changes in dimensionality; (iii) cation ordering, including Al/Si and M-cation ordering in solid solutions, resulting in the chemical stabilization of particular structure types and the formation of incommensurately modulated structures (in plagioclases); (iv) displacive distortions involving tilting of tetrahedra and rotations of crankshaft chains; (v) amorphization. The observed structural phenomena are controlled by temperature, pressure (including shock-induced transformations) and crystallization kinetics that may stabilize metastable phases with unique crystal structures.

Keywords: feldspar, crystal structure, polymorphism, structural complexity, phase transition, metastability, structural topology, high pressure, high temperature.

DOI: 10.31857/S0869605520040036

1. INTRODUCTION

Feldspars constitute one of the most important groups of rock-forming minerals and there have been many detailed works devoted to their composition, crystal structure, stability, gene-

sis, petrological and geochemical significance, high-temperature and high-pressure behavior, microstructures, etc., partially summarized in recent monographs and handbooks (Smith, Brown, 1988; Feldspars..., 1994; Deer et al., 2001; Minerals..., 2003). However, a number of important discoveries in the field of feldspar crystal chemistry have been made over the past decade, including findings of metastable feldspar polymorphs in different geochemical and cosmochemical environments (Nestola et al., 2010; Németh et al., 2013; Ma et al., 2013; Kotková et al., 2014; Fintor et al., 2013, 2014; Ferrero et al., 2016, 2018; Ferrero, Angel, 2018), discoveries of new feldspar modifications in synchrotron cold compression experiments (Pakhomova et al., 2017, 2019, 2020; Gorelova et al., 2019), studies of incommensurately modulated plagioclases (Xu, 2015; Boysen, Kek, 2015; Xu et al., 2016; Fredrickson, Fredrickson, 2016; Jin, Xu, 2017a, b; Jin et al., 2019, 2020), and discoveries of new feldspar-family minerals (Rao et al., 2014, 2015; Tschauner, Ma, 2017; Ma et al., 2018; Shchipalkina et al., 2019).

The aim of the present review is to provide a general summary of the feldspar polymorphism, focusing primarily on the results obtained for natural samples (including high-pressure and high-temperature polymorphs obtained during studies of natural samples) and thus leaving aside a systematic overview of synthetic feldspar chemistry. However, we shall use the information on synthetic analogues of feldspars, where appropriate and necessary for the understanding the behavior and stability of their natural counterparts.

The review is organized as follows. First, we provide a general definition of a member of the feldspar family and outline its chemical diversity. The adopted definition is then applied to the chemical classification, providing information on the actual and potential chemical diversity. Second, we discuss structural and topological aspects of feldspars and suggest a tentative crystal chemical classification scheme for the family as a basis for further systematic analysis, which is the subject of the major body of the review. The analytical part of the paper is concerned with the structural complexity analysis of the feldspar polymorphs using the methodology recently developed in (Krivovichev, 2012, 2013a, b, 2014a, 2016a, b, 2018). At the end, we summarize the basic points of the review and provide some ideas on further perspectives in the studies of polymorphism in the feldspar family.

2. CLASSIFICATION

2.1. Feldspar family: a definition

One of the classical authors in the feldspar mineralogy Paul Ribbe defined natural feldspars as "...MT_4O_8 aluminosilicates whose structures are composed of corner-sharing AlO_4 and SiO_4 tetrahedra linked in an infinite three-dimensional array" (Ribbe, 1994). This definition specifies feldspars as framework silicates with the particular stoichiometry, i.e. establishing the M : T ratio as 1 : 4 (here M and T are extraframework and framework-forming cations, respectively). However, it is easy to see that this definition allows to consider anorthite, $CaAl_2Si_2O_8$, and its polymorph svyatoslavite (based upon a non-feldspar tetrahedral framework) as feldspars, whereas dmisteinbergite, a layered anorthite polymorph, which has the same chemical composition, cannot be considered as a feldspar-family member.

Bruno and Pentinghaus (1974) provided for the feldspars the following general formula: $(M^{+}_{x}M^{2+}_{1-x})[T^{3+}_{2-x}T^{4+}_{2+x}O_8]$, where $0 \le x \le 1$, M^{+} = Na, K, Rb, Tl, NH_4; M^{2+} = Ca, Sr, Ba, Pb; T^{3+} = Al, B, Ga, Fe; T^{4+} = Si, Ge. Though the range of possible framework cations had been extended by divalent and pentavalent cations (see below), the important feature of the feldspar stoichiometry implied by the formula is the M : T ratio equal to 1 : 4.

According to Mills et al. (2009), "...mineral families apply to groups and/or supergroups having similar structural and/or chemical features that make them unique". We define the *feldspar family* as consisting of mineral species with the general formula $M^{n+}[T^{k+}_4O_8]$, where n is the average charge of the M^{n+} cation (n = 1–2; $M^{n+} = Na^{+}$, K^{+}, Rb^{+}, $(NH_4)^{+}$, Ca^{2+}, Sr^{2+},

Ba^{2+}), k is the average charge of the T^{k+} cation ($k = 4 - n/4$; $T^{k+} = Be^{2+}$, Zn^{2+}, Al^{3+}, B^{3+}, Fe^{3+}, Si^{4+}, As^{5+}, P^{5+}). The feldspar-family member has a crystal structure based upon d-dimensional network of (TO_m) coordination polyhedra sharing O atoms. For the mineral species known so far, $d = 2$ or 3 (layers or frameworks), and $m = 4$ or 6 (coordination of the T atoms in minerals is either tetrahedral or octahedral). The chemical diversity of the M and T atoms is not restricted to the elements mentioned above, but may be extended with new mineralogical discoveries. The M : T ratio of 1 : 4 should correspond to the ratio of the total numbers of the M and T sites in the crystal structure (taking into account their multiplicities). In general, feldspar-family minerals (FFMs) do not contain H_2O as a mineral-defining constituent, but we include into the family hydrated structures with the same topology as observed in the anhydrous FFMs. Thus, we consider cymrite, $Ba[Al_2Si_2O_8](H_2O)$, and "K-cymrite", $K[AlSi_3O_8](H_2O)$, as belonging to the feldspar family. There are several synthetic compounds with the paracelsian topology [including "K-paracelsian", $K[AlSi_3O_8](H_2O)$ (Boruntea et al., 2019)] that contain well-defined structural H_2O groups (Dordević, 2011, and references therein).

2.2. Chemical classification

Table 1 provides the list of currently known natural FFMs that satisfy the definition given above, along with their polymorphs obtained by applying high-pressure and high-temperature conditions to the natural crystals. From the chemical point of view, FFMs can be subdivided into aluminosilicates (nineteen valid and one potentially new mineral species), borosilicates (four mineral species), ferrisilicates (one mineral species), aluminoarsenates (one mineral species), and beryllophosphates (three mineral species). In total, the feldspar family includes twenty-nine mineral species accepted by the International Mineralogical Association (IMA) as of May 1st, 2020.

In some mineralogical classifications, the minerals of the banalsite group are considered as belonging to the feldspar family (Minerals..., 2003). The group contains three mineral species with the general formula $Na_2M^{2+}[Al_4Si_4O_{16}]$, where M = Ca for lisetite, Sr for stronalsite, and Ba for banalsite. Though the chemical formula can be considered as a sum of two feldspar components ($2Na[AlSi_3O_8] + M^{2+}[Al_2Si_2O_8]$), the overall M : T ratio is 3 : 8 instead of 1 : 4 required by the definition of FFMs. Taking into account their structural and chemical features, we suggest that the banalsite-group minerals are considered as members of the feldspathoid family.

2.3. Structural classification

By definition, the crystal structure of FFMs is based upon a d-dimensional $[T_4O_8]$ network of polymerized (TO_m) coordination polyhedra with M^{n+} cations located within the framework cavities. The crystal structure is therefore dominated by the T–O network of strong chemical bonds that makes it natural to consider the coordination of the T atoms as a first parameter for the structural classification of FFMs. At the current state of knowledge, there are three different coordination numbers of T atoms, CN(T), known: 4 (tetrahedral geometry), 5 (trigonal bipyramidal or square pyramidal geometry), and 6 (octahedral geometry).

According to the CN(T) values, the feldspar polymorphs can be classified into three major groups: (i) tetrahedral structures, CN(T) = 4, (ii) octahedral structures, CN(T) = 6, (iii) structures with mixed coordination of T atoms. We note that natural feldspar polymorphs are known for the first two groups only, whereas the third group contains only metastable polymorphs obtained by means of cold compression of natural crystals.

In the following, we provide a systematic description of the structural topologies and structure types observed for the feldspar polymorphs listed in Table 1.

Table 1. Crystallographic data on natural feldspar polymorphs
Таблица 1. Кристаллографические данные для природных полиморфов полевых шпатов

Chemical formula	Name/conditions	Top.	CN(T)	Space group	*a* [Å]/α [°]	*b* [Å]/β [°]	*c* [Å]/γ [°]	*V*, Å^3	Ref.
				Aluminosilicates					
$NaAlSi_3O_8$	Albite	**fsp**	4	$C\bar{1}$	8.161/93.5	12.875/116.5	7.110/90.2	669.8	1
	"Monalbite" (1253 K)	**fsp**	4	$C2/m$	8.274/90	12.991/116.1	7.144/90	689.4	1
	"Albite-II" (13.5 GPa)	–	4, 6	$P\bar{1}$	6.585/63.6	6.885/64.2	7.022/75.6	256.1	2
	"Albite-III" (17.5 GPa)	–	4, 5, 6	$P\bar{1}$	6.983/113.7	6.906/92.7	11.729/71.1	487.9	2
	Kumdykolite	**bct**	4	$P12_11$?	8.24/90	8.68/90	4.84/90	346.2	3
	Lingunite	**hol**	6	$I4/m$	9.263/90	= *a*/α	2.706/90	232.2	4
$KAlSi_3O_8$	Sanidine	**fsp**	4	$C2/m$	8.605/90	13.031/116.0	7.177/90	723.3	5
	Orthoclase	**fsp**	4	$C2/m$	8.554/90	12.970/116.0	7.207/90	718.7	6
	Microcline	**fsp**	4	$C\bar{1}$	8.592/90.62	12.963/116.0	7.222/87.67	722.7	5
	"Microcline-II"	–	4, 6	$P\bar{1}$	6.308/74.1	6.765/85.0	7.029/64.8	260.9	2
	Kokchetavite	**dms**	4	hex?	5.27/90	= *a*/α	7.82/120	188.1	7
	Liebermannite	**hol**	6	$I4/m$	9.15/90	= *a*/α	2.74/90	229	8
	"Liebermannite-II" (25.1 GPa)	**hol**	6	$I112/m$	9.147/90	8.783/90	2.651/91.2	213	9
$KAlSi_3O_8 \cdot H_2O$	"K-cymrite"	**dms**	4	$P6/mmm$	5.335/90	= *a*/α	7.706/120	189.9	10
$RbAlSi_3O_8$	Rubicline	**fsp**	4	$C\bar{1}$	8.81/90.3	13.01/115.7	7.18/88.2	741	11
$(NH_4)AlSi_3O_8$	Buddingtonite	**fsp**	4	$C2/m$	8.804/90	13.024/116.1	7.183/90	735.0	12
$CaAl_2Si_2O_8$	Anorthite	**fsp**	4	$P\bar{1}$	8.173/93.1	12.869/115.9	14.165/91.3	1336.4	13
	"Ca-feldspar"	**fsp**	4	$C\bar{1}$	8.152/93.3	12.917/116.4	7.126/88.7	671.2	14
	"Anorthite-II" (2.5 GPa)	–	4	$I\bar{1}$	8.082/92.8	12.767/115.8	14.032/91.7	1300.3	15
	"Anorthite-II" (514 K)	–	4	$I\bar{1}$	8.194/93.1	12.878/115.1	14.171/91.5	1350.6	16
	"Anorthite-III" (11.1 GPa)	–	4, 5	$P\bar{1}$	7.645/96.7	11.944/109.6	12.906/80.2	1091.9	2
	Dmisteinbergite	**dms**	4	$P312$	5.112/90	= *a*/α	14.742/120	333.7	17
	Svyatoslavite	**bct**	4	$P12_11$	8.220/90	8.951/90.0	4.828/90	355.2	18
	Stöfflerite	**hol**	6	$I4/m$	9.255/90	= *a*/α	2.745/90	235.1	19
$BaAl_2Si_2O_8$	Celsian	**fsp**	4	$I2/c$	8.622/90	13.078/115.1	14.411/90	1471.5	20
	Hexacelsian	**dms**	4	$P6_3/mcm$	5.292/90	= *a*/α	15.557/120	377.3	21
	Paracelsian	**pcl**	4	$P2_1/c$	8.576/90	9.573/90.2	9.068/90	744.4	22
	"Paracelsian-II" (14.2 GPa)	–	4, 5	$P2_1/c$	8.897/90	8.837/90.1	6.904/90	542.9	22
	"Paracelsian-III" (28.5 GPa)	–	4, 5, 6	$Pna2_1$	5.434/90	8.743/90	9.685/90	460.1	22
	"Paracelsian-IV" (32.4 GPa)	–	4, 5, 6	Pn	8.742/90	5.387/91.4	9.634/90	453.5	22
$BaAl_2Si_2O_8 \cdot H_2O$	Cymrite	**dms**	2	$P2_1$	5.335/90	36.926/90	7.693/90	1515.6	23

Table 1. (Contd.)

Chemical formula	Name/conditions	Top.	CN(T)	Space group	a [Å]/α [°]	b [Å]/β [°]	c [Å]/γ [°]	V, Å^3	Ref.
$SrAl_2Si_2O_8$	Slawsonite	**pcl**	4	$P2_1/c$	8.326/90	9.344/90.3	8.888/90	691.5	24
				Borosilicates					
$NaBSi_3O_8$	Reedmergnerite	**fsp**	4	$C\bar{1}$	7.839/93.3	12.373/116.4	6.808/92.0	589.2	25
$CaB_2Si_2O_8$	Danburite	**pcl**	4	*Pnam*	8.038/90	8.752/90	7.730/90	543.8	26
	"Danburite-II" (25.4 GPa)	–	4, 5	*Pnam*	6.354/90	7.952/90	8.011/90	404.8	27
	"Danburite-III" (25.4 GPa)	–	4, 6	$P\bar{1}$	5.479/91.7	5.532/104.6	6.681/95.6	194.7	27
	"Danburite-IV" (32.0 GPa)	–	4, 5	$P2_1/c$	7.999/90	7.870/89.8	6.249/90	393.4	27
$SrB_2Si_2O_8$	Pekovite	**pcl**	4	*Pnma*	8.155/90	7.919/90	8.921/90	576.1	28
	"Pekovite-II" (29.4 GPa)	–	4, 5	*Pnma*	6.697/90	7.869/90	8.159/90	430.0	29
	"Pekovite-III" (33.3 GPa)	–	4, 6	$P\bar{1}$	5.44/93.3	5.60/104.2	6.72/93.4	198	29
$BaB_2Si_2O_8$	maleevite	**pcl**	4	*Pnma*	8.141/90	8.176/90	9.038/90	601.6	28
	"Maleevite-II" (38.3 GPa)	–	4, 6	$P\bar{1}$	5.630/92.1	5.538/104.0	6.746/95.0	203.0	29
				Ferrisilicates					
$KFeSi_3O_8$	Ferrisanidine	**fsp**	4	$C2/m$	8.678/90	13.144/116.4	7.337/90	749.6	30
				Aluminoarsenates					
$K(Al,Zn)_2(As,Si)_2O_8$	Filatovite	**fsp**	4	$I2/c$	8.772/90	13.37/115.9	14.69/90	1549.1	31
				Beryllophosphates					
$CaBe_2P_2O_8$	Hurlbutite	**pcl**	4	$P2_1/c$	7.80/90	8.788/90.5	8.301/90	569.2	32
	"Hurlbutite-II" (74.5 GPa)	–	4, 5	$P2_1/c$	7.396/90	7.753/89.1	6.343/90	363.7	32
	"Hurlbutite-III" (83.2 GPa)	–	4, 5	$P2_1/c$	7.410/90	7.639/89.3	6.209/90	351.4	32
	"Hurlbutite-IV" (89.5 GPa)	–	6	$P\bar{1}$	6.203/80.1	7.163/85.2	7.865/77.6	335.8	32
$SrBe_2P_2O_8$	Strontiohurlbutite	**pcl**	4	$P2_1/c$	8.426/90	8.998/90.1	8.005/90	606.9	33
$BaBe_2P_2O_8$	Minjangite	**dms**	4	$P6/mmm$	5.030/90	= a/α	7.467/120	164.0	34

References: (1) Winter et al., 1979; (2) Pakhomova et al., 2020; (3) Hwang et al., 2009; (4) Gillet et al., 2000; (5) Kroll, Ribbe, 1987; (6) Colville, Ribbe, 1968; (7) Hwang et al., 2004; (8) Ma et al., 2018; (9) Ferroir et al., 2006; (10) Fasshauer et al., 1997; (11) Teerstra et al., 1998; (12) Kimball, Megaw, 1974; (13) Wainwright, Starkey, 1971; (14) Wadoski-Romejin, Armbruster, 2013; (15) Angel, 1988; (16) Ghose et al., 1993; (17) Zolotarev et al., 2019; (18) Krivovichev et al., 2012; (19) Tschauner, Ma, 2017; (20) Griffen, Ribbe, 1976; (21) Galuskina et al., 2017; (22) Gorelova et al., 2019; (23) Bolotina et al., 2010; (24) Griffen et al., 1977; (25) Fleet, 1992; (26) Phillips et al., 1974; (27) Pakhomova et al., 2017; (28) Pautov et al., 2004; (29) Gorelova et al., unpublished; (30) Shchipalkina et al., 2019; (31) Filatov et al., 2004; (32) Pakhomova et al., 2019; (33) Rao et al., 2014; (34) Rao et al., 2015.

3. TETRAHEDRAL STRUCTURES

3.1. Basic topologies

Tetrahedral structures are the most common for FFMs and constitute the basis for the mineral phases stable under ambient (atmospheric pressure and room temperature) conditions. The *d*-dimensional tetrahedral networks are based upon (TO_4) tetrahedra sharing O corners. Since each O atom can be shared among two tetrahedra only, the [T_4O_8] networks consist of 4-connected tetrahedra, i.e. each tetrahedron shares all four its corners with adjacent tetrahedra.

In order to describe the topology of tetrahedral networks in FFMs, we shall use the nodal representation where each (TO_4) tetrahedron is symbolized by a node and two nodes are connected by an edge if the respective tetrahedra share common O atom. This approach is well-known in inorganic crystal chemistry and has long been recognized in structural mineralogy of silicates in particular (Krivovichev, 2005, 2017, and references therein).

Fig. 1*a* shows the crystal structure of sanidine, K[$AlSi_3O_8$], projected along the *b* axis. The structure is based upon three-dimensional aluminosilicate framework with K^+ cations in the interstices. The basis of the framework is the so-called crankshaft chain of (Al, Si)O_4 tetrahedra (Fig. 1*b*) formed by successive polymerization of four-membered rings shown in Fig. 1d. Figs. 1c and e show nodal representations of the crankshaft chain and the four-membered ring, respectively, where each tetrahedron is replaced by a node and two nodes are linked if the respective tetrahedra share common corners. The nodal representation allows for the analysis of simplified structure models, which outline global topological features of the structures under consideration, whereas, for detailed geometrical analysis, the atomic configurations should be described in terms of bond lengths and interatomic angles.

There are four basic tetrahedral structural topologies observed in FFMs, which in the following are abbreviated using three-letter symbols: (i) feldspar topology (**fsp**); (ii) paracelsian topology (**pcl**); (iii) svyatoslavite topology (**bct**, due to its identity to the **BCT** topology in zeolites: see below); (iv) dmisteinbergite topology (**dms**). The **fsp**, **pcl** and **bct** topologies correspond to three-dimensional frameworks, whereas the **dms** topology is two-dimensional.

3.2. Feldspar topology

3.2.1. General description. As it was mentioned above, the basis of the **fsp** topology is a crankshaft chain of TO_4 tetrahedra. There is a whole family of minerals and synthetic compounds based upon different types of linkage of crankshaft chains, including natural and synthetic zeolites with important functional properties (Boruntea et al., 2019). The difference between the frameworks based upon crankshaft chains is in the rotational orientation of chains. Smith and Rinaldi (1962) developed an algebraic code in which the tetrahedra pointing up or down are denoted as U or D, respectively (Fig. 1*e*). Using this code, the 4-membered ring in the crankshaft chains oriented perpendicular to the chain extension is denoted as UUDD. The chains are linked together in such a way that 4-membered rings form a sheet consisting of 4- and 8-membered rings (Fig. 2*a*). Each framework based upon crankshaft chains has a unique combination of 8-membered rings characterized by particular algebraic codes. For instance, the sheet shown in Fig. 2*a* consists of two types of 8-membered rings with the codes UUUUDDDD and DUUDUDDU. Thus, the **fsp** framework can be considered also as based upon linkage of sheets of 4- and 8-membered rings. Smith (1978) derived a number of possible crankshaft-based frameworks that contain such sheets.

The important feature of the **fsp** framework topology is that the crankshaft chains are *twisted*, i.e. the adjacent perpendicular 4-membered rings in one chain are not directly superimposed in projection, but are rotated relative to each around the chain axis. This creates two possibilities of the linkage of the crankshaft chains: one that permits cooperative rotation of chains resulting of transformation of elliptical-shape 8-membered rings into regular octagons (Fig. 2*b, d*) and one that does not (Fig. 2*c*). The two types of linkage lead to the formation of

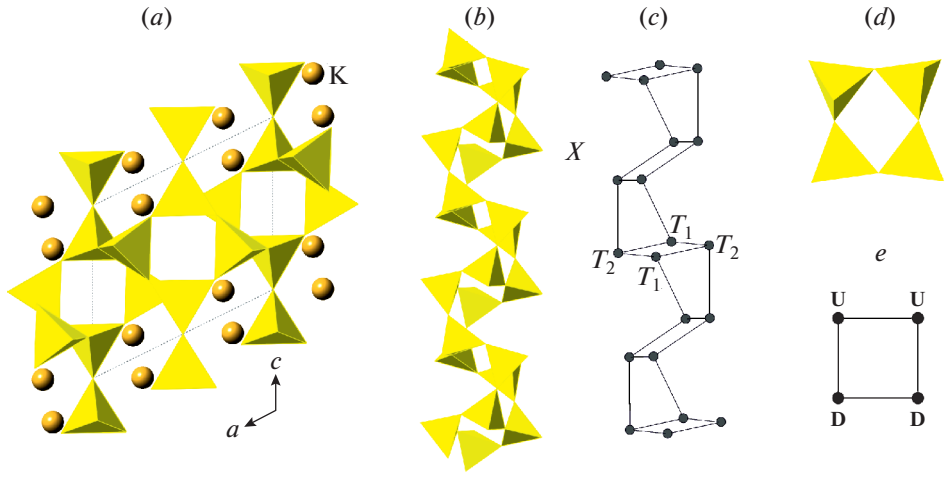

Fig. 1. The crystal structure of sanidine projected along the *b* axis (*a*), the crankshaft chain of tetrahedra (*b*) and its nodal representation (*c*), the four-membered tetrahedral rings (*d*) and its graph featuring the orientation of tetrahedra either up (**U**) or down (**D**) relative to the plane of the ring (*e*).
Рис. 1. Кристаллическая структура санидина в проекции вдоль оси *b* (*a*), цепочка типа карданных валов (*b*) и ее граф (*c*), четырехчленное тетраэдрическое кольцо (*d*) и его граф (*e*) с указанием ориентации тетраэдров вверх (up, **U**) или вниз (down, **D**) относительно плоскости слоя.

flexible and *inflexible* frameworks (Smith, 1968, 1974). The flexible frameworks are specific for zeolites based upon crankshaft chains that contain large pores able to accommodate H_2O and small organic molecules. The only known example of the topology with inflexible linkage is the **fsp** topology corresponding to the dense atomic configuration observed in feldspars *sensu stricto*. It should be emphasized that, despite the fact that protonated **fsp** frameworks can be obtained by ion-exchange (Müller, 1988), only small amount of H_2O may potentially be incorporated into the **fsp**-based solids reported so far (Kyono, Kimata, 2001).

3.2.2. Symmetry, nomenclature of sites and Al/Si distribution. There is a generally accepted nomenclature of the T and O sites in the ideal and distorted tetrahedral framework with the **fsp** topology that has its roots in the first determination of the crystal structure of sanidine by Taylor (1933). The maximal ideal symmetry (also called *topological* symmetry) of the **fsp** framework is described by the space group $C2/m$ [the structure type is also known as an aristotype following Megaw (1974)]. There are two symmetry-independent T sites denoted as T_1 and T_2. One of the T_1 sites is chosen as the primary site and is denoted as T_10 (the same also applies to the T_2 sites, from which one is denoted as T_20). The T_1 site, which is symmetrically equivalent to the T_10 site through the reflection in the *m* mirror plane is denoted as T_1m, whereas the T_1 site related to the T_10 site though the 2-fold rotation axis is denoted as T_1mc (the same applied to the T_2 sites). The notation of the T sites is shown in Figs. 3*a* and 4*a* that provide the projections of the **fsp** network onto (010) and (001) planes, respectively.

In the case of the ordered $[AlSi_3O_8]$ **fsp**-framework, Al is incorporated into one of the T_1 site [for the reasons outlined by Ribbe (1983b)], which leads to the reduction of symmetry from $C2/m$ to $C\bar{1}$. As a result, the T_1m site becomes symmetrically independent from the T_10 site. The general convention is that Al is concentrated in the T_10 site. Thus, the Al ordering in the $[AlSi_3O_8]$ **fsp**-framework results in the reduction of symmetry *at least* to the symmetry

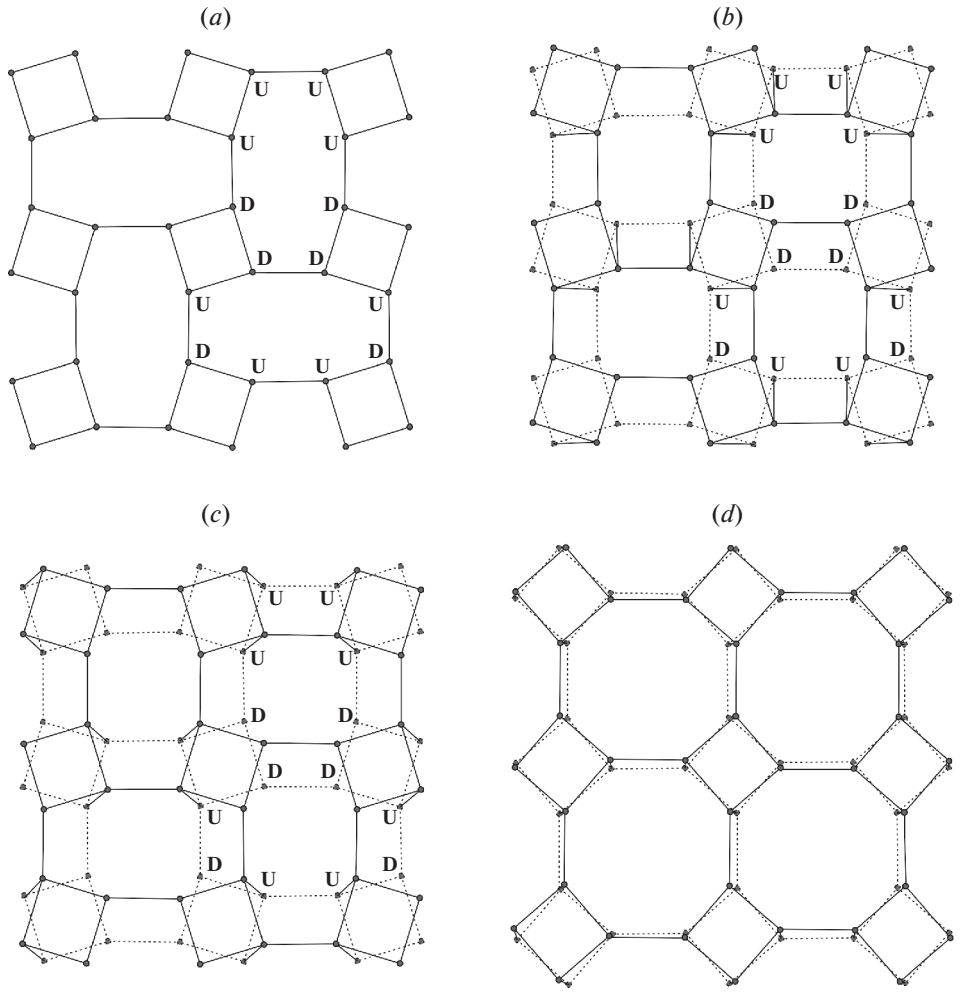

Fig. 2. The sheet of four- and eight-membered rings in the **fsp** framework topology with indicated orientations of tetrahedra relative to the plane of the sheet (*a*), two versions of linkage between the adjacent sheets of the kind shown in (*a*) (*b*, *c*; the sheet shown in dotted lines is located below the sheet shown in single lines). The sheet shown in (*b*) can be transformed into the sheet shown in (*d*) by cooperative rotations of the crankshaft chains, whereas the one shown in (*c*) cannot without the breaking of the edges between the nodes.

Рис. 2. Слой 4- и 8-членных колец в топологии fsp каркаса с обозначенной ориентацией тетраэдров относительно плоскости слоя (*a*), два различных варианта объединения соседних слоев типа (*a*) (*b, c*; слой, показанный точечными линиями, находится под слоем, показанным сплошной линией). Слой на рисунке (*b*) может быть преобразован в слой, показанный на рисунке (*d*), путем связанных поворотов карданновальных цепочек вокруг своей оси, тогда как слой, показанный на рисунке (*c*), в слой, показанный на рисунке (*d*) не преобразуется без разрыва связей между узлами сетки.

group $C\bar{1}$, which is the maximal symmetry group for such a configuration called *topochemical symmetry*. The distinction of topological and topochemical symmetry was proposed by P.B. Moore (Smith, 1974).

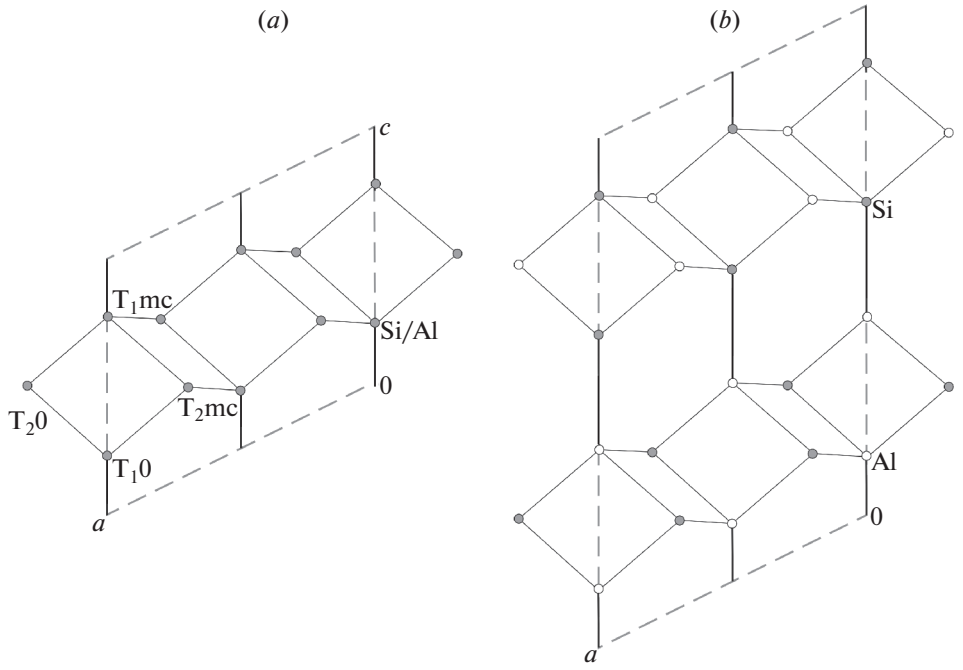

Fig. 3. Projection of the **fsp** network onto the (010) plane showing the nomenclature of the T sites (*a*) and the ordered version of the **fsp** framework with the Al_2Si_2 composition resulting in the doubling of the *c* parameter (*b*).

Рис. 3. Проекция сетки **fsp** на плоскость (010) с обозначенной номенклатурой позиций T (*a*) и упорядоченная версия сетки состава Al_2Si_2, имеющая удвоенный параметр *c* (*b*).

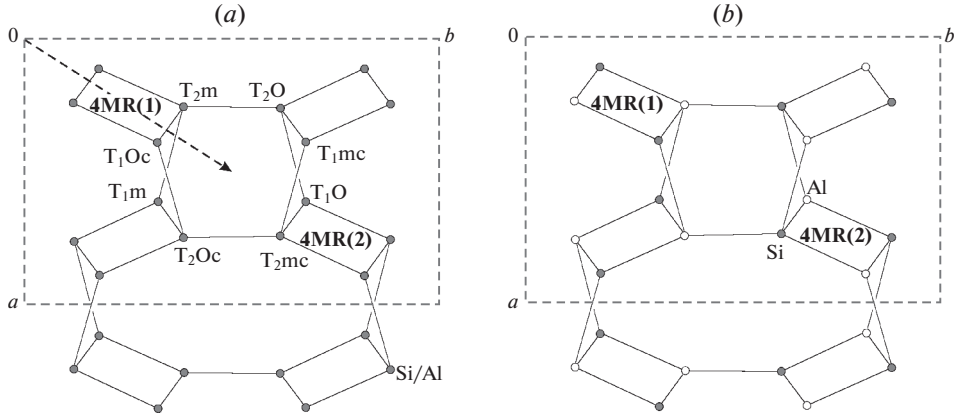

Fig. 4. Projection of the **fsp** network onto the (01) plane showing the nomenclature of the T sites (*a*) and the ordered version of the **fsp** framework with the Al_2Si_2 composition resulting in the disappearance of the *C*-translation [(**a** + + **b**)/2] (*b*). The two four-membered rings [4MR(1) and 4MR(2)] are translationally equivalent in the disordered version (*a*) and become translationally independent in the ordered version (*b*).

Рис. 4. Проекция сетки **fsp** на плоскость (001) с обозначенной номенклатурой позиций T (*a*) и упорядоченная версия сетки состава Al_2Si_2, с отсутствующей C-трансляцией [(**a** + **b**)/2] (*b*). Два четырехчленных кольца, обозначенные 4MR(1) и 4MR(2) трансляционно эквивалентны в разупорядоченном варианте (*a*) и становятся различными в упорядоченном варианте (*b*).

In the case of the ordered $[Al_2Si_2O_8]$ **fsp**-framework, the alternative Al–Si distribution is governed by the Al-avoidance rule [(SiO_4) tetrahedron is surrounded by four (AlO_4) tetrahedra and *vice versa*; sometimes called a Loewenstein rule (Loewenstein, 1954)]. Fig. 4*b* shows that the ordered Al–Si distribution results in the loss of the *C*-translation with the *ab* plane, whereas Fig. 3*b* demonstrates that the Al-Si ordering is possible only with the doubling of the *c* parameter of the **fsp** aristotype cell. The resulting topochemical symmetry of the ordered $[Al_2Si_2O_8]$ **fsp**-framework is $I2/c$ with $c \sim 14$ Å, in contrast to the topological $C2/m$ group with $c \sim 7$ Å. The maximal topochemical $I2/c$ group (or $C2/c$ in a standard setting) is realized in celsian and filatovite (see below).

There are six possible space groups observed for the minerals and synthetic materials with the **fsp** framework topology: (i) $C2/m$, $c \sim 7$ Å (topological symmetry; aristotype; example: sanidine, orthoclase); (ii) $C\bar{1}$, $c \sim 7$ Å (topochemical symmetry for the $AlSi_3$ configuration; example: microcline, albite); (iii) $I2/c$, $c \sim 14$ Å (topochemical symmetry for the Al_2Si_2 configuration; example: celsian); (iv) $I\bar{1}$, $c \sim 14$ Å [example: high-temperature (HT) and high-pressure (HP) modifications of anorthite]; (v) $P\bar{1}$, $c \sim 14$ Å (example: anorthite); (vi) $P2_1/c$, $c \sim 14$ Å [example: HP-modification of synthetic $PbAl_2Si_2O_8$ (Curetti et al., 2015)]. This list does not include the symmetries of incommensurately modulated plagioclases, which will be considered in some detail below.

When studying the crystal structure of orthoclase (including its variety adularia), Colville and Ribbe (1968) observed the presence of "forbidden" streak reflections with $h + k = 2n + 1$ in the diffraction pattern that can otherwise be described in the framework of the $C2/m$ space group and suggested the occurrence of domains with the $P2_1/a$ symmetry ($c \sim 7$ Å). However, recently Xu et al. (2019) reported on the transmission electron microscopy (TEM) observation and density functional theory (DFT) modeling of the nanophase domains in orthoclase and microcline with the *Pa* symmetry ($c \sim 7$ Å) and the composition $NaK[AlSi_3O_8]_2$ characterized by an ordered Na-K distribution. The $P2_1/a$ symmetry reported by Colville and Ribbe (1968) was interpreted as a result of the overlap of the reflections generated by the *Pa* domains and the $C2/m$ host. We note that, from the viewpoint of nomenclature, the *Pa*-structured nanophase could not be considered as a distinct mineral species. According to Nickel and Grice (1998): "...if a domain of nanometric dimensions in a larger mineral grain has a unique composition or crystal structure but is not sufficiently large to qualify as a mineral species, it should not be given a distinctive mineral name. If it is deemed necessary to refer to such a domain by name, it should retain the name of the host mineral, with the addition of an appropriate suffix to indicate the crystallographic or compositional nature of the domain. Such suffixes do not require approval by the CNMMN."

3.2.3. Sanidine, orthoclase, microcline. There are three $K[AlSi_3O_8]$ feldspars, which are distinguished by the different degree of Al/Si ordering, which is also called *structural state* of a feldspar. In order to properly identify a feldspar, one has to analyze the Al contents in the T sites, which are denoted as $t_{1(0)}$, $t_{1(m)}$, $t_{2(0)}$, and $t_{2(m)}$ for the T_10, T_1m, T_20, and T_2m sites, respectively. Note that, for the $C2/m$ structure, $t_{1(0)} = t_{1(m)}$ and $t_{2(0)} = t_{2(m)}$, as imposed by the symmetry. Note that, for the $[AlSi_3O_8]$ framework,

$$t_{1(0)} + t_{1(m)} + t_{2(0)} + t_{2(m)} = 1 . \quad (1)$$

Strictly speaking, sanidine, orthoclase and microcline should not be considered as separate mineral species, but rather as disordered, partially ordered and ordered varieties of the same mineral species. However, due to historical reasons and the importance of petrological and geochemical implications, the three names are retained in the modern mineralogical nomenclature. Table 2 provides the compositional and structural nomenclature for the three species, following borders established by Ribbe (1983a). In order to assign the mineral name properly, one has to know the crystal structure of the mineral, in particular, the unit-cell dimensions,

Table 2. Nomenclature of the $K[AlSi_3O_8]$ feldspars
Таблица 2. Номенклатура калиевых полевых шпатов

Mineral name	Space group	Definition	End member
Sanidine	*C*2/*m*	$0.50 \le 2t_1 < 0.74$	$2t_1 = 0.50$*
Orthoclase	*C*2/*m*	$0.74 \le 2t_1 < 1.00$	–
Microcline	$C\bar{1}$	$t_1 0 > t_1 m > t_2 0 = t_2 m$	$t_1 0 = 1.00$

* $2t_1 = t_1 0 + t_1 m$

space group and the distribution of Al over T sites. The correct determination of the t_i values was widely discussed in mineralogical literature (see Deer et al., 2001). Blasi and Blasi (1993) distinguished three different approaches to the determination of T-site occupancies: (i) the use of unit-cell dimensions; (ii) the use of T-O bond lengths; (iii) the refinement of T-site occupancies using X-ray single-crystal diffraction. The detailed discussion of the advantages and disadvantages of these methods are beyond the scope of this review. However, the necessity of detailed crystal-structure studies in order to properly identify the mineral species allows us to consider them as *cryptic* species, by analogy with cryptic biological species, whose proper identification requires the application of a DNA sequencing (Bickford et al., 2007).

The formation of a particular $K[AlSi_3O_8]$ mineral is related to the rate of crystallization and to the cooling rate of rock-forming melt. Sanidine is characteristic for relatively young volcanic and subvolcanic rocks (the "classical" locality is the Eifel paleovolcanic region, Southern Germany). Microcline and orthoclase form either as a result of solid-state transformation of sanidine or by direct crystallization from moderate-temperature (500 ± 50 °C) melts and solutions (Minerals..., 2003). Both sanidine and orthoclase are therefore metastable kinetically stabilized species, whereas microcline (in its completely Al,Si-ordered ideal form) should be considered as a thermodynamically stable phase.

3.2.4. Ferrisanidine. The synthetic $K[FeSi_3O_8]$ feldspar had been known since the late XIX century (Hautefeuille, Perrey, 1888), and its structure that may possess different structural states was a subject of detailed investigations (Wones, Appleman, 1963; Nadezhina et al., 1993; Lebedeva et al., 2003; Taroev et al., 2008). Natural feldspars with the high Fe content identified as sanidines have been described in lamproites (Linthout, Lustenhouwer, 1993; Kuehner, Joswiak, 1996), but the mineral species itself was described by Shchipalkina et al. (2019) only recently from the active Arsenatnaya fumarole at the Second scoria cone of the Northern Breakthrough of the Great Fissure Tolbachik Eruption, Tolbachik volcano, Kamchatka Peninsula, Russia. Due to the absence of single crystals, the crystal structure was refined by Rietveld method in the *C*2/*m* space group, assuming fully Fe–Si disordered configuration indirectly confirmed by the Raman spectroscopy. Shchipalkina et al. (2019) consider ferrisanidine as a quenched phase that crystallized directly from fumarolic gases at temperatures around 500–700 °C. The observations of different structural states for the synthetic $K[FeSi_3O_8]$ compositions point out to the potential existence of natural Fe-bearing analogues of microcline and orthoclase ("ferrimicrocline" and "ferriorthoclase", respectively).

3.2.5. Rubicline. The Al,Si-disordered synthetic $Rb[AlSi_3O_8]$ feldspar was first prepared hydrothermally by Ghélis and Gasperin (1970) with its crystal structure reported by Gasperin (1971) (see also: Kyono, Kimata, 2001). The ordered triclinic variety was synthesized by ion-exchange reactions using albite as a starting material (Wietze, Wiswanathan, 1971). The natural Rb-rich feldspars have been studied by Teerstra et al. (1997, 1998a, b) who described rubicline as a new mineral species. The mineral was reported as triclinic, space group $C\bar{1}$. Teerstra et al. (1998b) identified three basic subsolidus mechanisms of the formation of rubicline in granitic pegmatites: exsolution from a primary (K, Na, Rb)-feldspar, solution-reprecipitation from the same precursor, and metasomatic coprecipitation with K-feldspar in pollucite. On the basis of

their study of the Rb-rich feldspars from Voron'i Tundry, Kola peninsula, Russia, Pekov and Kononkova (2010) proposed that rubicline was formed *via* natural ion-exchange reactions of microcline with the fluid generated by the breakdown of high-temperature Rb-enriched pollucite. This conclusion is in good agreement with the experimental data on the synthesis of Al,Si-ordered $Rb[AlSi_3O_8]$ feldspar.

3.2.6. Buddingtonite. Buddingtonite, $(NH_4)[AlSi_3O_8]$, was first described by Erd et al. (1964) as "an ammonium feldspar with zeolitic water" with the formula $(NH_4)[AlSi_3O_8] \cdot 0.5H_2O$. However, Voncken et al. (1993) re-investigated the holotype sample and demonstrated that the mineral contains no zeolitic H_2O and is a pure ammonium feldspar. The synthetic analogue of buddingtonite was prepared first by an ion-exchange (Barker, 1964) and then by direct hydrothermal crystallization (Voncken et al., 1988). The preliminary results on the crystal structure of natural buddingtonite were given by Kimball and Megaw (1974), but the detailed report was never published. The synthetic analogue was investigated using different methods, including low-temperature X-ray diffraction study that did not reveal any evidence for the phase transition induced by the reorientation or ordering of the NH_4^+ ion under decreasing temperature (Harlov et al., 2001; Mookherjee et al., 2004, 2005; Vennari et al., 2017). The most probable mechanism of the formation of buddingtonite in nature is by ion-exchange of primary alkali feldspar with NH_4-rich fluid under relatively hot conditions (~100 °C). Franz et al. (2017) reported on the biologically-mediated formation of buddingtonite in the Volyn pegmatites, Ukraine, where the mineral replaces K-feldspar and albite, thus confirming the ion-exchange model of its genesis in nature. All the crystal-structure reports on buddingtonite agree on its $C2/m$ symmetry but, surprisingly, the detailed structure data on natural crystals have not been reported so far.

3.2.7. Albite. There are two modifications of $Na[AlSi_3O_8]$ with the **fsp** framework, which differ from each in their symmetries and structural states. The room-temperature modification is albite that has the triclinic symmetry, space group $C\bar{1}$. In its "low" form, it has an ordered Al/Si distribution with Al concentrated in the $T_1 0$ site (Winter et al., 1979). The "high albite" has a disordered Al/Si configuration, but the unit-cell metrics is triclinic, due to the framework adaptation to rather small size of Na^+ cations. At temperatures around 930–980 °C, albite transforms into "monalbite" that has monoclinic symmetry, space group $C2/m$, and complete Al/Si disorder (Kroll et al., 1980). Wu et al. (2004) reported on the natural occurrence of "monalbite" that has been observed using TEM as submicron-scale inclusions in jadeite quartzite in the Dabie ultrahigh-pressure (UHP) metamorphic terrane, China. It was suggested that the preservation of "monalbite" as a metastable quenched phase was due to the armouring of its grains by jadeite and implies a very rapid cooling during retrograde metamorphism.

3.2.8. Reedmergnerite. Reedmergnerite, $Na[BSi_3O_8]$, a boron analogue of albite, was reported by Milton et al. (1955, 1960) as an autigenic mineral from dolomitic rocks and black oil shales of the lacustrine Green River formation, Utah, U.S. Later it was also reported in alkaline pegmatites of Dara-i-Pioz, Tajikistan (Dusmatov et al., 1967; Grew et al., 1993) and Lovozero, Kola peninsula, Russia (Khomyakov, Rogachev, 1991). The crystal structure of reedmergnerite was solved by Appleman and Clark (1965) and refined by Fleet (1992) in the space group C. The structure is fully ordered with B concentrated in the $T_1 0$ site. It is of interest that synthetic $KBSi_3O_8$ is isotypic to danburite and is therefore based upon the **pcl** framework topology (Kimata, 1993).

3.2.9. Anorthite. The topochemical symmetry of the $[Al_2Si_2O_8]$ framework in anorthite is $I2/c$ as described above. However, the adaptation of the aluminosilicate framework to the relatively small Ca^{2+} cations results in the reduction of its symmetry from $I2/c$ to P. At $T_c \sim 240$ °C, anorthite undergoes the $P\bar{1} \rightarrow I\bar{1}$ phase transition first observed by Brown et al. (1963). Salje (1994) described this phase transition "...as a classical displacive transition with some fluctuations, which do not, however, destroy the thermodynamic second order character of the tran-

sition". The $P\bar{1} \rightarrow I\bar{1}$ phase transition is also observed under high-pressure conditions at 2.61 $\pm \pm$ 0.06 GPa (Angel, 1988, 1994). It is worthy to note that, slightly above the phase transition, the $I\bar{1}$ anorthite demonstrates the splitting of the Ca sites that has either dynamical or statistical character.

Wadoski-Romejin and Armbruster (2013) investigated the high-temperature behavior of gismondine, $Ca_4[Al_8Si_8O_{32}] \cdot 18H_2O$, that also possesses the framework based upon crankshaft chains of tetrahedra, but, in contrast to the **fsp** framework, the flexible one (note that gismondine can in fact be considered as a highly hydrated chemical analogue of anorthite). In one of two different pathways of the high-temperature behavior, above 250 °C gismondine transforms into "Ca-feldspar" phase with the stoichiometry $Ca[Al_2Si_2O_8]$ crystallizing in the space group $C\bar{1}$ ($c \sim 7$ Å). The structure of this new phase is based upon the inflexible **fsp** framework topology with ordered Al/Si distribution. As it was shown above, the ordered Al/Si distribution obeying the Loewenstein rule is impossible for the $C\bar{1}$ ($c \sim 7$ Å) symmetry, so the structure of the "Ca-feldspar" contains both Al–Al and Si–Si links. Such a structure is definitely metastable, since the violation of the Loewenstein rule is associated with the increasing energies (about 40 kJ/mol) of the resulting structure configurations (McConnell et al., 1997). The study by Wadoski-Romejin and Armbruster (2013) demonstrates that metastable feldspar polymorphs can be obtained by means of unusual experimental pathways such as transformation of hydrated structures with the feldspar stoichiometry of their "anhydrous part".

3.2.10. Celsian. Celsian is considered as a stable polymorph of $Ba[Al_2Si_2O_8]$ at ambient conditions. Its full crystal-structure determination was reported by Newnham and Megaw (1960) who described it in the non-standard unit-cell setting, $I2/c$, which was chosen in order to allow comparison with the unit cell of the topological space group $C2/m$. The crystal structure was refined by Griffen and Ribbe (1976). The space group $I2/c$ corresponds to the topochemical space group of the ordered $[Al_2Si_2O_8]$ framework with no Al–Al and Si–Si links (see above). No displacive or order-disorder phase transitions that retain the **fsp** topology have been reported for celsian so far.

3.2.11. Filatovite. The incorporation of pentavalent P^{5+} cations into the tetrahedral framework with the **fsp** topology was observed experimentally by Simpson (1977) and Bychkov et al. (1989) who synthesized $Na[Al_2PSiO_8]$ and $K[Al_2PSiO_8]$ with the feldspar-type structures (however, the full crystal-structure determination was not reported). Bontchev and Sevov (1997) and Bu et al. (1998) prepared and structurally characterized the compounds $(NH_4)_x(NH_3)_{0.5-x}[Al_{1-x}Co_xPO_4]$ and $(NH_4)[AlCoP_2O_8]$, respectively, which both crystallize in the topochemical space group $I2/c$ with ordered arrangements of $(Al/Co)O_4$ and PO_4 tetrahedra. Kotelnikov et al. (2011) prepared a series of As- and P-containing synthetic feldspars and reported on their unit-cell parameters. In nature, P-containing feldspars are known in granites, granitic pegmatites and rhyolites (London et al., 1990; London, 1992, etc.), however, the P_2O_5 content does not exceed 2.6 wt %. Vergasova et al. (2004) discovered filatovite, $K[(Al,Zn)_2(As,Si)_2O_8]$, the first feldspar with pentavalent cation (As^{5+}) as an essential mineral-forming component, which was found in volcanic fumaroles of the Great Fissure Tolbachik eruption, Kamchatka peninsula, Russia. The detailed chemical formula of filatovite can be written as $K[(Al_{2-x}Zn_x)(As_{1+x}Si_{1-x})O_8]$, with $x \sim 0.20$. Filatov et al. (2004) determined the crystal structure of the mineral and demonstrated that it has the topochemical $I2/c$ space group with the ordered (alternating) distribution of the Al/Zn and As/Si sites in the tetrahedral framework. Shchipalkina et al. (2020) investigated the crystal-chemical features of As-bearing sanidine ($C2/m$) from Tolbachik fumarole exhalations. It is worthy to note that all structurally characterized P- and As-containing crystalline compounds of the **fsp** topology with P and As dominant at least in one tetrahedral site possess the $I2/c$ space group, which implies the ordered arrangement of pentavalent and low-valent tetrahedral cations. The $C2/m \rightarrow$

$\rightarrow I2/c$ transition happens at relatively low content of pentavalent elements, e.g. the mineral with As + P = 0.6 apfu already has the $I2/c$ space group.

3.2.12. Incommensurately modulated structures in plagioclases. The crystal chemistry of plagioclases, i.e. the members of the albite-anorthite solid solution series, displays the most structurally complex phenomena in the minerals and compounds with the **fsp** framework topology, which deserves a separate review article with a deep crystallographic analysis. The transition between albite and anorthite involves the substitution mechanism $Na^+ + Si^{4+} \leftrightarrow$ $\leftrightarrow Ca^{2+} + Al^{3+}$. As it was mentioned above, low albite crystallizes in the space group $C\bar{1}$ ($c \sim 7$ Å), whereas the space group for anorthite is $P\bar{1}$ ($c \sim 14$ Å). Chao and Taylor (1940) first observed the existence of superlattice reflections for the members of the albite (Ab) – anorthite (An) solid solutions. The reflections are usually observed for plagioclases in the range $\sim An_{25}$–An_{75}. As a rule, for the crystals in the range $\sim An_{25}$–An_{50}, the diffraction patterns contain sharp *a*-reflections corresponding to the $C\bar{1}$ ($c \sim 7$ Å) structure and weaker satellite *e*-reflections concentrated around the absent *b*-reflections that correspond to the reflections due to the $I\bar{1}$ ($c \sim 14$ Å) structure. The diffraction patterns of the crystals in the range $\sim An_{50}$–An_{75} are more complicated and possess additional weak *f*-reflections. The two types of structures are usually denoted as e_2 and e_1 plagioclases, respectively. The refinements of the crystal structures with the use of satellite reflections [the incommensurate models described in the framework of the (3+1)D superspace approach] demonstrated rather complex modulation patterns with the major component of the $\boldsymbol{q}^*$-vectors (responsible for the modulation) oriented along the *c* axis. The previous structural models that included the alternation of the $C\bar{1}$ ($c \sim 7$ Å) and $I\bar{1}$ ($c \sim 14$ Å) domains (in alternating antiphase orientations) first proposed by Megaw (1960a, b, c) are now replaced by the model consisting of $I1$ domains separated by $I\bar{1}$ domains (Jin et al., 2020). For more details and the discussion of alternative models see recent publications (Xu, 2015; Boysen, Kek, 2015; Xu et al., 2016; Fredrickson, Fredrickson, 2016; Jin, Xu, 2017a, b; Jin et al., 2019, 2020). Jin and Xu (2017a) demonstrated that the appearance of the *e*-reflections is correlated with the cooling history of mineral crystals. The less complex e_2 structure is observed for the fastest cooled samples, whereas the slowest cooled samples show the more complex e_1 structure with additional *f*-reflections.

3.3. Paracelsian topology

3.3.1. General description. The similarity between the **fsp** and **pcl** topologies was recognized at the early stages of the development of X-ray diffraction analysis. In fact, the crystal structure of danburite, $CaB_2Si_2O_8$, the first structurally characterized mineral with the **pcl** topology, was solved in 1931 by C. Dunbar and F. Machatschki (Dunbar, Machatschki, 1931), i.e. *before* the crystal-structure determination of sanidine was published by Taylor (1933). It was nobody else but W.L. Bragg who realized the close topological relations between danburite and feldspar: according to W. Taylor, "...Professor Bragg has pointed out to me that there is an interesting relationship between the sanidine structure and that of danburite $CaB_2Si_2O_8$. Danburite structure is based on rings of four tetrahedra (of composition $B_2Si_2O_8$) similar to those in sanidine and linked together to form continuous chains of four-rings. ⟨...⟩ The central chain is linked to four adjacent chains differently in the two crystals, but in projection the structures are similar" (Taylor, 1933). Indeed, both feldspar (**fsp**) and paracelsian (**pcl**) topologies are based upon crankshaft chains linked in different topological manner. It is important to note that the crankshaft chains in feldspars are twisted compared to those in paracelsian, which opens up the possibility of the formation of inflexible **fsp** topologies. In contrast, the **pcl** topology is flexible, which is reflected in the fact that phases with this topology may contain stoichiometric H_2O, e.g., in the recently reported "K-paracelsian", $K[AlSi_3O_8] \cdot H_2O$ (Boruntea et al., 2019), and zinc arsenates such as $Ba[Zn_2As_2O_8] \cdot H_2O$ [see (Dordević, 2011)].

The topological symmetry of the **pcl** framework (Fig. 5*a*) is *Ccmm* (Smith, 1978). When the vertices of the network are splitted into two kinds under the condition of the absence of the links between the nodes of the same kind, the ideal 2D net of 4- and 8-membered rings loses its *C*-translation (Fig. 5*b*) and the resulting symmetry of the network becomes *Pnam* (Fig. 5*c*). This group, however, does not exclude the links between the nodes of the same kind in the direction perpendicular to the 2D net (i.e., along the extension of the crankshaft chains). This topochemical group is realized in the $[B_2Si_2O_8]$ framework in the danburite-group minerals, where there are both B–B and Si–Si links. In order to completely avoid the existence of such contacts, the symmetry should be reduced further by the elimination of the *m* plane perpendicular to the crankshaft chains, the 2_1 axes running inside the chains, and the *n* glide plane parallel to (100). The resulting topochemical symmetry is $P2_1/a$, which is realized in paracelsian, $Ba[Al_2Si_2O_8]$ (Fig. 5*d*).

3.3.2. The danburite group. The danburite group includes three mineral species with the general formula $M[B_2Si_2O_8]$, where M = Ca (danburite), Sr (pekovite), and Ba (maleevite). The crystal structure of danburite was solved by Dunbar and Machatschki (1931) and refined by Phillips et al. (1974). The electron-density distribution in danburite was investigated experimentally by Downs and Swope (1992) and theoretically by Luaña et al. (2003), who found the presence in its structure of weak bonded O–O interactions. The Sr and Ba analogues of danburite have been reported as mineral species, pekovite and maleevite, respectively, by Pautov et al. (2004). The synthetic analogue of pekovite had been known for long time (Verstegen et al., 1972) and was prepared under high-pressure conditions by Berger and Range (1996), who also reported on its crystal structure as identical to danburite. The synthetic analogue of maleevite was prepared by solid-state reactions from the mixture of $BaCO_3$, H_3BO_3 and SiO_2 at 850 to 900 °C (Mihailova, Stavrakeva, 2005). The high-temperature behavior of the crystal structure of danburite was reported by Sugiyama and Takéuchi (1985) using single-crystal X-ray analysis, whereas Gorelova et al. (2015) provided data on comparative high-temperature behavior of all three members of the danburite group. The high-pressure behavior of danburite was studied by Pakhomova et al. (2017) (see below).

3.3.3. Paracelsian and slawsonite. The crystal structure of paracelsian was first solved by Smith (1953) in the space group *Pnam*, assuming the disordered Al/Si configuration. Using the Smith's data and suggesting the analogy to hurlbutite (see below), Bakakin and Belov (1961) demonstrated that Al and Si in paracelsian are in fact ordered and that the true space group is $P2_1/a$. The crystal structure was refined by Chiari et al. (1985).

Slawsonite is the Sr analogue of paracelsian, which was first reported as a synthetic compound (Barrer, Marshall, 1964). According to Griffen et al. (1977), the mineral was found by Richard C. Erd and co-workers in metamorphosed limestones of the Triassic Martin Bridge formation in Wallowa County, Oregon, U. S. (as to our knowledge, the full formal description of the mineral from the type locality had never been published). Slawsonite is extremely rare and had been found in less than ten localities worldwide (Matýsek, Jirásek, 2016). Tagai et al. (1995) reported the triclinic natural polymorph of slawsonite with very small deviations from the monoclinic symmetry. The mineral transforms into $P2_1/a$ slawsonite by heating to 220 °C.

3.3.4. Hurlbutite and strontiohurlbutite. Hurlbutite, $Ca[Be_2P_2O_8]$, was described by Mrose (1952) as an orthorhombic early-stage pegmatite mineral. Bakakin and Belov (1959) solved the crystal structure of hurlbutite and demonstrated that it is in fact monoclinic, $P2_1/a$. In a separate paper, Bakakin et al. (1959) analyzed the differences between danburite and hurlbutite and identified that, despite the same overall topology, the topochemical symmetries are different due to the different patterns of T-cation ordering. The crystal structure was refined by Lindbloom et al. (1974). Rao et al. (2014) discovered a Sr analogue of hurlbutite, strontiohurlbutite, in the Nanping pegmatite, Fujian province, China. The crystal chemistry of the synthetic $M[Be_2P_2O_8]$ compounds (M = Ca, Sr, Ba) prepared by hydrothermal method was investigated by Dal Bo et al. (2014). Whereas the Ca and Sr compounds adopt a **pcl** framework

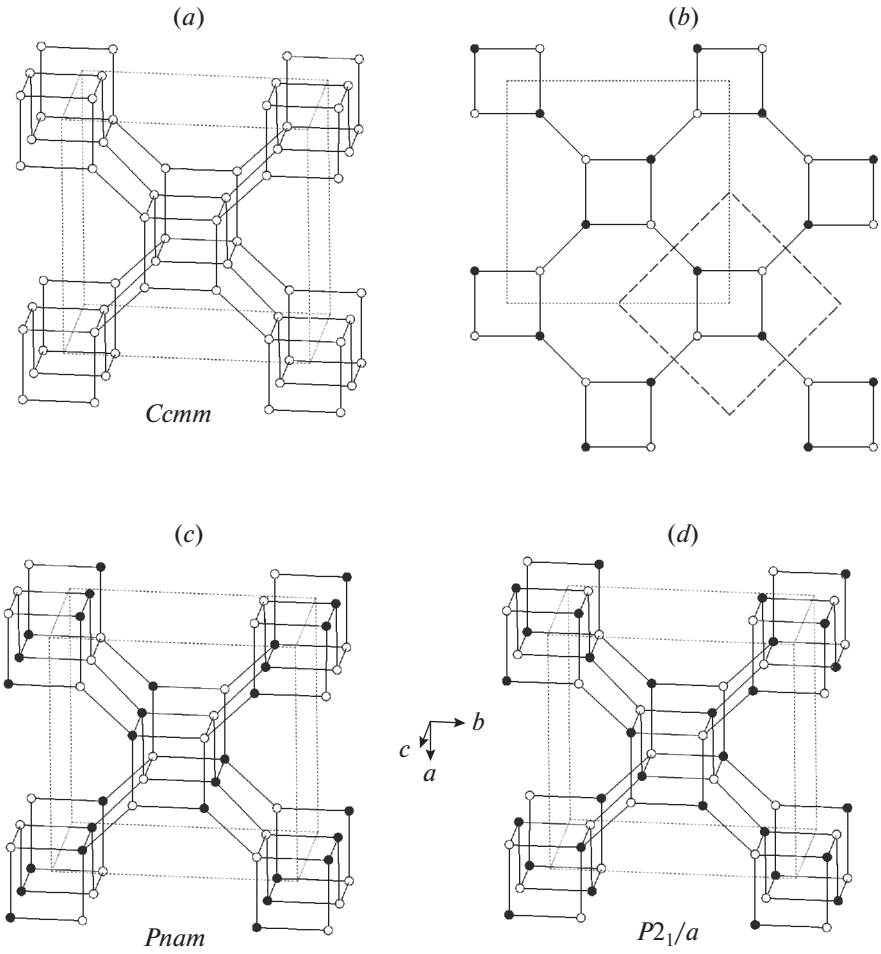

Fig. 5. The **pcl** network in its ideal geometry (space group *Ccmm*) (*a*), the ordered net of four- and eight-membered rings with dashed lines showing the contour of the primitive cell in the disordered version (*b*), the two versions of ordered **pcl** nets with the presence of vertical links between vertices of the same kind (danburite net, *Pnam*) (*c*) and with links between the different vertices only (paracelsian net, $P2_1/a$) (*d*).

Рис. 5. Трехмерная сетка типа pcl в ее идеальной геометрии (пространственная группа *Ccmm*) (*a*), упорядоченная двумерная сетка из 4- и 8-членных колец (штриховой контур указывает примитивную ячейку в разупорядоченной версии) (*b*), два варианта упорядоченной pcl-сетки с наличием связок между вершинами одного типа (данбуритовая сетка, *Pnam*) (*c*) и с присутствием связок только между вершинами разного типа (парацельзиановая сетка, $P2_1/a$) (*d*).

topology, their Ba analogue has a layered structure with the layers based upon the **dms** topology (see below).

*3.4. Svyatoslavite (**bct**) topology*

3.4.1. General description. Svyatoslavite is a metastable pseudo-orthorhombic polymorph of anorthite based upon a three-dimensional framework of corner-linked (AlO_4) and (SiO_4)

tetrahedra. The Al_2Si_2 network contains the Al-Si links only, i.e. the full Al/Si ordering is assumed. The topology of the network corresponds to the **BCT** type of zeolite topologies (hence the **bct** notation used herein), which was observed in the framework alkali silicates with Si^{4+} replaced by Mg^{2+}, Zn^{2+} or Fe^{2+} (type material: Dollase, Ross, 1993). The topological space group is $I4/mmm$ (Fig. 6a), but the Al/Si ordering reduces the symmetry to the topochemical space group $P4_2/mnm$ (Fig. 6b). The topology is based upon 4-membered rings of tetrahedra stacked in columns along the *c* axis and interlinked with similar rings in the adjacent columns. The topology has no crankshaft chains, since the rings in the same column are not interlinked.

3.4.2. Svyatoslavite. Svyatoslavite was first described as a mineral species from the burnt coal dump at Kopeisk, the Chelyabinsk coal basin, Southern Ural, Russia (Chesnokov et al., 1989). The mineral crystallized metastably from the gaseous phase at the temperatures higher than 900 °C. Its synthetic analogue was reported also as a metastable phase forming, along with dmisteinbergite (see below), in the $Ca[Al_2Si_2O_8]$ melt prior to anorthite (Davis, Tuttle, 1951; Abe et al., 1991; Daniel et al., 1995). The crystal structure of the synthetic crystal was solved by Takéuchi et al. (1973) in the monoclinic space group $P2_1$; the authors described the structure as pseudo-orthorhombic with merohedral twinning emulating orthorhombic symmetry. Krivovichev et al. (2012) investigated the holotype sample and confirmed these observations. Taking into account the topochemical space group $P4_2/mnm$, it is very likely that, under heating, svyatoslavite may undergo a temperature-induced displacive phase transition into a high-temperature orthorhombic or tetragonal polymorph. The verification of this hypothesis requires an additional high-temperature X-ray diffraction study.

3.4.3. Kumdykolite. Kumdykolite is a metastable polymorph of albite, which was found by Hwang et al. (2009) as micrometer-scale mineral inclusions in omphacite of eclogite from the Kumdy Kol, Kokchetav ultrahigh-pressure massif, Northern Kazakhstan. The mineral was "...presumed to be a metastable phase formed at high temperatures followed by rapid cooling in the absence of water" (Hwang et al., 2009). Németh et al. (2013) reported the occurrence of kumdykolite in the meteorite Sahara 97072, EH3, where it occurs in the core of a concentrically zoned metal-sulfide nodule. Kotková et al. (2014), Perraki and Faryad (2014), Ferrero et al. (2016, 2018) and Ferrero and Angel (2018) reported on the findings of kumdykolite in solid inclusions in garnet crystals in high-pressure granulites. In all the reported findings, kumdykolite was suggested to be a metastable phase that crystallized at high temperatures and preserved in (confined) anhydrous environments due to the rapid cooling of the host rocks.

The unit-cell parameters of kumdykolite are similar to those reported for svyatoslavite (Table 1) with the pronounced orthorhombic metric. The possible space groups indicated by Hwang et al. (2009) are $P2nn$ or $Pmnn$, but the exact assignment is unclear. The similarity of the unit cell dimensions of kumdykolite and svyatoslavite suggests that the former has the **bct** topology of the aluminosilicate framework as well. However, the $[AlSi_3O_8]$ stoichiometry requires either high topological symmetry (in the case of complete Al/Si disorder) or low symmetry (corresponding to the full Al/Si ordering). The monoclinic crystal structure of svyatoslavite contains four T sites corresponding to the four nodes of the 4-membered ring of tetrahedra, which allows for the ordered $AlSi_3$ configuration (Németh et al., 2013). Thus it is very likely that kumdykolite is also monoclinic with strong orthorhombic pseudo-symmetry, which requires further crystallographic investigations. Kotková et al. (2014) described for kumdykolite the admixture of 2 wt % CaO, pointing out to the possible solid solution between kumdykolite and svyatoslavite according to the plagioclase-type substitution mechanism $Na^+ + Si^{4+} \leftrightarrow Ca^{2+} + Al^{3+}$, which provides further support for the hypothesis on the structural similarity between the two minerals.

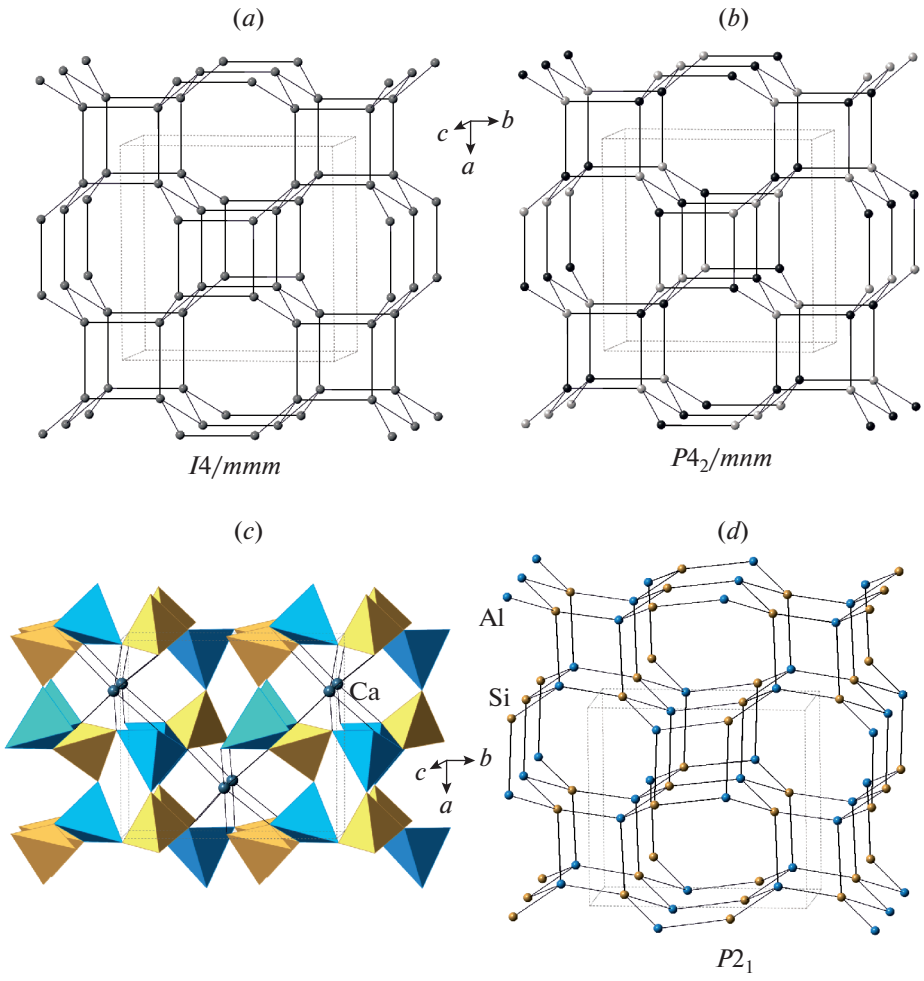

Fig. 6. The **bct** network with its highest possible symmetry (*a*) and the ordered network with the reduced tetragonal symmetry (*b*); the crystal structure of svyatoslavite (*c*) and its Al_2Si_2 net of monoclinic symmetry (*d*). The SiO_4 and AlO_4 tetrahedra in (*c*) are shown in yellow and blue colors, respectively; the Si and Al nodes in (*d*) are shown in yellow and blue colors, respectively.

Рис. 6. Трехмерная **bct** сетка с ее наивысшей симметрией (*a*) и упорядоченная сетка с пониженной тетрагональной симметрией (*b*); кристаллическая структура святославита (*c*) и ее Al_2Si_2 сетка с моноклинной симметрией (*d*). Тетраэдры SiO_4 и AlO_4 на рисунке (*c*) закрашены желтым и голубым цветами, соответственно; узлы Si и Al на рисунке (*d*) показаны желтым и голубым цветами соответственно.

3.5. Dmisteinbergite topology

3.5.1. General notes. In contrast to the previously described **fsp**, **pcl** and **bct** topologies, the **dms** topology is two-dimensional and corresponds to the double tetrahedral layer consisting of two mica-type layers linked by corner-sharing of tetrahedra (Fig. 7*a*). The ideal symmetry of the layer is described by the topological layer group *p6/mmm*, and the ideal space group for the unit cell containing one double layer is *P6/mmm* (Fig. 7b). This maximal symmetry is realized in the crystal structures of synthetic "K-cymrite", $K[AlSi_3O_8] \cdot H_2O$, with disordered Al/Si

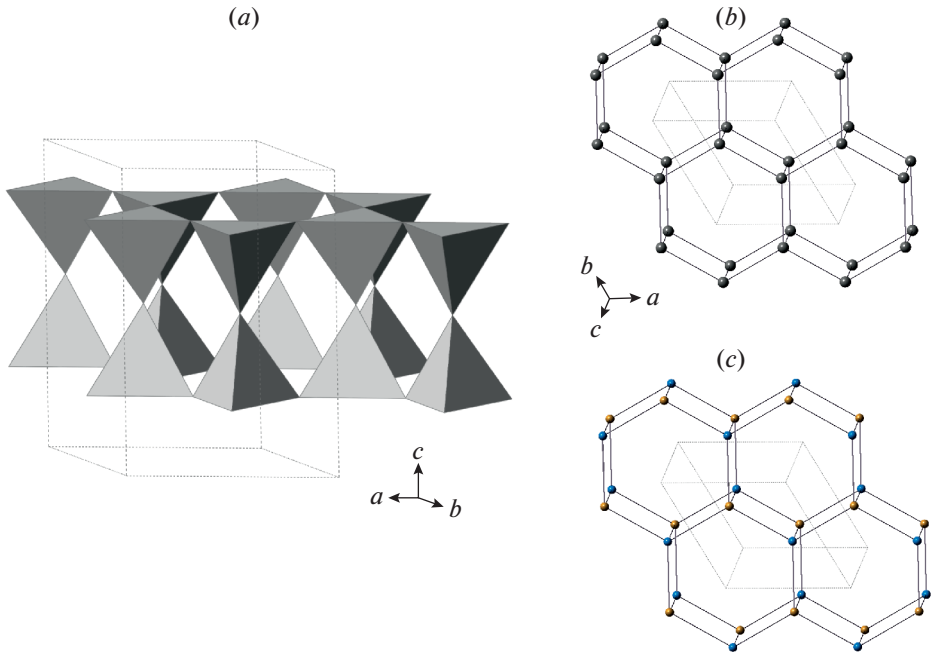

Fig. 7. Double tetrahedral layer with the **dms** topology (*a*) and its disordered (*b*) and Al–Si ordered (*c*) versions. Legend as in Fig. 6.

Рис. 7. Двойной тетраэдрический слой с топологией **dms** (*a*) и его разупорядоченная (*b*) и Al,Si-упорядоченная (*c*) версии. Условные обозначения как на рис. 6.

distribution as reported by Fasshauer et al. (1997) and, most probably, in the high-temperature modification of γ-hexacelsian (Müller, 1977; Xu et al., 2002). For the Loewenstein-ordered $[Al_2Si_2O_8]$ layer, the ideal layer symmetry group is $p\bar{3}m1$, and the ideal space group for the one-layer structure is $P\bar{3}m1$ (Fig. 7c). The M cations are located in the interlayer space and their bonding to the O atoms from adjacent layers strongly influences the conformation of the layers. The nature of the conformation can be described by the in-plane rotation of tetrahedra around the *c* axis. This phenomenon is well-known and studied in detail for the mica-group minerals (Brigatti, Guggenheim 2002; Ferraris, Ivaldi, 2002). The ideal tetrahedral layer formed by six- membered ring has a hexagonal symmetry with the basal O atoms forming perfect hexagonal rings. The layers are actually distorted according to a ditrigonal rotation, which is defined as a rotation of tetrahedra around the axis perpendicular to the plane of the layer (see below the discussion on dmisteinbergite). The degree of the distortion is specified by the tetrahedral rotation angle α. The directions of the ditrigonal rotation in two adjacent layers comprising a double layer may be either identical (++ or –) or opposite (+- or -+). By analogy, the interlayer space may be either of the **A** (+– or –+) or **B** (++ or –) type, which corresponds to either trigonal antiprismatic (octahedral) or trigonal prismatic coordination of the interlayer M cation.

3.5.2. Dmisteinbergite. Along with svyatoslavite (see above), dmisteinbergite is another metastable $Ca[Al_2Si_2O_8]$ that nucleates in a supercooled melt and is subsequently replaced by anorthite (Davis, Tuttle, 1951; Abe et al., 1991; Daniel et al., 1995). Alternatively, the phase may also crystallize from glasses, again as a metastable form of $Ca[Al_2Si_2O_8]$ (Maeda, Yasu-

mori, 2016, 2017; Maeda et al., 2019). Like svyatoslavite, the mineral was first described by Chesnokov et al. (1990) from burnt coal dump at Kopeisk, the Chelyabinsk coal basin (see also: Simakin et al., 2010). It was also reported in pseudotachylytes (Nestola et al., 2010; Mittempergher et al., 2014; Dobson et al., 2018) and meteorites (Ma et al., 2013; Fintor et al., 2013, 2014), where its origin is explained by metastable crystallization as well. The crystal structure of synthetic "hexagonal" $Ca[Al_2Si_2O_8]$ was solved and refined by Takeuchi and Donnay (1959) and Dimitrijević et al. (1996) in the space group $P6_3/mcm$. The structure model contains two tetrahedral double layers per unit cell and implies completely disordered distribution of Si and Al over one crystallographically independent tetrahedral site.

Recently, Zolotarev et al. (2019) re-investigated the holotype sample from a burnt dump of the Mine No 45, Kopeisk, by means of single-crystal X-ray diffraction and Raman spectroscopy. The careful examination of the diffraction data allowed to assign to dmisteinbergite the non-centrosymmetric space group $P312$ with (001) merohedral twinning. The crystal structure of the mineral is shown in Fig. 8. It is based upon double layers of six-membered rings of corner-sharing AlO_4 and SiO_4 tetrahedra. The model obtained in the space group $P312$ shows at least partial order of Al and Si over four distinct crystallographic sites with tetrahedral coordination. The existence of order is evident from the average $\langle T\text{–O}\rangle$ bond lengths (T = Al, Si), which are equal to 1.666, 1.713, 1.611, and 1.748 Å for T1, T2, T3, and T4, respectively. Therefore, T1 and T3 sites are predominantly occupied by Si, whereas the T2 and T4 sites are predominantly occupied by Al. During the structure refinement, it was observed that one of the O sites (O4) is splitted over two positions, which implies the existence of two possible conformations of the $[Al_2Si_2O_8]^{2-}$ layers. The nature of the conformation can be described by the ditrigonal rotation mentioned above with the tetrahedral rotation angle α equal to 22.1° (Fig. 9). The disorder of the O4 site has a direct influence upon the geometry of interlayer space and coordination of Ca atoms. There are two independent Ca sites in the crystal structure of dmisteinbergite. Coordination of the Ca1 site is not influenced by the disorder and is trigonal antiprismatic (distorted octahedral) (Fig. 10*b*). In contrast, the coordination environment of the Ca2 site includes O4 and O4A atoms and therefore depends on the occupancies of the disordered O sites. If one of the two sites is occupied in both upper and lower tetrahedral layers (e.g., O4–O4 and O4A–O4a), the coordination is trigonal antiprismatic (Fig. 10*b*; the **A**-type interlayer). However, if the occupancies of the sites are different (e.g., if the O4 site is occupied in the upper layer and the O4A site is occupied in the lower layer), the coordination becomes trigonal prismatic (Fig. 10*a*; the **B**-type interlayer). The value of the ditrigonal rotation angle α (22.1°) is in good agreement with the values reported for brittle micas with Ca^{2+} cation as interlayer species. For instance, in the crystal structure of clintonite, $Ca(Mg_2Al)_{\Sigma3}(Al_{3-}SiO_{10})(OH)_2$, the α value is in the range 23.1–24.9° (Alietti et al., 1997).

The comparison of the structure model derived for the holotype dmisteinbergite by Zolotarev et al. (2019) with the models reported in the literature (Takeuchi, Donnay, 1959; Ito, 1976; Dimitrijević et al., 1996; Akatsuka et al., 2019) points out to the potential existence of different varieties of dmisteinbergite that may differ in: (i) degree of disorder of the Al/Si tetrahedral sites with completely disordered structure having the $P6_3/mcm$ symmetry with two double layers per unit cell distorted by ditrigonal rotation; (ii) degree of disorder of the O sites, which have a direct influence upon the coordination of the Ca^{2+} cations; (iii) polytypic variations (different stacking sequences and layer shifts). These features may explain, at least in part, the different symmetries reported for dmisteinbergite and its synthetic analogues. The high-temperature behavior of dmisteinbergite had not been studied so far.

3.5.3. Kokchetavite and "K-cymrite". The breakdown of sanidine with the formation of "sanidine hydrate" (Thompson et al., 1998) or "K-cymrite" (Massone, 1992), $K[AlSi_3O_8] \cdot H_2O$, was first reported by Seki and Kennedy (1964). The structural studies demonstrated that "K-cymrite" crystallizes in the topological $P6/mmm$ space group with one layer per unit cell,

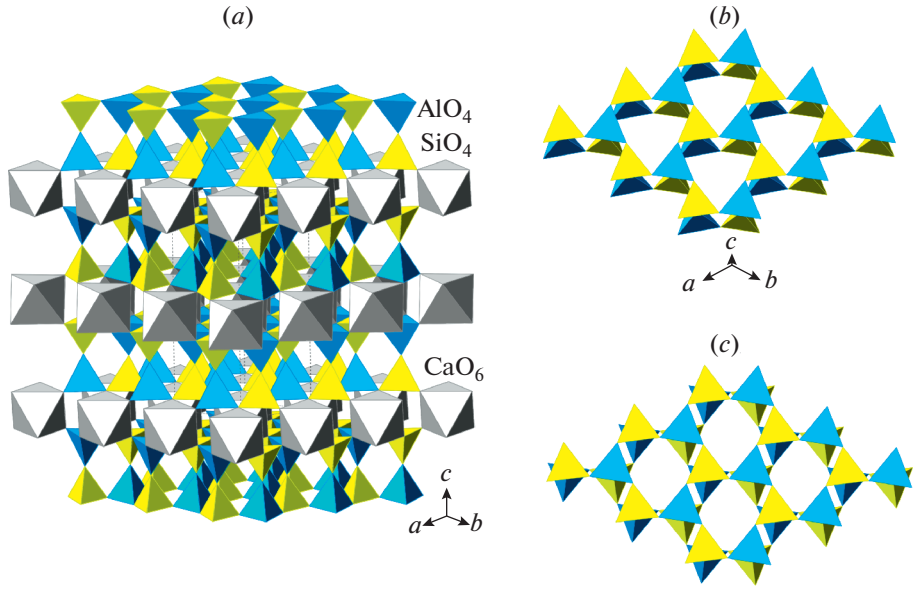

Fig. 8. The crystal structure of dmisteinbergite (*a*) and two versions of its tetrahedral double layers corresponding to different occupancies of the O4 sites (*b*, *c*). After Zolotarev et al. (2019). Legend as in Fig. 6, Ca polyhedra are shown in grey.

Рис. 8. Кристаллическая структура дмиштейнбергита (*a*) и две конфигурации двойного тетраэдрического слоя, соответствующие различной заселенности позиций O4 (*b*, *c*) [по работе (Zolotarev et al., 2019)]. Условные обозначения как на рис. 6, координационные полиэдры кальция закрашены светло-серым цветом.

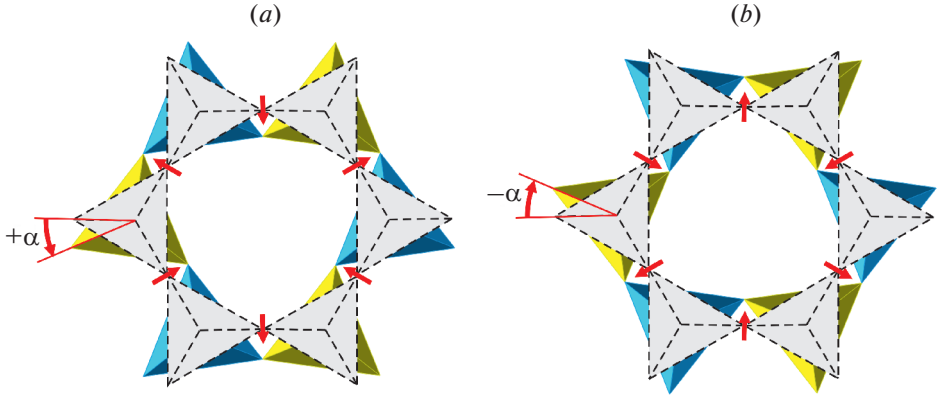

Fig. 9. Ditrigonal rotation of tetrahedra in an ideal six-membered tetrahedral ring (gray tetrahedra with dashed outlines) results in two different versions of distorted ring with positive (*a*) and negative (*b*) values of the α angle. Red arrows indicate directions of shifts of bridging O atoms from their ideal positions. After Zolotarev et al. (2019).

Рис. 9. Дитригональный разворот тетраэдров в идеальном тетраэдрическом кольце (выделено серым цветом) приводит к двум различным вариантам искаженного кольца с положительным (*a*) и отрицательным (*b*) значением угла α. Красные стрелки указывают направление смещения мостиковых атомов кислорода с их идеальных позиций [по работе (Zolotarev et al., 2019)].

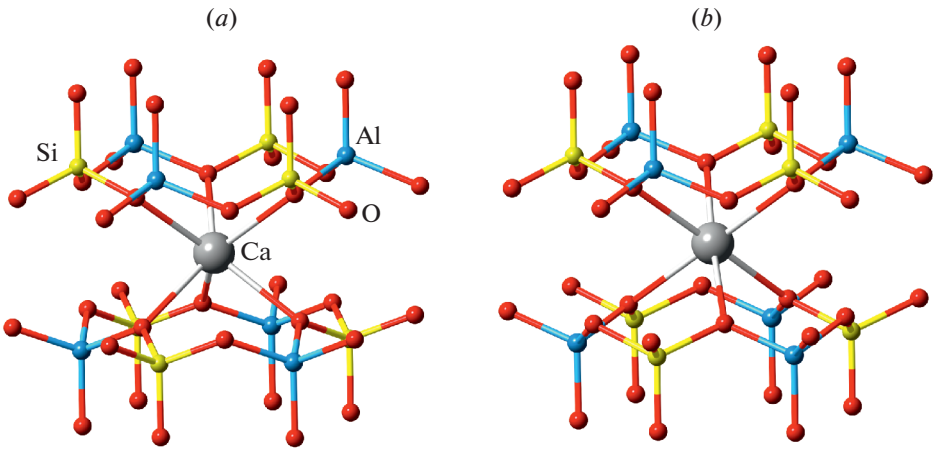

Fig. 10. Two possible coordination environments of the Ca site in dmisteinbergite: trigonal prismatic (*a*) and trigonal antiprismatic (distorted octahedral; *b*). After Zolotarev et al. (2019).

Рис. 10. Две возможных координации атома кальция в дмиштейнбергите: тригонально-призматическая (*a*) и тригональная антипризматическая (искаженная октаэдрическая; *b*) [по работе (Zolotarev et al., 2019)].

complete Al/Si disorder and the absence of ditrigonal rotation of the tetrahedral layers (Fasshauer et al., 1997; Sokol et al., 2020). The latter is definitely a consequence of the large size of the K^+ cations, their high coordination numbers and the relative weakness of the K–O bonds that are unable to distort the tetrahedral layers. It had already been known that the dehydration of "K-cymrite" results in the formation of anhydrous $K[AlSi_3O_8]$ with hexagonal symmetry (Thompson et al., 1998), when Hwang et al. (2004) described its natural occurrence as micrometer-sized inclusions in clinopyroxene and garnet in a garnet-pyroxene rock from the Kokchetav ultra-high-pressure terrane. The mineral, named kokchetavite, was later reported in solid inclusions (nanogranites) in garnet from granulites by Ferrero et al. (2016), along with other metastable phases such as kumdykolite and cristobalite. The unit-cell dimensions reported by Hwang et al. (2004) are in good agreement with those of "K-cymrite" as reported by Fasshauer et al. (1997) and Sokol et al. (2020), indicating that, most probably, the symmetry is hexagonal and the unit cell contains one double layer, due to the absence of ditrigonal rotation. The more definite conclusion, however, requires the complete crystal-structure determination. The natural occurrence of "K-cymrite" was first identified by Mikhno et al. (2013) in polyphase mineral inclusions in clinopyroxene of calc-silicate ultrahigh-pressure metamorphic rocks from the Kokchetav terrane by means of Raman spectroscopy. The authors suggested that, in their samples, kokchetavite formed as a result of dehydration of "K-cymrite", but Ferrero et al. (2016) demonstrated that kokchetavite may also form by direct metastable crystallization. The Raman and NMR spectra of "K-cymrite" and kokchetavite were reported by Kanzaki et al. (2012). The discovery of "K-cymrite" in nature (Mikhno et al., 2013) allows for the consideration of this phase as a separate mineral species. Sokol et al. (2020) pointed out that NH_3- and N_2-rich "K-cymrite" may act as a redox insensitive carrier of nitrogen to >250 km mantle depths in subducting slabs.

3.5.4. Hexacelsian. Among different feldspars, the compound $Ba[Al_2Si_2O_8]$ is the richest in terms of the diversity of polymorphs. Along with two tetrahedral framework polymorphs (celsian and paracelsian), there are three layered polymorphs with the **dms** topology (α-, β- and γ-hexacelsian) and three high-pressure polymorphs with mixed coordination of the T atoms (see below). In

addition, there are at least two metastable hexacelsian polymorphs obtained by dehydration of Ba-exchanged zeolites (Kremenović et al., 1997; Taiji, Yoshiaki, 2002), by analogy with the "Ca-feldspar" phase obtained by Wadoski-Romejin and Armbruster (2013) by the dehydration of gismondine. The high-temperature evolution of hexacelsian was studied, in particular, by Müller (1977) and Xu et al. (2002), who reported on the existence of three polymorphs: low-temperature α- (hexagonal $P6_3/mcm$), intermediate-temperature β- (orthorhombic *Immm*), and high-temperature γ- (hexagonal $P6/mmm$). Galuskina et al. (2017) reported on the natural occurrence of hexacelsian in veins of paralava cross-cutting gehlenite-flamite hornfels located in the Gurim Anticline, Negev Desert, Israel. Here the mineral was formed due to the rapid crystallization from melt, which explains its preservation as a metastable quenched phase. The natural hexacelsian was reported to have the space group $P6_3/mcm$, which is usually ascribed to the α-polymorph (Müller, 1977; Xu et al., 2002).

Among three basic topologies of $Ba[Al_2Si_2O_8]$, **fsp** (celsian), **pcl** (paracelsian), and **dms** (hexacelsian), celsian is the most interesting from the viewpoint of practical applications, due to its low thermal expansion coefficient (2.29×10^{-6} °C^{-1}), good dielectric properties, high melting point (~1760 °C), and excellent resistance towards oxidation and reduction (Li et al., 2020). However, its preparation by direct crystallization from melt is problematic, due to the metastable formation of hexacelsian and the high kinetic barrier of the hexacelsian → celsian transformation. Paracelsian occurs as an intermediate metastable transitional phase between hexacelsian and celsian (Li et al., 2020 and references therein). Thus, the $Ba[Al_2Si_2O_8]$ phase stable under ambient conditions is celsian, whereas paracelsian and hexacelsian are metastable phases.

3.5.5. Cymrite. Cymrite, $Ba[Al_2Si_2O_8] \cdot H_2O$, was first reported by Smith et al. (1949) from the Bennalt manganese mine, Rhiw, Carnarvonshire, Wales, UK. The mineral is rare and its formation is usually associated with near-surface sedimentary or low-temperature (up to 300 °C) hydrothermal conditions (Hsu, 1994, Sorokhtina et al., 2008, and references therein). Its crystal structure is based upon the $[Al_2Si_2O_8]^{2-}$ double layers as described above, but, in contrast to "K-cymrite", is much more complex. Its crystal structure was first studied by Kashaev (1966) and re-investigated by Drits et al. (1975) and Bolotina et al. (1991, 2010). Drits et al. (1975) reported cymrite to be monoclinic, pseudo-orthorhombic, $P2_1$, $a = 5.33$, $b = 36.6$, $c = 7.67$ Å, $\beta = 90°$. The refinement converged to the R_1 index of 0.135 and the disordered arrangement of Al and Si was observed. Bolotina et al. (2010) refined the structure using a sixfold twinned model to $R_1 = 0.054$. The elongated *b* axis was reported to be the result of a wave-like modulation of the tetrahedral layer as shown in Fig. 11 [the (3+1) superspace approach suggested by Bolotina et al. (1991) was later reconsidered by Bolotina et al. (2010) in the favor of the twinned model]. The phase transitions of cymrite under heating are poorly know, except for the fact that it loses H_2O and transforms first to hexacelsian and then to stable celsian.

4. OCTAHEDRAL STRUCTURES

4.1. Hollandite topology

The formation of the $K[AlSi_3O_8]$ feldspar polymorph in the high-pressure experiments using diamond anvil cells was first reported by Ringwood et al. (1967). The crystal structure [determined by Ringwood et al. (1967) and refined by Yamada et al. (1984) from powder data and Zhang et al. (1993) using single-crystal data] belongs to the hollandite structure type and consists of octahedral framework composed from double chains of edge-sharing (TO_6) octahedra (T = Al, Si) that share corners to form channels with square cross-section that accommodate K^+ cations (Fig. 12). The Al/Si distribution is disordered. The K^+ cations are in eightfold cubic coordination with eight K^+—O bonds ~2.71—2.79 Å long (depending upon the pressure). It is remarkable that the K···K contacts within the column of K^+ ions in the channel are slightly

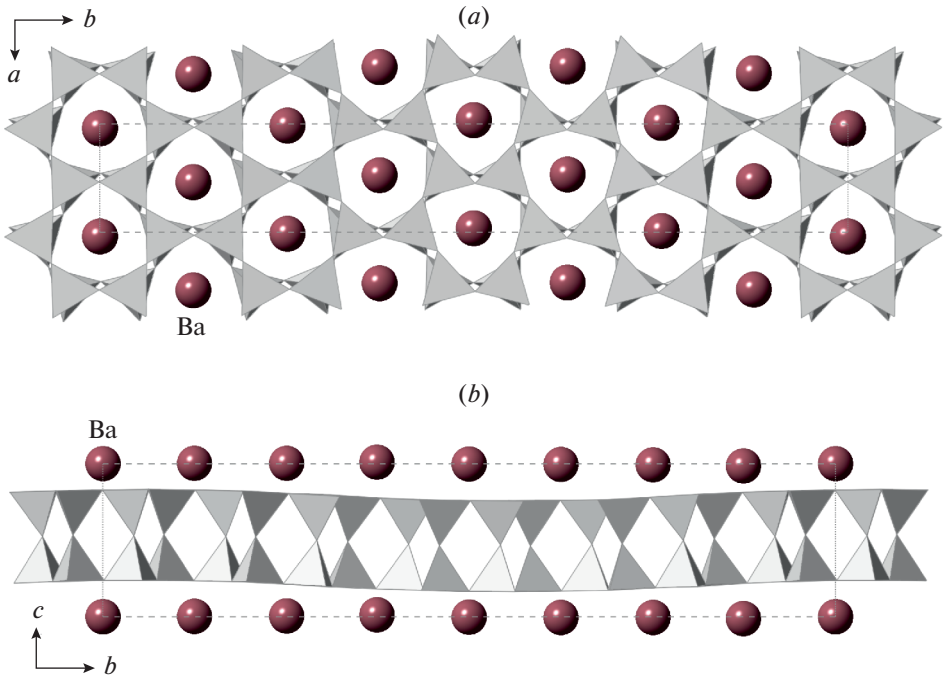

Fig. 11. The crystal structure of cymrite projected along the *c* and *a* axes (*a, b*, respectively). The positions of H_2O groups inside the layers are omitted for clarity.

Рис. 11. Кристаллическая структура кимрита в проекции вдоль осей *c* и *a* (*a*, *b* соответственно). Позиции молекул воды внутри слоев опущены для ясности изображения.

shorter than the K^+–O bonds, which indicates the possibility of the K–K closed-shell attractive interactions. The high-pressure investigations of a synthetic hollandite-type $K[AlSi_3O_8]$ by Zhang et al. (1993) demonstrated that the *a* axis is approximately twice as compressible as *c*, which is explained by the rigidity of the octahedral chains due to the strong repulsive Si^{4+}-Si^{4+} forces across the shared edges of (TO_6) octahedra. The aristotype hollandite structure has the topological space group $I4/m$ which may transform to $I2/m$ under high pressure [~20 GPa as observed for the hollandite-type $K[AlSi_3O_8]$ by Ferroir et al. (2006)]. The phase transition is second-order in character (Boffa Ballaran et al., 2009).

4.2. Lingunite, liebermannite, stöfflerite

The synthetic analogue of lingunite, a natural hollandite-type $Na[AlSi_3O_8]$, was first synthesized in high-pressure experiments (Liu, 1978; Tutti, 2007). According to Liu and El Goresy (2007), its first natural occurrence was reported by Mori (1990, 1994) in the Yamato-790729 L6 chondrite, followed by its other findings in meteorites with the X-ray diffraction data and Raman spectrum first provided by Gillet et al. (2000). The mineral was approved by the IMA in 2004 (IMA proposal 2004-054), but its full (formal) description is not published to date. The name honors Lin-gun Liu from Institute of Earth Sciences, Academia Sinica, Taiwan, who seems to be first to prepare its synthetic analogue. Lingunite was also reported in impactites, where it may occur in association with maskelynite, a glass with the feldspar composition (see below) (Agarwal et al., 2016).

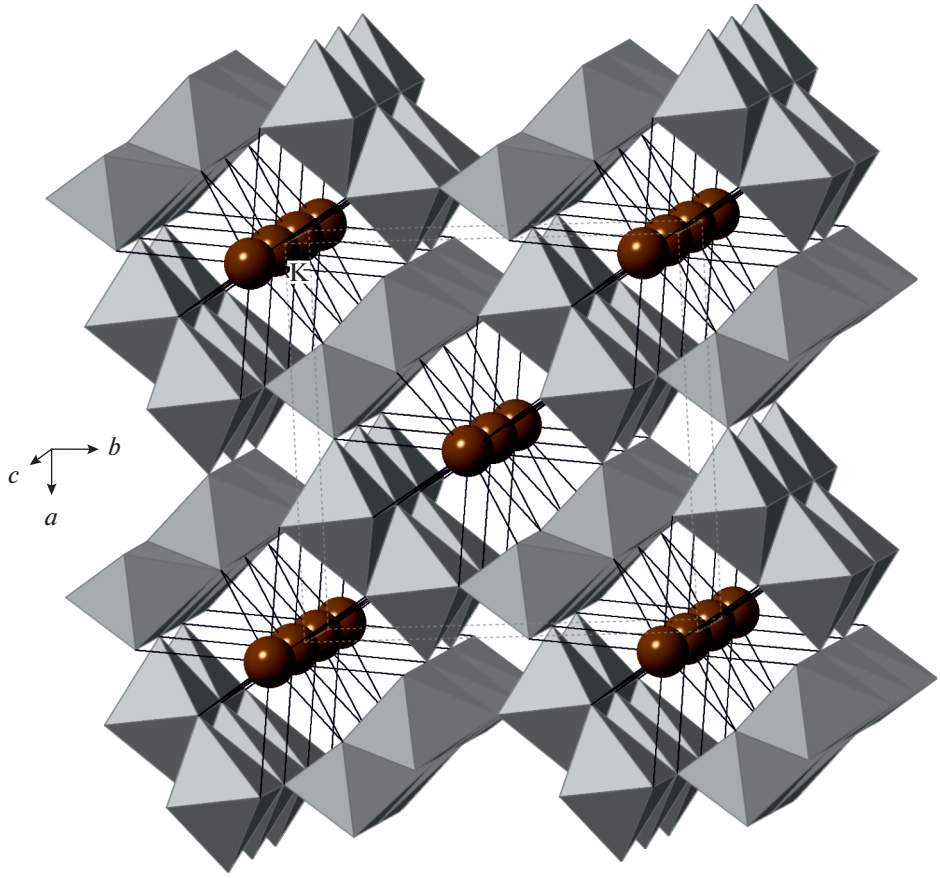

Fig. 12. The crystal structure of liebermannite, $K[AlSi_3O_8]$. The TO_6 octahedra are shown in grey, K^+ cations in brown.

Рис. 12. Кристаллическая структура либерманнита $K[AlSi_3O_8]$. Октаэдры TO_6 закрашены серым, катионы K^+ показаны коричневыми сферами.

Liebermannite, the hollandite-type $K[AlSi_3O_8]$ polymorph, was recently approved as a new mineral by the IMA (Ma et al., 2018). The holotype material is from the Martian meteorite (shergottite) Zagami, where it was reported as formed *via* solid-state transformation of primary K-feldspar during an impact event that achieved pressures of ~20 GPa or more. Prior to the formal description, the mineral was reported as a natural phase in shergottites by Langenhorst and Poirier (2000a) and Beck et al. (2005, 2007), but without structural data first provided by Ma et al. (2018). In Zagami, liebermannite is associated with maskelynite, stishovite, pigeonite and lingunite.

Stöfflerite, the hollandite-type analogue of anorthite, was approved as a new mineral species by the IMA in 2017 (Tschauner, Ma, 2017), but its formal description still awaits publication. The earlier reports on the discoveries of the Ca-rich hollandite-type aluminosilicate in Zagami and NWA-856 meteorites were due to El Goresy et al. (2000), Langenhorst and Poirier (2000b), and Beck et al. (2004).

5. HIGH-PRESSURE STRUCTURES WITH MIXED COORDINATIONS

5.1. Preliminary notes

In this part of the review, we shall discuss the high-pressure behavior and polymorphism of feldspar-family phases as revealed by a series of very recent high-pressure cold compression X-ray diffraction experiments with the use of high-energy synchrotron radiation (Pakhomova et al., 2017, 2019, 2020; Gorelova et al., 2019). The results obtained in these experiments are quite remarkable and essentially extend our understanding of polymorphism and phase transitions in the framework feldspar-like structures. In total, fourteen new polymorphs have been discovered and structurally characterized, not counting the maleevite and pekovite polymorphs still awaiting detailed publications. Quite highlighting are also the recent results on the high-pressure behavior of datolite and hingganite-(Y), two minerals of the gadolinite supergroups that are based upon single sheets of 4- and 8-membered rings topologically identical to the one shown in Fig. 5*a* (Gorelova et al., 2018, 2020).

The cold-compression high-pressure behavior had been studied for the structures with **fsp** [albite, anorthite and microcline (Pakhomova et al., 2020)] and **pcl** [danburite (Pakhomova et al., 2017), hurlbutite (Pakhomova et al., 2019), and paracelsian (Gorelova et al. 2019)] framework topologies, i.e. the topologies based upon crankshaft chains of tetrahedra. We remind that the **fsp** and **pcl** topologies are inflexible and flexible, respectively, and this difference first recognized by Smith (1968) appears to be of crucial importance for the high-pressure behavior of the two types of frameworks structures. The polymorphism of the flexible **pcl** topology is driven by the compression of the framework due to the rotation of the chains around their axes with subsequent densification of structures into close-packed arrangements, whereas the phase transitions of the **fsp** structures involves transformation of the crankshaft chains and formation of novel structure topologies.

*5.2. High-pressure behavior of structures with the **fsp** framework topology*

5.2.1. The [$AlSi_3O_8$] stoichiometry: general features. Pakhomova et al. (2020) reported on new polymorphs of microcline (microcline-II) and albite (albite-II and III). In their completely ordered varieties, microcline and albite contain Al concentrated in the $T_1$0 site. The formation of all three new high-pressure polymorphs follows the same scenario:

(i) breaking of crankshaft chains;

(ii) formation of the okenite-type [Si_3O_8] chains of corner-sharing (SiO_4) tetrahedra;

(iii) separation of Al into dimers of edge-sharing (AlO_n) polyhedra (n = 5, 6) associated with the changes in the coordination number of Al;

(iv) in the case of albite-III, breaking of the okenite chains into triple rings with the formation of dimers of edge-sharing (SiO_5) square pyramids linking the rings into layers.

In all cases, the polymorphs have dense framework structures of new topological types. It is worthy to note that the above scenario is dictated by the topological inflexibility of the **fsp** framework, which prevents the cooperative rotation of the crankshaft chains that could densify the structure as it is observed for the **pcl** topology (see below).

Below we consider each of the three new M[$AlSi_3O_8$] polymorphs (M = K, Na) in more details, providing new structure descriptions not considered in the original report by Pakhomova et al. (2020).

5.2.2. Microcline-II = K[$^{vi}Al(^{iv}Si_3O_8)$]. As reported by Pakhomova et al. (2020), in between 10 and 13 GPa, microcline undergoes a phase transition associated with the increase in the coordination number of Al from four to six. The phase transition is accompanied by the breaking of the crankshaft chains. Instead, a new silicate ribbon is formed running along the *c* axis and consisting of alternating 4- and 6-membered tetrahedral rings (Fig. 13*b*). The [Si_3O_8] ribbons of this type are known in minerals (Day, Hawthorne, 2020) and have been observed in the

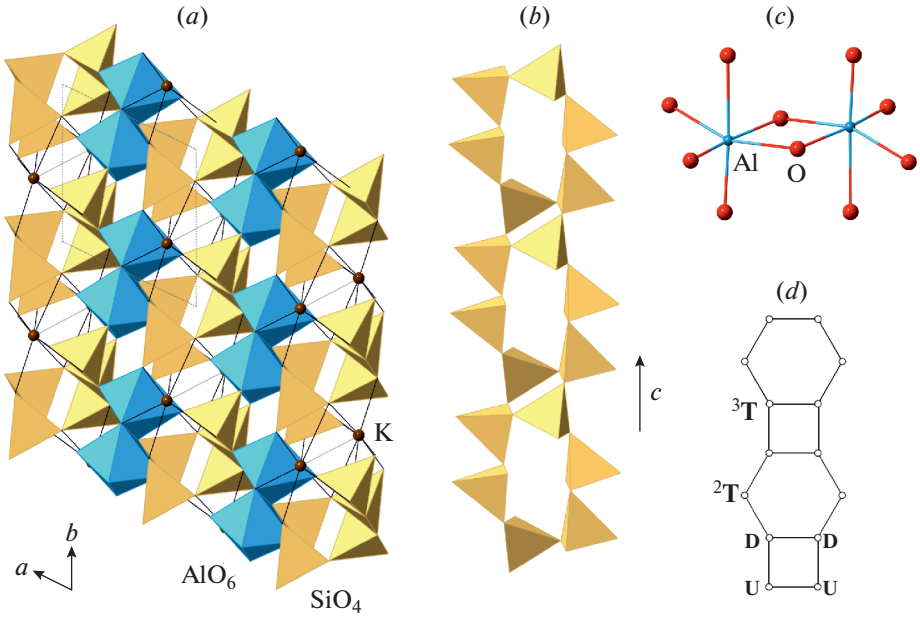

Fig. 13. The crystal structure of "microcline-II" projected along the *c* axis (*a*), the okenite silicate chain (*b*), the dimer of AlO_6 octahedra (*c*), and the graph of the okenite chain (*d*). See text for details. Legend as in Fig. 6.

Рис. 13. Кристаллическая структура высокобарической модификации микроклина ("микроклин-II") (*a*), окенитовая кремнекислородная цепочка (*b*), димер из двух октаэдров AlO_6 (*c*) и граф окенитовой цепочки (*d*). Условные обозначения как на рис. 6.

crystal structures of okenite, $Ca_{10}[Si_3O_8][Si_6O_{15}]_2 \cdot 18H_2O$ (Merlino, 1983) and yangite, $PbMn[Si_3O_8] \cdot H_2O$ (Downs et al., 2016). According to the nomenclature developed by Day and Hawthorne (2020), the ribbon can be designated as $^2T_2{}^3T_4$, where the superscript numbers correspond to the connectivities of tetrahedra, whereas the subscript numbers indicate the numbers of the particular tetrahedra within the chain identity period (Fig. 13*d*). The ribbons are linked by dimers of edge-sharing (AlO_6) octahedra (Fig. 13*c*) into three-dimensional octahedral-tetrahedral framework (Fig. 13*a*). The K^+ cation is located in the framework interstices and coordinated by nine O atoms. Taking into account the coordination numbers of framework-forming Al and Si atoms, the crystal-chemical formula of microcline-II can be described as $K[^{vi}Al(^{iv}Si_3O_8)]$. Microcline-II is stable at least up to 27 GPa (Pakhomova et al., 2020).

5.2.3. Albite-II = $Na[^{vi}Al(^{iv}Si_3O_8)]$. The crystal structure of albite-II solved and refined by Pakhomova et al. (2020) at 13.5 GPa has many similarities to the crystal structure of microcline-II, though the two structure types are different (Fig. 14). It can also be described as based upon the three-dimensional $[^{vi}Al(^{iv}Si_3O_8)]$ octahedral-tetrahedral framework formed by the linkage of the okenite-like $[Si_3O_8]$ ribbons (Fig. 14*b*) via $[Al_2O_{10}]$ octahedral dimers (Fig. 14*c*). However, the conformation degree of the ribbons is different, as can be inferred from the comparison of Figs. 13*b* and 14*b*. The chains are parallel to the *b* axis and are packed within the (100) plane (Fig. 14*b*). The Na^+ cations reside in the framework cavities and have eightfold coordination.

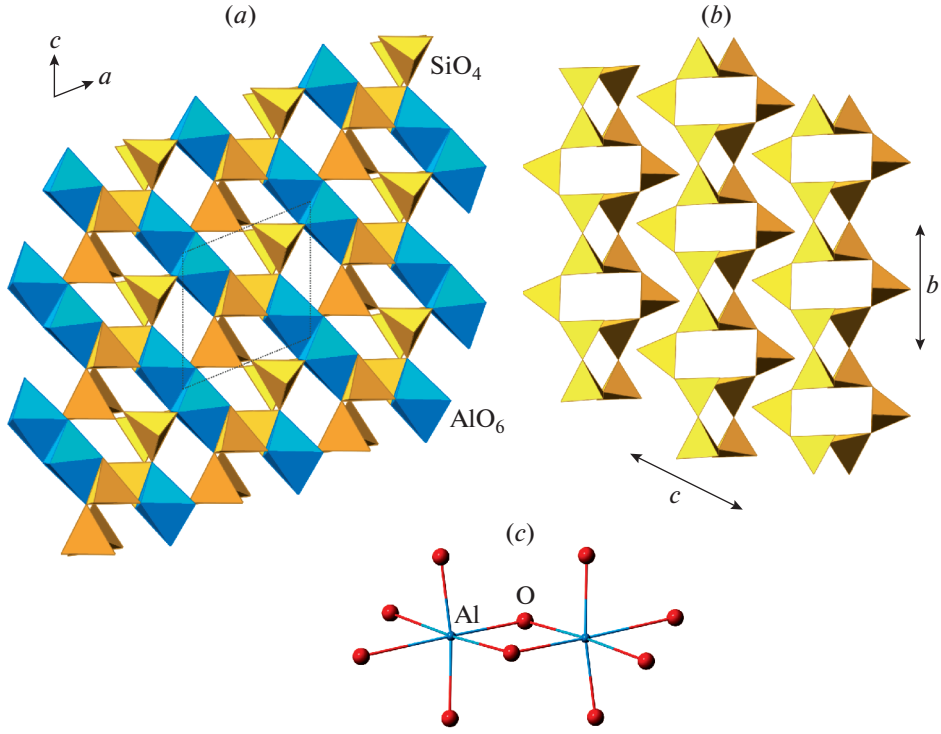

Fig. 14. The crystal structure of "albite-II" projected along the *b* axis (*a*), the okenite silicate chain (*b*), and the dimer of AlO_6 octahedra (*c*). See text for details. Legend as in Fig. 6.

Рис. 14. Кристаллическая структура высокобарической модификации альбита ("альбит-II") (*a*), окенитовая кремнекислородная цепочка (*b*) и димер из двух октаэдров AlO_6 (*c*). Условные обозначения как на рис. 6.

5.2.4. Albite-III. In between 13.5 and 16 GPa, albite-II transforms into albite-III that inherits its basic structural features, but with essential structural modification. The triclinic unit cell doubles in size with the splitting of Al sites from one (as in albite-II) into two, Al1 and Al2. The number of the Si sites becomes six (instead of three in albite-II). The coordination number of Al1 changes to five, whereas that of Al2 remains equal to six. From six Si sites, five (Si1–Si5) remain tetrahedrally coordinated, whereas the Si6 site adopts fivefold square-pyramidal coordination. From the viewpoint of structural architecture, the (100) layers of the okenite ribbons (Fig. 14*b*) transforms into the layers of (SiO_4) tetrahedra interlinked by dimers of ($Si6O_5$) pyramids (Fig. 15*c*). The okenite ribbons split into the [$Si_{10}O_{28}$] triple rings consisting of the central 6-membered ring sharing opposite edges with two 4-membered rings (Fig. 15*d*). As to our knowledge, rings of this topological type have never been observed in minerals or inorganic compounds. The silicate layers have the composition [$^{v}Si_2O_4[^{iv}Si_{12}O_{28}]$] and are oriented parallel to the (101) plane (Fig. 15*b*). The linkage of the layers is provided by the dimers of ($Al1O_5$) square pyramids (Fig. 15*e*) and ($Al2O_6$) octahedra (Fig. 15*f*). According to Pakhomova et al. (2020), albite-III is stable at least up to 20 GPa. It is remarkable that, upon decompression, albite-III transforms into the room-temperature $C\bar{1}$ (c ~ 7 Å) structure with the **fsp** topology.

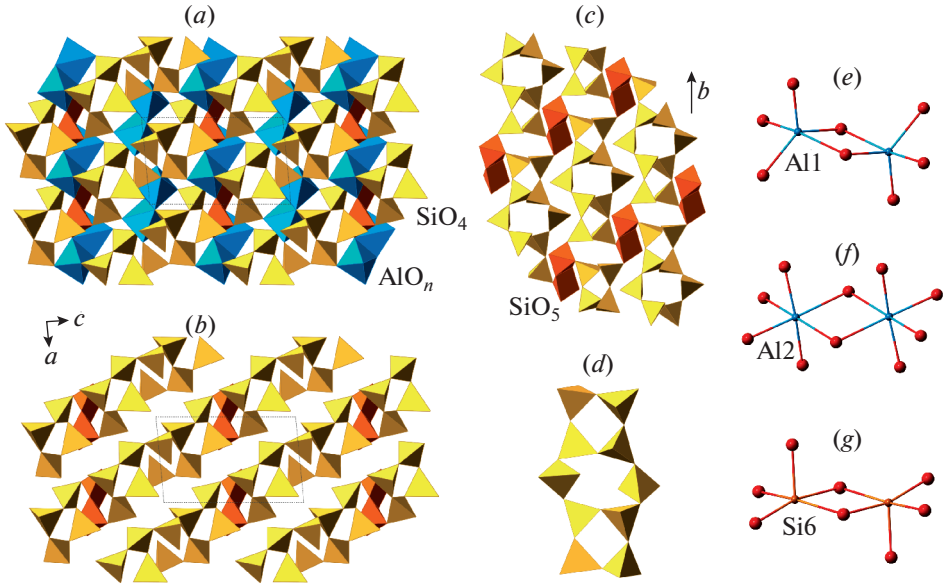

Fig. 15. The crystal structure of "albite-III" projected along the *b* axis (*a*), the same with the Al polyhedral omitted featuring the layers of Si polyhedra (*b*), the structure of silicate layer (*c*), the triple ring of silicate tetrahedra (*d*), and the dimers of AlO_5, AlO_6, and SiO_5 polyhedra (*e*, *f*, and *g*, respectively). See text for details. Legend as in Fig. 6, SiO_5 polyhedra are shown in orange.

Рис. 15. Кристаллическая структура высокобарической модификации альбита ("альбит-III") в проекции вдоль оси *b* (*a*), то же без координационных полиэдров Al для отображения присутствия в структуре кремнекислородных слоев (*b*), развертка силикатного слоя (*c*), тройное кремнекислородное кольцо нового типа (*d*) окенитовая кремнекислородная цепочка (*b*) и димеры из координационных полиэдров AlO_5, AlO_6 и SiO_5 (*e*, *f* и *g* соответственно). Условные обозначения как на рис. 6, координационные полиэдры SiO_5 закрашены оранжевым цветом.

The remarkable feature of the albite-II → albite-III phase transition is the decrease of the coordination number of one of the Al sites from six in low-pressure modification to five in high-pressure modification.

5.2.5. The $[Al_2Si_2O_8]$ stoichiometry: anorthite-III. It seems feasible to suggest that, in the $[AlSi_3O_8]$ **fsp**-frameworks (microcline and albite), the presence of Si-Si links results in the separation of a silicate substructure from the Al-oxo units during compression, whereas, in the $[Al_2Si_2O_8]$ frameworks, the absence of such links leads to the totally different high-pressure behavior. In fact, the crystal structure of anorthite-III stable between ~9 and 16 GPa (Pakhomova et al., 2020) shows a remarkable complexity, which, however, can be rationalized in terms of the reconstruction of the crankshaft chains. Fig. 16*a* shows the projection of the Al_2Si_2 network in anorthite along the *a* axis under ambient conditions. Due to the twisted character of the crankshaft chains in the inflexible **fsp** topology, they project along the chain extension as two 4-membered rings rotated relative to each other around the vertical axis. All vertices in the network are 4-connected and all crankshaft chains are topologically identical. For comparison, Fig. 16*b* shows the projection of the Al_2Si_2 network in albite-III along the *a* axis. It can be seen that the Al and Si nodes still group into one-dimensional 1D units, but now with different topologies. Since the symmetry of albite-III is $P\bar{1}$, there are four different types of 1D

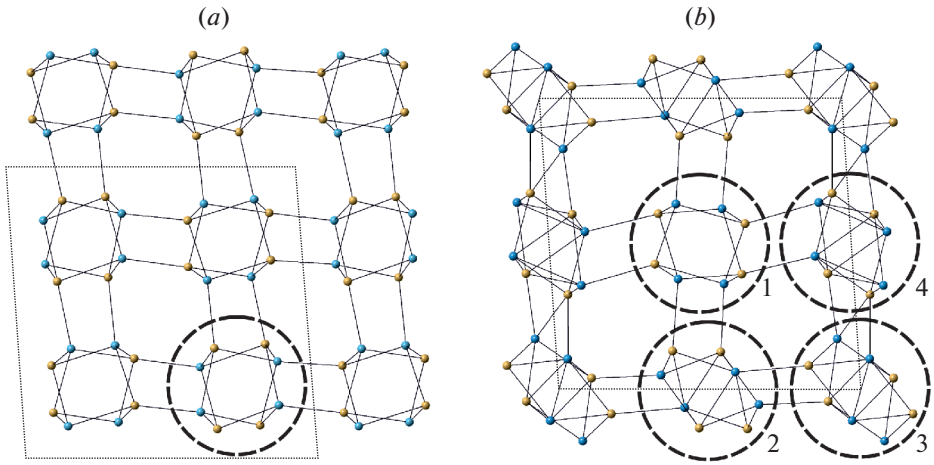

Fig. 16. The Al_2Si_2 nets in anorthite (*a*) and anorthite-III (*b*). Legend as in Fig. 6.

Рис. 16. Сетки Al_2Si_2 в анортите (*a*) и "анортите-III" (*b*). Условные обозначения как на рис. 6.

units denoted for the convenience as **1**, **2**, **3**, and **4**. All four units are in fact crankshaft chains, distorted and reconstructed (for **2**, **3** and **4**). Fig. 17 provides structural and topological diagrams describing the chain topologies. For each chain, a polyhedral representation is given followed by the 1D graph that defines the connectivity of nodes in each chain (we remind that two nodes are joined by an edge, if the respective coordination polyhedra have a common O atom). The edges of the 1D graphs are then separated into those corresponding to the basic crankshaft chains (shown as single line segments) and additional ones that appear in the course of reconstruction (shown as bold dashed lines). The right topological diagram for each chain shows only the crankshaft skeleton of each chain. It is truly remarkable that the four chains are topologically different:

(i) the chain **1** is composed of (SiO_4) and (AlO_4) tetrahedra and can be considered as a pristine crankshaft chain inherited from the structure of anorthite-I (Fig. 17*a*);

(ii) the chain **2** contains (SiO_4) and (AlO_4) tetrahedra, along with (AlO_5) trigonal bipyramids that share corners with three adjacent (SiO_4) tetrahedra and one (AlO_4) tetrahedron (Fig. 17*b*);

(iii) the chain **3** is based upon (SiO_4) tetrahedra and (AlO_6) octahedra, which form edge-sharing dimers flanked on two sides by two additional corner-linked octahedra (Fig. 17*c*);

(iv) the chain **4** consists of (SiO_4) tetrahedra and (AlO_5) polyhedra; the latter share corners to form 4-membered rings covered by one of the two symmetrically independent tetrahedra; one of the (AlO_5) polyhedra share an edge with adjacent (SiO_4) tetrahedron, which is not seen in three other types of chains (Fig. 17*d*).

The crystal structure of anorthite-III shows another (compared to albite and microcline) pathway of the reconstruction of the **fsp**-topology under pressure: the modification of the chemical bonding system within the crankshaft chains through the formation of additional Al-O bonds with the increase of the coordination number of Al up to 6. The Ca^{2+} in the framework cavities are either eight- or ninefold coordinated (Pakhomova et al., 2020).

In conclusion, the phase transition mechanism in aluminosilicates with the **fsp** framework topology depends upon the Al:Si ratio and is modified by the nature of the M cation (compare the behavior of albite *versus* microcline).

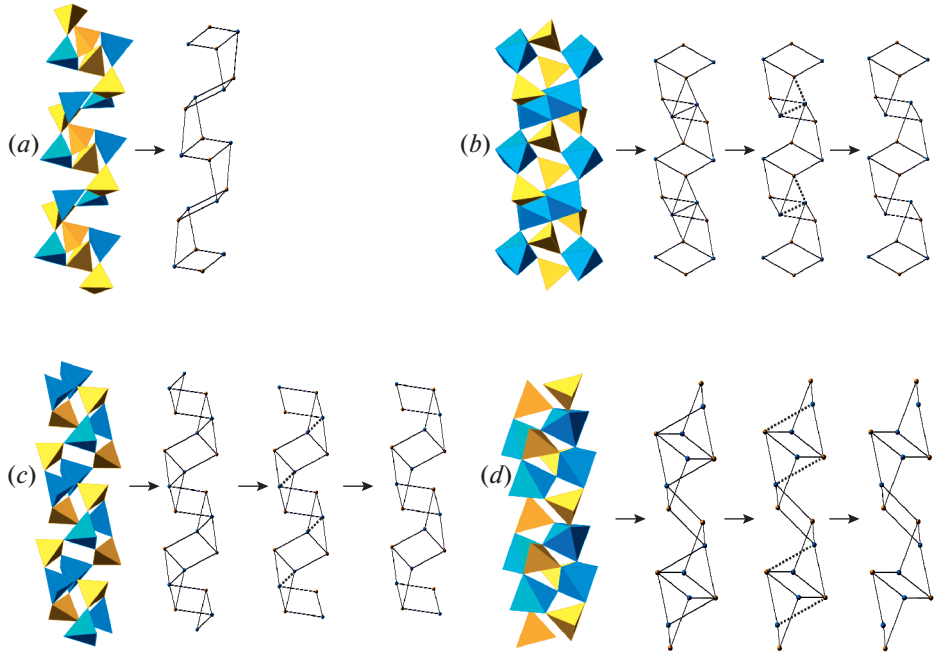

Fig. 17. The crankshaft chains in "anorthite-III" (*a*, *b*, *c*, *d* for the chains **1**, **2**, **3**, **4** as denoted by dashed lines in Fig. 16). For each chain the following diagrams are given (as indicated by arrows): polyhedral representation → graph → graph with high-pressure-induced links shown as dashed lines → graph without high-pressure-induced links. Legend as in Fig. 6.

Рис. 17. Карданные цепочки в "анортите-III" (*a*, *b*, *c*, *d* для цепочек **1**, **2**, **3**, **4**, выделенных точечными линии на рис. 16). Для каждой цепочки даны следующие диаграммы: полиэдрическое изображение → граф → граф с дополнительными связками, обусловленными действием высоких давлений → граф без дополнительных связок. Условные обозначения как на рис. 6.

*5.3. High-pressure behavior of structures with the **pcl** framework topology*

5.3.1. General features. In contrast to the **fsp** topology, the **pcl** topology is flexible and allows cooperative rotations of adjacent crankshaft chains with opening and closure of the channels outlined by 8-membered tetrahedral rings. The two opposite cases are shown in Fig. 18. The calculation of the area of the 8-membered ring (highlighted in grey color) shows that the volumes of the channels for the two cases differs by the factor of *ca*. 1.6. The closure of the 8-membered ring results in the shortening of the distance between the nodes located on the opposite sides of the ring. If **a** is the edge length (assumed to be equal for both diagrams shown in Fig. 18), then, for the ring with the maximal opening (Fig. 18*a*), the **A'A"** distance is equal to ~2.4**a**, and, due to the ring closure, the resulting distance becomes equal to **a**. Such a dramatic shortening provides the possibility of the formation of new bonds across the channels and this is exactly what happens for the structures with flexible crankshaft-chain-based topologies.

The transition from the left to the right diagram in Fig. 18 results in the graph with all edges oriented in two mutually orthogonal directions, which allows us to indicate this kind of transformation as *orthogonalization* (Krivovichev, 2014b).

Based upon the observations of the high-temperature behavior of the framework structures with the **pcl** topology (Pakhomova et al., 2017, 2019; Gorelova et al., 2019), the following general scenario can be formulated:

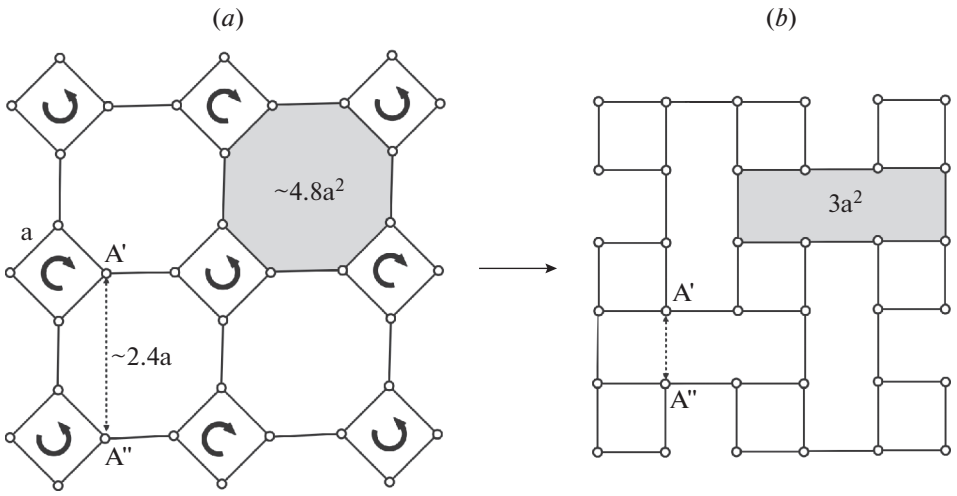

Fig. 18. The transformation of the regular net with four- and eight-membered rings in the course of orthogonalization. The arrows indicate the rotation directions of the four-membered rings.

Рис. 18. Трансформация симметричной сетки из 4- и 8-членных колец в результате ортогонализации. Стрелки указывают направления вращения 4-членных колец.

(i) orthogonalization of the framework topology induced by the cooperative rotation of adjacent crankshaft chains around their axes, which results in the closure of the 8-membered rings and the formation of additional T–O bonds across the channels; the transition is displacive with the appearance of new bonds, which may occur in a stepwise fashion (hence, several phase sub-transitions); the transitions of this kind are usually isosymmetric with the conservation of the space-group type; large M-cations migrate from the center of the channels to the open space within its walls;

(ii) formation of close-packed arrangements of anions (O) and large cations (M) with voids occupied by T cations; the coordination numbers of the T cations may vary from four to six.

It is of interest that the phase transitions driven by the orthogonalization of underlying topology is not restricted to the structures with the **pcl** topology. Gorelova et al. (2018, 2020) investigated high-pressure behavior of datolite and hingganite-(Y), two minerals based upon tetrahedral layers with the $4^1 8^1$ topology (Fig. 18). In the case of datolite, the closure of the 8-membered rings promotes the fivefold coordination of Si through the formation of additional Si–O bond across the ring (Gorelova et al., 2018). In hingganite-(Y), the same mechanism results in the approaching of the fifth O atom to the Si site with the formation of the [4+1] coordination that includes the Si–O distance of 2.10 Å at ~47 GPa (Gorelova et al., 2020).

The orthogonalization mechanism is not restricted to the high-pressure mineral transformations. Wadoski-Romejin and Armbruster (2013) investigated the high-temperature behavior of gismondine, $Ca_4[Al_8Si_8O_{32}] \cdot 18H_2O$, where stepwise dehydration drives the rotation of the crankshaft chains of the flexible **GIS** topology in order to fill the empty intraframework space and ends up with the reconfiguration of the T–T links and the formation of the inflexible "Ca-feldspar" structure (see above).

Below we briefly review the recent results on the high-pressure behavior of the minerals based upon the **pcl** topology, which generally follows the two-stage scenario sketched above.

5.3.2. High-pressure phase transitions of danburite. The crystal structure of danburite, $Ca[B_2Si_2O_8]$, is based upon the **pcl**-type framework with the topochemical symmetry *Pnam* that allows for the existence of Si–O–Si and B–O–B links in the direction parallel to the ex-

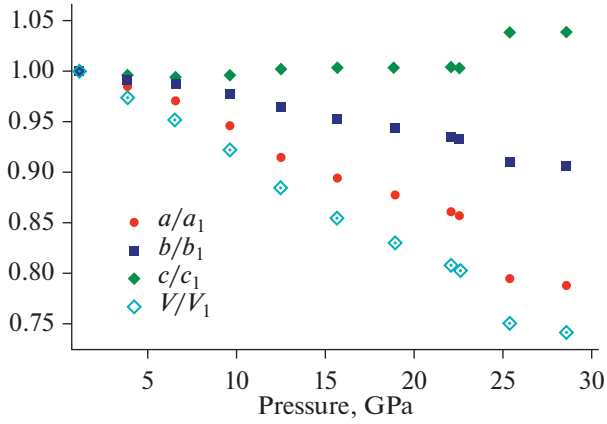

Fig. 19. The high-pressure evolution of the normalized unit-cell parameters of danburite [after Pakhomova et al. (2017)].

Рис. 19. Эволюция нормализованных значений параметров элементарной ячейки данбурита в зависимости от давления [по работе (Pakhomova et al., 2017)].

tension of the crankshaft chains, i.e. to the *c* axis (see above). Fig. 19 shows the evolution of the normalized unit-cell parameters of danburite in the pressure range 0–30 GPa, where the **pcl** framework topology is generally conserved [taken from the Supplementary Information of Pakhomova et al. (2017)]. It can be seen that, while the *c* axis does not essentially compress (and even experiences an anomalous increase at ~23 GPa), the *a* and *b* parameters decrease, which supports the orthogonalization mechanism resulting in the closure of the 8-membered rings. At ~23 GPa, the isosymmetric phase transition occurs, which manifests itself in the discontinuity of the *a* and *b* parameters. The sudden compression of the structure in the *ab* plane corresponds to the formation of the additional Si–O bond across the channel. The projection of the crystal structure of the new phase, danburite-II, is shown in Fig. 20*d* in comparison with the structure of danburite-I, and their B_2Si_2 nets (Figs. 20a, b). The comparison of Figs. 20*a* and *b* is particularly instructive, as it demonstrates the validity of the orthogonalization mechanism driven by the cooperative rotation of the crankshaft chains. The comparison of Figs. 20*c* and *d* indicates that the Ca atoms migrate from the central parts of the 8-membered rings to the walls of the channels, which favors the densification of the structure. It should be noted that danburite-II is the first ever known inorganic silicate with Si in exclusively fivefold coordination [the second one is datolite (Gorelova et al., 2018)].

At ~32 GPa, danburite-II transforms into danburite-III, a highly dense structure based upon the 3-layer **ABC** cubic close packing (c.c.p.) of anions (O) and large cations (Ca). The Si and B atoms reside in the octahedral and tetrahedral cavities, respectively. The structure of danburite-III is depicted in Fig. 21. It can be described as consisting of chains of edge-sharing (SiO_6) octahedra interlinked by [B_2O_7] tetrahedral dimers, which remain almost intact (not counting the bond-length and bond-angle changes) during the whole high-pressure range.

5.3.3. High-pressure phase transitions of paracelsian. Paracelsian, $Ba[Al_2Si_2O_8]$, is based upon the **pcl**-framework with the $P2_1/a$ topochemical space group (= $P2_1/c$ in the standard setting). Its high-pressure behavior is more complicated than that of danburite, but equally follows the two-stage scenario (Gorelova et al., 2019). There are at least one isosymmetric phase transition at ~7 GPa, from paracelsian-I to paracelsian-II, driven by the formation of new Si–O and Al–O bonds across the 8-membered rings compressed due to the orthogonalization. The formation of new bonds is stepwise, so, technically speaking, paracelsian-II is not

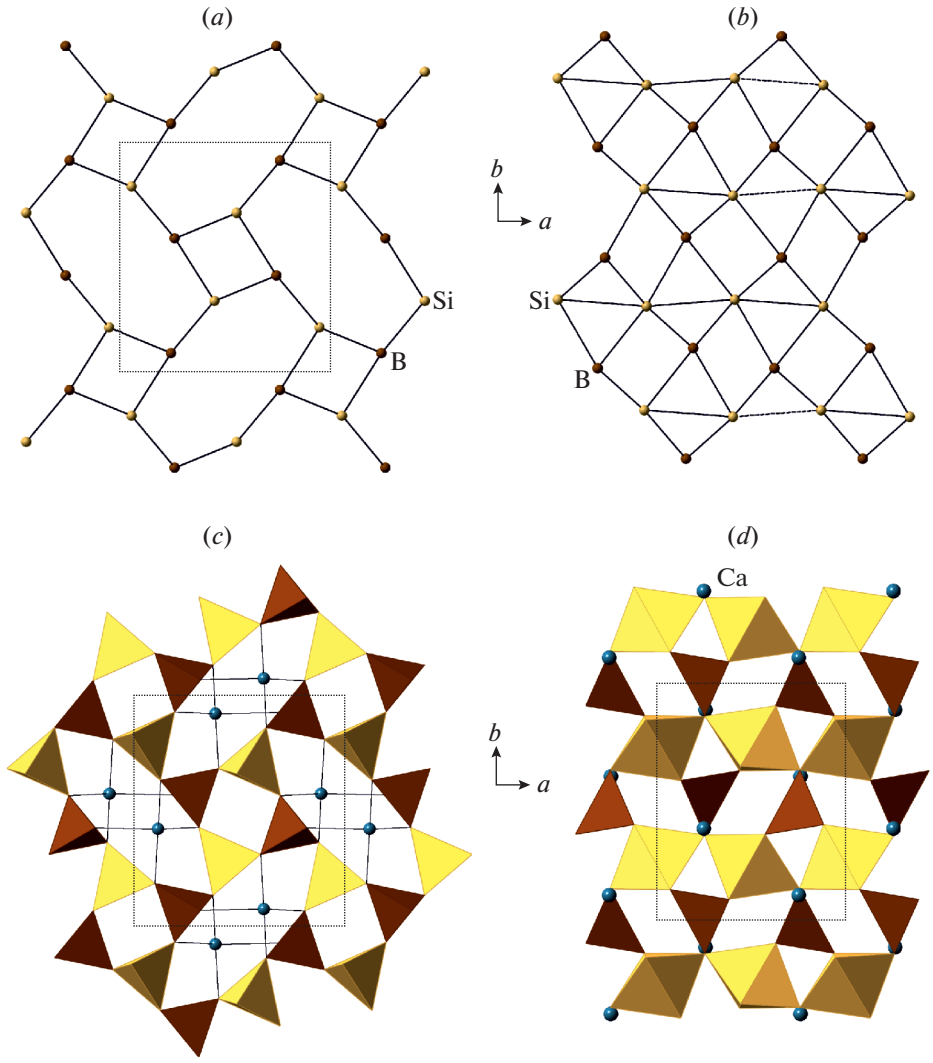

Fig. 20. The B_2Si_2 nets in danburite-I (room pressure; *a*) and "danburite-II" (*b*) projected along the *c* axis, and the crystal structures of danburite-I and "danburite-II" (*c* and *d*, respectively) projected along the *c* axis. The Si atoms (polyhedral) and B atoms (polyhedral) are shown in yellow and brown, respectively.

Рис. 21. Сетки B_2Si_2 в данбурите (обычные давления; *a*) и высокобарическом "данбурите-II" (*b*) в проекциях вдоль оси *c* и кристаллические структуры данбурита и "данбурита-II" (*c, d* соответственно) в проекциях вдоль оси *c*. Атомы (полиэдры) кремния и бора показаны желтым и коричневым цветами соответственно.

a single phase but can be classified into the IIa, IIb and IIc phases, which possess slightly different Al–O and Si–O bonding patterns. Upon compression above 28 GPa, the new phase, paracelsian-III, is observed that corresponds to the second stage of the scenario outlined in section 5.3.1. Its space group is $Pna2_1$ and it is based upon the 9-layer **ABACACBCB** close packing of O and Ca atoms with Si and Al distributed over different interstices. The location of the T atoms in the voids is asymmetrical, which results in the variations of their coordination number from 4 to 6. Gorelova et al. (2019) observed another phase transition, paracelsian-III → paracelsian-IV,

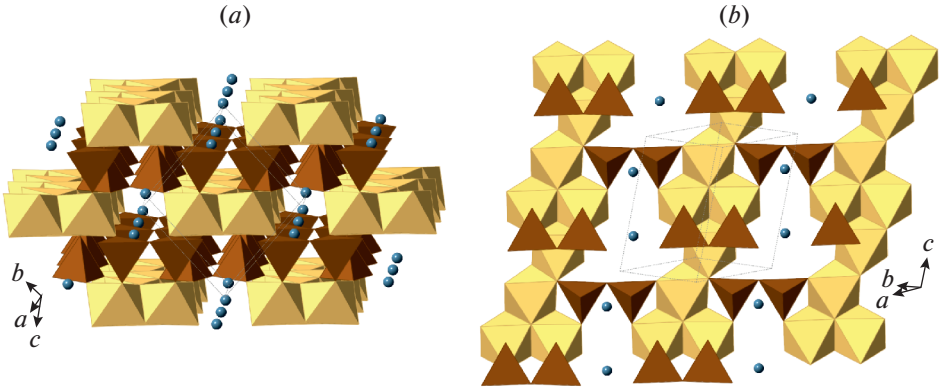

Fig. 21. The projections of the crystal structure of danburite-III. Legend as in Fig. 20.

Рис. 21. Проекции кристаллической структуры данбурита-III. Условные обозначения как на рис. 20.

which conserves the basic atomic arrangement of paracelsian-III, but is associated with the increasing densification of the structure and the symmetry reduction $Pna2_1 \rightarrow Pn$.

5.3.4. High-pressure phase transitions of hurlbutite. As it was shown by Bakakin and Belov (1961), hurlbutite, $Ca[Be_2P_2O_8]$, is isotypic to paracelsian. The high-pressure behavior of hurlbutite up to 90 GPa was studied by Pakhomova et al. (2019), who discovered in this pressure region three new phase transitions and three new $Ca[Be_2P_2O_8]$ polymorphs. Again, the behavior obeys the two-stage scenario (section 5.3.1). In the $P2_1/c$ setting of the **pcl**-type topology, the crankshaft chains run along the *a* axis, which is the least compressible axis in hurlbutite (see the high-pressure evolution of normalized unit-cell parameters of hurlbutite in Fig. 22), in good agreement with the orthogonalization mechanism. The first phase transition, hurlbutite-I $\rightarrow$ hurlbutite-II, occurs between 70 and 75 GPa and corresponds to the closure of the 8-membered ring and the formation of the new Be–O bond across the ring and the new (BeO_5) coordination polyhedron. The second transition, hurlbutite-II $\rightarrow$ hurlbutite-III, at ~ 83 GPa, corresponds to the formation of (PO_5) polyhedron, again due to the formation of the P–O bond across the ring. Thus, the orthogonalization stage in hurlbutite includes two phase transitions (both are isosymmetric). The third phase transition, hurlbutite-III $\rightarrow$ hurlbutite-IV, results in the compactification of the structure *via* the formation of the 12-layer **ABCACABCBCAB** close packing of Ca and O atoms with Be and P in octahedral voids. The structure (space group $P\bar{1}$) can be described as an arrangement of face- and edge-sharing (BeO_6) and (PO_6) octahedra with Ca^{2+} cations in the interstices (Fig. 23*a*). In the P2-Be4 and P4-Be2 dimers of face-sharing octahedra (Fig. 23*b*), the Be···P distances are in the range 2.29–2.32 Å. According to Pakhomova et al. (2019), hurlbutite-II, -III, and -IV are the first examples of experimentally observed inorganic compounds possessing beryllium with coordination numbers higher than four.

6. MASKELYNITE AND AMORPHIZATION OF PLAGIOCLASES

In addition to the natural crystalline feldspar polymorphs considered above, X-ray amorphous glass phases are of petrological and mineralogical importance. Maskelynite is the glassy analogue of plagioclase that was first reported by Tschermak (1872, 1883) from Shergotty achondrite. Later maskelynite was found in numerous meteorites as well as terrestrial impactites. There are two basic mechanisms suggested for its formation: (i) maskelynite is a diaplectic glass formed by shock-induced *solid-state* transformation of primary plagioclase (Engel-

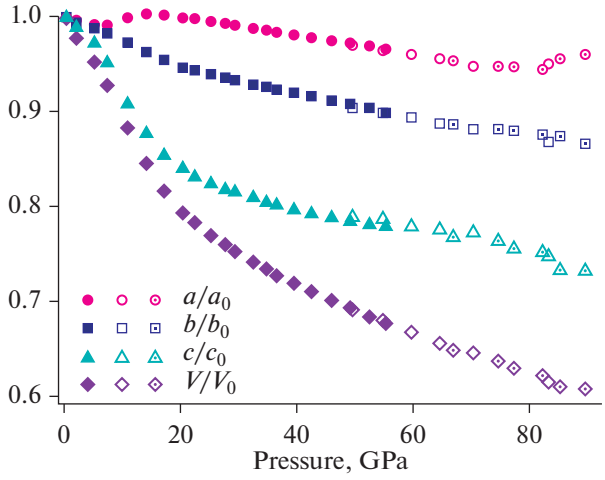

Fig. 22. The high-pressure evolution of the normalized unit-cell parameters of hurlbutite [after Pakhomova et al. (2019)].

Рис. 22. Эволюция нормализованных значений параметров элементарной ячейки херлбатита в зависимости от давления [по работе (Pakhomova et al., 2019)].

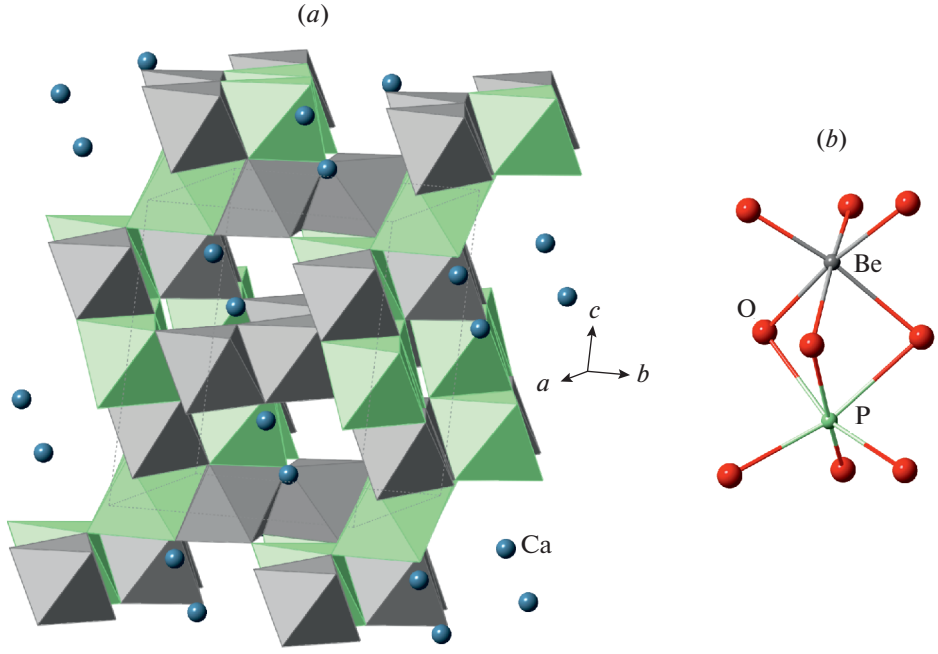

Fig. 23. The crystal structure of "hurlbutite-IV" as a framework of BeO_6 (grey) and PO_6 (light-green) octahedra with Ca^{2+} cations in cavities (*a*) and the dimer of face-sharing BeO_6 and PO_6 octahedra (*b*).

Рис. 23. Кристаллическая структура высокобарического "херлбатита-IV" как трехмерного каркаса из октаэдров BeO_6 (показаны серым) и PO_6 (показаны светло-зеленым) с катионами Ca^{2+} в пустотах (*a*) и димер из октаэдров BeO_6 и PO_6, связанных по общей грани (*b*).

hardt et al., 1967); (ii) it is a glass formed by quenching of *melt* formed due to shock at high pressures (Chen, El Goresy, 2000). The difference between the two processes is in the presence of melting induced by the shock, and there is no general consensus as to which mechanism (or both) occur in nature.

The amorphization of plagioclases has been the subject of extensive experimental studies (Sims et al., 2019, and references therein). The dependence of amorphization pressure upon the compression rate was studied by Sims et al. (2019), who reported, in accord with the previous results (Redfern, 1996; Daniel et al., 1997; Tomioka et al., 2010), the higher amorphization pressures for albite compared to anorthite. In particular, Daniel et al. (1997) observed the full amorphization of anorthite at ~16 GPa, and the phase transition of the $I\bar{1}$ anorthite into "a phase of higher symmetry" at ~10 GPa. The latter phase is most probably the same as "anorthite-III" reported by Pakhomova et al. (2020), which, however, has the lower symmetry compared to the $I\bar{1}$ anorthite. The different behavior of albite and anorthite under high pressures is evident from their structural topologies [the ground-breaking results by Pakhomova et al. (2020) are especially instructive]: in albite, there is a silicate substructure based upon the Si–Si links, which separates from the more "fluid" Al substructure under compression. In contrast, in the ideal anorthite topology, the Si–Si links are absent and the tetrahedral framework is more vulnerable to the external stress.

7. STRUCTURAL COMPLEXITY: INFORMATION-BASED ANALYSIS

7.1. Methods

In accord with our previous proposals (Krivovichev, 2012, 2013a, b, 2014a, 2016a, b, 2018), the crystal-structure complexity is estimated as the amounts of structural Shannon information per atom ($^{str}I_G$) and per unit cell ($^{str}I_{G,\,total}$) calculated according to the following equations:

$$^{str}I_G = -\sum_{(i=1)}^{k} p_i \log_2 p_i \quad (\text{bits/atom}), \tag{1}$$

$$^{str}I_{G,total} = -v\,I_G = -v\sum_{(i=1)}^{k} p_i \log_2 p_i \quad (\text{bits/cell}), \tag{2}$$

where k is the number of different crystallographic orbits in the structure and p_i is the random choice probability for an atom from the ith crystallographic orbit, that is:

$$p_i = m_i/v\,, \tag{3}$$

where m_i is a multiplicity of a crystallographic orbit (i.e. the number of atoms of a specific Wyckoff site in the reduced unit cell), and v is the total number of atoms in the reduced unit cell.

The analysis of different contributions to structural complexity is done using ladder diagrams as proposed in (Krivovichev, 2018) and implemented in (Gurzhiy, Plášil, 2019; Gurzhiy et al., 2019; Tymentseva et al., 2019).

Table 3 provides the list of topological and structural complexity parameters for the feldspar polymorphs with tetrahedral networks. The topological complexity parameters correspond to the aristotype structures with the highest possible symmetries of the tetrahedral networks. Table 4 lists structural complexity parameters for high-pressure feldspar polymorphs.

Fig. 24 shows ladder diagrams for different contributions to the total structural complexity of the structure types with the **fsp** and **pcl** topologies [we recall that there are six and two known structure types for these topologies, respectively (see sections 3.2.2 and 3.3.1 above)]. The important point is that the **pcl** topology is slightly *simpler* than the **fsp** topology in terms of Shannon information per atom and per unit cell. Among the structure types with the **fsp** topology, the structure type of anorthite $P\bar{1}$ is the most complex. For the **pcl** topology, the struc-

Table 3. Structural complexity parameters for the feldspar structure types with the tetrahedral network topologies (v in atoms per cell; I_G in bit per atom; $I_{G,total}$ in bit per cell)
Таблица 3. Параметры структурной сложности для полевошпатовых структурных типов с тетраэдрическими комплексами (v в атомах на ячейку; I_G в битах на атом; $I_{G,total}$ в битах на ячейку)

Space group	Reference structure	Framework complexity			Total complexity		
		v	I_G	$I_{G,total}$	v	I_G	$I_{G,total}$
			fsp topology				
$C2/m$*	Sanidine	24	2.752	66.039	26	2.931	76.211
$C\bar{1}$	Albite	24	3.585	86.039	26	3.700	96.211
$I\bar{1}$	Anorthite HT	48	4.585	220.078	52	4.700	244.423
$P\bar{1}$	Anorthite	96	5.585	536.156	104	5.700	592.846
$I2/c$	Celsian	48	3.585	172.078	52	3.700	192.423
$P2_1/c$	"Pb-feldspar"**	96	4.585	440.156	104	4.700	488.846
			pcl topology				
$Cmcm$*	–	24	2.252	54.039	–	–	–
$Pnam$	Danburite	48	2.752	132.078	52	2.931	152.423
$P2_1/a$	Paracelsian	48	3.585	172.078	52	3.700	192.423
			bct topology				
$I4/mmm$*	BCT	12	1.585	19.020	–	–	–
$P2_1$	Svyatoslavite	24	3.585	86.039	26	3.700	96.211
			dms topology				
$P6/mmm$*	γ-hexacelsian	12	1.459	17.510	14	1.985	27.793
$P6_3/mcm$	α-hexacelsian	24	1.459	35.020	26	1.738	45.192
$P312$	Dmisteinbergite	24	2.792	67.020	26	3.046	79.192

* Aristotype structures for Al–Si tetrahedral networks.
** Synthetic compound (Curetti et al., 2015).

Table 4. Structural complexity parameters for the high-pressure feldspar polymorphs (v in atoms per cell; I_G in bit per atom; $I_{G,total}$ in bit per cell)*
Таблица 4. Параметры структурной сложности для высокобарических полевошпатовых полиморфов (v в атомах на ячейку; I_G в битах на атом; $I_{G,total}$ в битах на ячейку)

Polymorph	Space group	Structural complexity		
		v	I_G	$I_{G,total}$
Albite-II	$P\bar{1}$	26	3.700	96.211
Albite-III	$P\bar{1}$	52	4.700	244.423
Anorthite-II	$I\bar{1}$	52	4.700	244.423
Anorthite-III	$P\bar{1}$	104	5.700	592.846
Microcline-II	$P\bar{1}$	26	3.700	96.211
Paracelsian-II	$P2_1/c$	52	3.700	192.423
Paracelsian-III	$Pna2_1$	52	3.700	192.423
Paracelsian-IV	Pn	52	4.700	244.423
Danburite-II	$Pnam$	52	2.931	152.423
Danburite-III	$P\bar{1}$	26	3.700	96.211
Hurlbutite-II	$P2_1/c$	52	3.700	192.423
Hurlbutite-III	$P2_1/c$	52	3.700	192.423
Hurlbutite-IV	$P\bar{1}$	52	4.700	244.423

* See Table 1 for detailed crystallographic information.

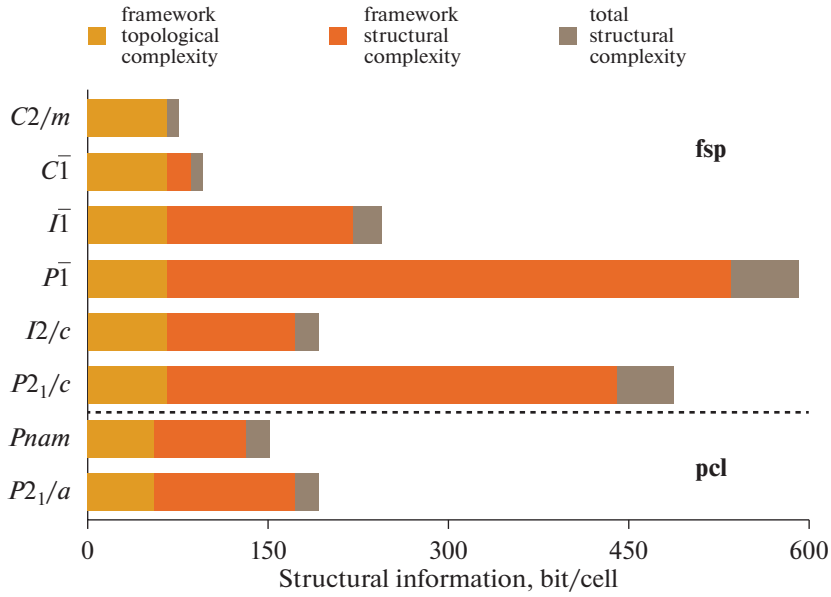

Fig. 24. The ladder diagrams for the structure types of the feldspar polymorphs with **fsp** and **pcl** topologies.

Рис. 24. Ступенчатые диаграммы для структурных типов полиморфов полевых шпатов с топологиями **fsp** и **pcl**.

ture type of paracelsian is more complex than that of danburite, obviously due to the fact that the $P2_1/a$ group of paracelsian ($P2_1/c$ in standard setting) is a subgroup of the *Pnam* group of danburite.

7.2. Structural complexity and thermodynamic parameters

The behavior of structural complexity with the change of temperature and pressure were preliminarly considered by Krivovichev (2013a). Generally, structural complexity decreases with the increasing temperature, which can be explained by the increase in total entropy, including configurational entropy, which is associated with Shannon structural information (Krivovichev, 2016a). This principle is valid for the feldspar polymorphism as well. There are several examples of FFMs, for which complexity is decreasing with the increasing temperature (below the arrow indicates the direction of the higher temperature with structural information per cell in square brackets):

(i) albite [86.039] → "monalbite" [66.039];

(ii) anorthite $P\bar{1}$ [592.846] → anorthite I [244.423];

(iii) $I\bar{1}$ [244.423] → $I2/c$ [192.423] for synthetic $Ca_{0.2}Pb_{0.8}[Al_2Si_2O_8]$ (Benna et al., 2000).

In contrast, the behavior of structural complexity under high pressure is irregular and does not demonstrate any obvious trends. The illustrative example is the evolution of structural information during pressure-induced phase transitions in $Ca_{0.2}Sr_{0.8}[Al_2Si_2O_8]$ (Benna et al., 2007) (the arrow indicates the direction of the increasing pressure with structural information per cell in square brackets): $I\bar{1}$ [244.423] → $I2/c$ [192.423] → $P2_1/c$ [488.846].

It is of interest that the isosymmetric phase transitions induced by orthogonalization in the structures with the **pcl** topology does not result in any changes of structural complexity, except for the changes in physical and information densities.

7.3. Structural complexity and metastability

7.3.1. The Ostwald rule of stages and the Goldsmith"s simplexity principle. The Ostwald step rule is an empirical rule that a crystallizing system first forms a sequence of metastable phases before forming the stable phase (Ostwald, 1897). There are different interpretations of this rule that take into account structures of precursors in solutions and melts, competition between surface energy and polymorphism, etc. (Navrotsky, 2004). Goldsmith (1953) observed that metastable polymorphs that crystallize according to the Ostwald rule are usually less complex that the final stable product in the sequence. For instance, disordered dolomite (or high-magnesium calcite), (Ca, Mg)CO_3, that has Ca and Mg disordered over the same cation site forms metastably before dolomite, $CaMg(CO_3)_2$, that has a fully ordered distribution of Ca and Mg in its crystal structure. Morse and Casey (1988) provided many other similar examples, and quantitative verification of the Goldsmith"s principle was considered in detail in (Krivovichev, 2013a). The polymorphism in FFMs provides at least three examples of the applicability of the Goldsmith's principle to the Ostwald sequences of phases during metastable crystallization.

7.3.2. Sanidine, orthoclase, microcline. The three $K[AlSi_3O_8]$ polymorphs with the **fsp** topology differ in the degree of the Al/Si ordering with sanidine and orthoclase ($C2/m$) being the metastable phases, which transform into microcline ($C\bar{1}$) with time. Therefore, the sanidine → orthoclase → → microcline sequence is the Ostwald cascade of phases initiated by the metastable crystallization of sanidine. The transition is associated with the ordering of Al and its incorporation into the $T_1$0 site. Along the sequence, the complexity is increasing from 76.211 to 96.211 bit per cell for the $C2/m$ to $C\bar{1}$ structure types, respectively. This kind of behavior agrees well with the Goldsmith's simplexity principle. The topological complexity remains the same for all three polymorphs.

7.3.3. Anorthite, svyatoslavite, dmisteinbergite. As it was mentioned in sections 3.4.2 and 3.5.2, svyatoslavite and dmisteinbergite are metastable kinetically stabilized polymorphs of anorthite, which is the thermodynamically stable phase. The sequence "svyatoslavite + dmisteinbergite → anorthite" is the Ostwald sequence, which conforms to the Goldsmith's principle. Fig. 25 shows the ladder diagram for anorthite $P\bar{1}$ and $I\bar{1}$, svyatoslavite and dmisteinbergite. The $[Al_2Si_2O_8]$ tetrahedral networks in svyatoslavite and dmisteinbergite are topologically simpler (19.020 and 17.510 bit/cell, respectively) than that in anorthite (66.039 bit/cell). The same is also true for the total structural complexity, which is 6–8 times higher for anorthite (592.846 bit/cell) than for svyatoslavite (96.211 bit/cell) and dmisteinbergite (79.192 bit/cell). Thus the Goldsmith"s principle is valid for the tetrahedral $Ca[Al_2Si_2O_8]$ polymorphs in terms of both topological and full structural complexity.

7.3.4. Hexacelsian, paracelsian, celsian. Li et al. (2020) described the Oswald sequence of phases during the crystallization of celsian as hexacelsian → paracelsian → celsian. This sequence corresponds to the general increase in the combination of structural and topological complexity (in bit/cell; topological information given in square brackets): 35.020 [17.510] → → 172.078 [54.039] → 172.078 [66.039]. Note that the total structural complexities for celsian and paracelsian are identical, but the **fsp**-framework in celsian is topologically more complex than that (**pcl**) in paracelsian. This behavior agrees with the Goldsmith"s principle.

7.4. Algorithmic complexity

The complexity measured as a Shannon information is static in character and reflects the size of a system and the diversity of its components. In contrast, an algorithmic complexity corresponds to the complexity of constructing the system from its elementary parts and thus is dynamic in character. Krivovichev et al. (2012) proposed, whereas Krivovichev (2014b) further developed the theory of orthogonal structural deterministic finite automata (SDFA) to describe the algorithmic complexity of networks in the crystal structures of FFMs with tetrahedrally coordinated T atoms. Here the complexity is understood in terms of the number of

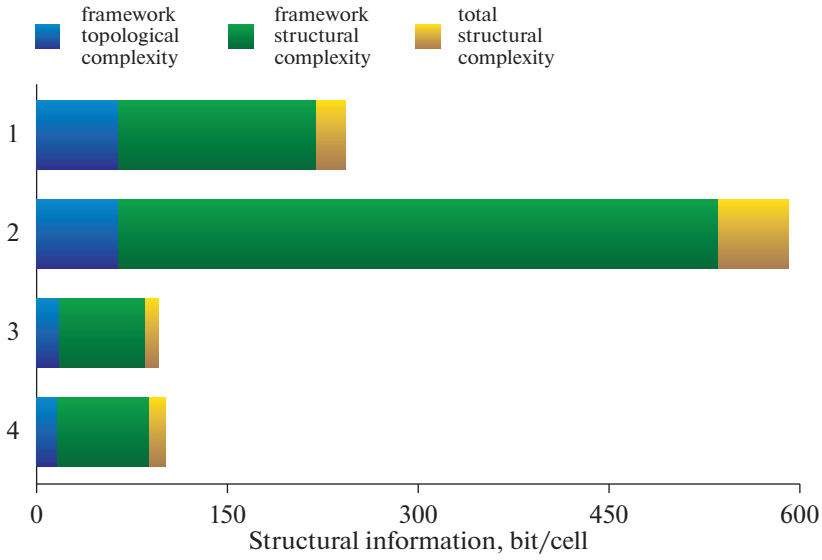

Fig. 25. The ladder diagrams for the $Ca[Al_2Si_2O_8]$ polymorphs with tetrahedral topologies: **1** – anorthite *P*; **2** – anorthite *I*; **3** – dmisteinbergite; **4** – svyatoslavite.
Рис. 25. Ступенчатые диаграммы для полиморфов $Ca[Al_2Si_2O_8]$ с тетраэдрическими топологиями: **1** – анортит *P*; **2** – анортит *I*; **3** – дмиштейнбергит; **4** – святославит.

nodes and links of the state diagrams of network-generating SDFA. The construction of the SDFA that generate the **fsp**, **bct** and **dms** topologies provides the sequence of complexities **fsp** > **bct** > **dms**, which agrees with the information-based estimates (Table 2). However, the **pcl**-generating SDFA is much more complex than that of the **fsp** network, in contrast to the numerical data obtained by the Shannon information approach. This shows that the algorithmic approach requires more investigation and perhaps the change of the general methodology.

8. SUMMARY

In this review, we have touched upon the various aspects of polymorphism in the feldspar family of minerals. Below we summarize the basic points of the review.

1. The feldspar family is defined as consisting of minerals and synthetic compounds with the general formula $M^{n+}[T_4^{k+}O_8]$, where n is the average charge of the M^{n+} cation (n = 1–2; $M^{n+} = Na^+$, K^+, Rb^+, $(NH_4)^+$, Ca^{2+}, Sr^{2+}, Ba^{2+}), k is the average charge of the T^{k+} cation ($k = 4 - n/4$; $T^{k+} = Be^{2+}$, Zn^{2+}, Al^{3+}, B^{3+}, Fe^{3+}, Si^{4+}, As^{5+}, P^{5+}). The feldspar-family member has a crystal structure based upon d-dimensional network of (TO_m) coordination polyhedra sharing O atoms, $d = 2$ or 3 (layers or frameworks), and $m = 4$, 5 or 6 (coordination of the T atoms in minerals is either tetrahedral or octahedral). The M:T ratio of 1 : 4 should correspond to the ratio of the total numbers of M and T sites in the unit cell. Cymrite, $Ba[Al_2Si_2O_8](H_2O)$, and "K-cymrite", $K[AlSi_3O_8](H_2O)$, are considered as members of the feldspar family, due to their close similarity to hexacelsian and kokchetavite, respectively. There are twenty-nine valid mineral species known to date that can be assigned to the feldspar family. Maskelynite is the natural X-ray amorphous feldspar polymorph (glass) with the plagioclase composition.

2. From the structural point of view, all feldspar polymorphs can be classified into two groups: those containing T atoms in tetrahedral coordination only and those containing T atoms in non-tetrahedral coordination. There are four basic topologies of feldspar-family tetrahedral networks: **fsp** (3D; feldspar *sensu stricto*; eleven mineral species), **pcl** (3D; paracelsian; seven mineral species), **bct** (3D, svyatoslavite; two mineral species), and **dms** (2D; dmisteinbergite; six mineral species). There are three minerals that contain T atoms in exclusively octahedral (sixfold) coordination; all these minerals belong to the hollandite structure type (including its distorted varieties). All other feldspar polymorphs have been obtained during high-pressure and high-temperature experiments on natural crystals.

3. The high-pressure phase transitions have been investigated in details for the structures with the **fsp** and **pcl** topologies. The high-pressure behavior of the members of these two groups is different and governed by the distinction of the **pcl** and **fsp** topologies as flexible and inflexible, respectively. For the flexible **pcl** topology, the high-pressure phase transitions consist of two stages: (i) orthogonalization of the framework topology induced by the cooperative rotation of adjacent crankshaft chains around their axis, which results in the appearance of new T–O bonds across the 8-membered rings; the transitions of this kind are usually isosymmetric; (ii) formation of close-packed arrangements of anions (O) and large cations (M) with voids occupied by T cations; the coordination numbers of the T cations may vary from four to six. The mechanism of the high-pressure behavior for the **fsp** structures does not involve rotation of crankshaft chains and depends upon the Al:Si ratio. For the 1:3 ratio (albite, microcline), the formation of high-pressure polymorphs follows the same scenario: (i) breaking of crankshaft chains; (ii) formation of the okenite-type $[Si_3O_8]$ chains of corner-sharing (SiO_4) tetrahedra; (iii) separation of Al into dimers of edge-sharing (AlO_n) polyhedra ($n = 5, 6$) associated with the change in the coordination number of Al; (iv) (possible) breaking of the okenite chains into triple rings with the formation of dimers of edge-sharing (SiO_5) square pyramids linking the rings into layers. For the 1:1 ratio (anorthite), the phase transition proceeds via the reconstruction of the crankshaft chains and formation of 5- and 6-coordinated Al.

4. The analysis of structural complexity by means of the Shannon information theory indicates the following general trends: (i) structural complexity decreases with the increasing temperature, which can be explained by the increase in total entropy, including configurational entropy associated with the Shannon structural information; (ii) at least three Ostwald sequences of phase formation can be recognized in the feldspar family: sanidine → orthoclase → → microcline, svyatoslavite + dmisteinbergite → anorthite, hexacelsian → paracelsian → celsian; in these sequences kinetically stabilized metastable phases are topologically simpler than the thermodynamically stable phases; transition from metastable to stable phases is associated with the gradual increase of topological and structural complexity; (iii) the high-pressure behavior of feldspar-family structures does not show any obvious trends in the evolution of structural complexity.

Despite the seemingly simple chemical composition, the feldspar polymorphism is extremely rich and complex and includes a number of structural phenomena: (i) coordination changes of intra- and extraframework cations; (ii) topological reconstructions, including changes in dimensionality; (iii) cation ordering, including Al/Si and M-cation ordering in solid solutions, resulting in the chemical stabilization of particular structure types and the formation of incommensurately modulated structures (in plagioclases); (iv) displacive distortions involving tilting of tetrahedra and rotations of crankshaft chains; (v) amorphization. In turn, the observed structural phenomena are controlled by temperature, pressure (including shock-induced transformations) and crystallization kinetics that may stabilize metastable phases with unique crystal structures.

Within the recent years, it was realized that polymorphism in feldspars is a much more common phenomenon than it was thought previously and the investigation of natural feldspar polymorphs sheds new light onto the magmatic and metamorphic processes in the Earth.

The reported study was funded by RFBR, project number 19-15-50064. I am grateful to Igor Pekov for the useful comments on the manuscript.

REFERENCES

Abe T., Tsukamoto K., Sunagawa I. Nucleation, growth and stability of $CaAl_2Si_2O_8$ polymorphs. *Phys. Chem. Miner.* **1991**. Vol. 17. P. 473–484.

Agarwal A., Reznik B., Kontny A., Heissler S., Schilling F. Lingunite-a high-pressure plagioclase polymorph at mineral interfaces in doleritic rock of the Lockne impact structure (Sweden). *Sci. Rep.* **2016**. Vol. 6. P. 25991.

Akatsuka K., Yasumori A., Maeda K. Structure of crystalline $CaAl_2Si_2O_8$ precipitated in a $CaO–Al_2O_3–SiO_2$ glass-ceramic. *Mater. Lett.* **2019**. Vol. 242. P. 163–165.

Alietti E., Brigatti M.F., Poppi L. Clintonite-1*M*: Crystal chemistry and its relationships to closely associated Al-rich phlogopite. *Amer. Miner.* **1997**. Vol. 82. P. 936–945.

Angel R.J. High-pressure structure of anorthite. *Amer. Miner.* **1988.** Vol. 73. P. 1114–1119.

Angel R.J. Feldspars at high pressure. In: *Feldspars and Their Reactions.* Ed. by *Parsons I.* Dordrecht: Kluwer Academic Publishers, **1994**. P. 271–312.

Appleman D.E., Clark J.R. Crystal structure of reedmergnerite, a boron albite, and its relation to feldspar crystal chemistry. *Amer. J. Sci.* **1965**. Vol. 50. P. 1827–1850.

Bakakin V.V., Belov N.V. The crystalline structure of hurlbutite. *Dokl. Acad. Sci.* USSR. **1959**. Vol. 125. P. 343–344 (*in Russian*).

Bakakin V.V., Belov N.V. Crystal structure of paracelsian. *Sov. Phys. Crystallogr.* **1961**. Vol. 5. P. 826–829 (*in Russian*).

Bakakin V.V., Kravchenko V.B., Belov N.V. The crystalline structure of danburite $CaB_2Si_2O_8$ and hurlbutite $CaBe_2P_2O_8$. *Dokl. Acad. Sci. USSR.* **1959**. Vol. 129. P. 1155–1158 (*in Russian*).

Barker D.S. Ammonium in alkali feldspars. *Amer. Miner.* **1964**. Vol. 49. P. 851–858.

Barrer R.M., Marshall D.J. Hydrothermal chemistry of silicates. Part XII. Synthetic strontium aluminosilicates. *J. Chem. Soc.* **1964**. Vol. 1964. P. 485–497.

Beck P., Gillet P., Gautron L., Daniel I., El Goresy A. A new natural high-pressure (Na,Ca)-hexaluminosilicate $[(Ca_xNa_{1-x})Al_x^{3+}Si_{3-x}O_{11}]$ in shocked Martian meteorites. *Earth Planet. Sci. Lett.* **2004**. Vol. 219. P. 1–12.

Beck P., Gillet P., El Goresy A., Mostefaoui S. Timescales of shock processes in chondritic and Martian meteorites. *Nature.* **2005**. Vol. 435. P. 1071–1074.

Beck P., Ferroir T., Gillet P. Shock-induced compaction, melting, and entrapment of atmospheric gases in Martian meteorites. *Geophys. Res. Lett.* **2007**. Vol. 34. P. L01203.

Benna P., Tribaudino M., Bruno E. $I\bar{1} - I2/c$ ferroelastic phase transition in the $Ca_{0.2}Pb_{0.8}Al_2Si_2O_8$ feldspar as a function of temperature. *Miner. Mag.* **2000**. Vol. 64. P. 285–290.

Benna P., Nestola F., Boffa Ballaran T., Balić-Žunić T., Lundegaard L. F., Bruno E. The high-pressure structural configurations of $Ca_{0.2}Sr_{0.8}Al_2Si_2O_8$ feldspar: The $I\bar{1} - I2/c$ and $I2/c - P2_1/c$ phase transitions. *Amer. Miner.* **2007**. Vol. 92. P. 1190–1199.

Berger K., Range K.-J. High-pressure synthesis and structure refinement of strontium danburite, $SrB_2Si_2O_8$. *Z. Naturforsch.* **1996**. Bd. 51b. S. 172–174.

Bickford D., Lohman D.J., Sodhi N.S., Ng P.K.L., Meier R., Winker K., Ingram K.K., Das I. Cryptic species as a window on diversity and conservation. *Trends Ecol. Evol.* **2007**. Vol. 22. P. 148–155.

Blasi A., Blasi C.D.P. Aspects of alkali feldspar characterization: prospects and relevance to problems outstanding. In: *Feldspars and Their Reactions.* Ed. by *Parsons I.* Dordrecht: Kluwer Academic Publishers, **1994**. P. 51–102.

Boffa Ballaran T., Liu J., Dubrovinsky L. S., Caracas R., Crichton W. High-pressure ferroelastic phase transition in aluminosilicate hollandite. *Phys. Rev. B.* **2009**. Vol. 80. P. 214104.

Bolotina N.B., Rastsvetaeva R.K., Andrianov V.I., Kashaev A.A. Refinement of modulated crystals. Structure of kimrite. *Sov. Phys. Crystallogr.* **1991**. Vol. 36. P. 190–194 (*in Russian*).

Bolotina N.B., Rastsvetaeva R.K., Kashaev A.A. Refinement of the twinned structure of cymrite from the Ruby Creek deposit (Alaska). *Crystallogr. Rep.* **2010**. Vol. 55. P. 569–574.

Bontchev R.P., Sevov S.C. Synthesis and characterisation of a new cobalt aluminophosphate with an open-framework structure. *Chem. Mater.* **1997**. Vol. 9. P. 3155–3158.

Boruntea C.R., Vennestrøm P., Lundegaard L.F. K-paracelsian ($KAlSi_3O_8 \cdot H_2O$) and identification of a simple building scheme of dense double-crankshaft zeolite topologies. *IUCrJ.* **2019**. Vol. 6. P. 66–71.

Boysen H., Kek S. The modulated structure of labradorite. *Z. Kristallogr.* **2015**. Vol. 230. P. 23–36.

Brigatti M.F., Guggenheim S. Mica crystal chemistry and the influence of pressure, temperature, and solid solution on atomistic models. *Rev. Miner. Geochem.* **2002**. Vol. 46. P. 1–97.

Brown W.L., Hoffman W., Laves F. Über kontinuierliche und reversible Transformation des Anorthites ($CaAl_2Si_2O_8$) zwischen 25 und 350 °C. *Naturwiss.* **1963**. Bd. 50. S. 221.

Bruno E., Pentinghaus H. Substitution of cations in natural and synthetic feldspars. In: *The Feldpars.* Ed. by *MacKenzie W.S., Zussman J.* Manchester University Press, Manchester, UK, **1974**. P. 574–609.

Bu X.-H., Feng P.-Y., Gier T. E., Stucky G. D. Synthesis and crystal structure of feldspar analogs in beryllosilicate and aluminium-cobalt phosphate systems. *Micropor. Mesopor. Mater.* **1998**. Vol. 23. P. 323–330.

Bychkov A.M., Kotelnikov A.R., Romanenko I.M., Senderov E.E. The influence of isomorphous substitution of silicon by phosphorus upon the structural features of feldspars. *Geochemistry.* **1989**. N 2. P. 310–313 (*in Russian*).

Chao S.H., Taylor W.H. Isomorphous replacement and superlattice structures in the plagioclase felspars. *Proc. Royal. Soc. London.* **1940**. Vol. *A*176. P. 76–87.

Chen M., El Goresy A. The nature of maskelynite in shocked meteorites: not diaplectic glass but a glass quenched from shock-induced dense melt at high pressures. *Earth Planet. Sci. Lett.* **2000**. Vol. 179. P. 489–502.

Chesnokov B.V., Lotova E.V., Pavlyuchenko V.S., Nigmatulina E.N., Usova L.V., Bushmakin A.R., Nishanbaev T.P. Svyatoslavite, $CaAl_2Si_2O_8$ (orthorhombic), a new mineral. *Zapiski RMO* (*Proc. Russian Miner. Soc.*). **1989**. Vol. 118. P. 111–114 (*in Russian*).

Chesnokov B.V., Lotova E.V., Nigmatulina E. N., Pavlyuchenko V. S., Bushmakin A. F. Dmisteinbergite $CaAl_2Si_2O_8$ (hexagonal) – a new mineral. *Zapiski RMO* (*Proc. Russian Miner. Soc.*). **1990**. Vol. 119. P. 43–45 (*in Russian*).

Chiari G., Gazzoni G., Craig J.R., Gibbs G.V., Louisnathan S.J. Two independent refinements of the structure of paracelsian, $BaAl_2Si_2O_8$. *Amer. Miner.* **1985**. Vol. 70. P. 969–974.

Colville A.A., Ribbe P.H. The crystal structure of an adularia and a refinement of the crystal structure of orthoclase. *Amer. Miner.* **1968**. Vol. 53. P. 25–37.

Curetti N., Benna P., Bruno E. High-pressure equation of state and phase transition in $PbAl_2Si_2O_8$ feldspar. *Amer. Miner.* **2015**. Vol. 100. P. 1568–1577.

Dal Bo F., Hatert F., Baijot M. Crystal chemistry of synthetic $M^{2+}Be_2P_2O_8$ (M^{2+} = Ca, Sr, Pb, Ba) beryllophosphates. *Canad. Miner.* **2014**. Vol. 52. P. 337–350.

Daniel I., Gillet P., McMillan P.F., Richet P. An in-situ high-temperature structural study of stable and metastable $CaAl_2Si_2O_8$ polymorphs. *Miner. Mag.* **1995**. Vol. 59. P. 25–33.

Daniel I., Gillet P., McMillan P. F., Wolf G., Verhelst M. A. High-pressure behavior of anorthite: compression and amorphization. *J. Geophys. Res. Solid Earth.* **1997**. Vol. 102. P. 10313–10325.

Davis G.L., Tuttle O.F. Two new crystalline phases of the anorthite composition, $CaO–Al_2O_3–SiO_2$. *Am. J. Sci. Bowen Volume.* **1951**. Vol. 1. P. 107–114.

Day M.C., Hawthorne F.C. A structure hierarchy for silicate minerals: chain, ribbon, and tube silicates. *Miner. Mag.* **2020**. Vol. 84. P. 165–244.

Deer W.A., Howie R.A., Zusmann J. Rock-Forming Minerals. Vol. 4A. Framework Silicates: Feldspars. London: The Geological Society, **2001**. 973 p.

Dimitrijević R., Dondur V., Kremenović A. Thermally induced phase transformations of Ca-exchanged LTA and FAU zeolite frameworks: Rietveld refinement of the hexagonal $CaAl_2Si_2O_8$ diphyllosilicate structure. *Zeolites.* **1996**. Vol. 16. P. 294–300.

Dobson D.P., Thomas R.W., Mitchell T.M. Diffusion profiles around quartz clasts as indicators of the thermal history of pseudotachylytes. *Geochem. Geophys. Geosyst.* **2018**. Vol. 19. P. 4329–4341.

Dollase W.A., Ross C.R. Crystal structures of body-centered tetragonal tectosilicates: $K_{1.14}Mg_{0.57}Si_{1.43}O_4$, $K_{1.10}Zn_{0.55}Si_{1.45}O_4$, and $K_{1.11}Fe_{1.11}Si_{0.89}O_4$. *Amer. Miner.* **1993**. Vol. 78. P. 627–632.

Dordević T. $Ba(ZnAsO_4)_2 \cdot H_2O$, a non-centrosymmetric framework structure related to feldspar. *Eur. J. Miner.* **2011**. Vol. 23. P. 437–447.

Downs J.W., Swope R.J. The Laplacian of the electron density and the electrostatic potential of danburite, $CaB_2Si_2O_8$. *J. Phys. Chem.* **1992**. Vol. 96. P. 4834–4840.

Downs R.T., Pinch W.W., Thompson R.M., Evans S.H., Megaw L. Yangite, $PbMnSi_3O_8 \cdot H_2O$, a new mineral species with double wollastonite silicate chains from the Kombat mine, Namibia. *Amer. Miner.* **2016**. Vol. 101. P. 2539–2543.

Drits V.A., Kashaev A.A., Sokolova G.V. Crystal structure of cymrite. *Sov. Phys. Crystallogr.* **1975**. Vol. 20. P. 171–175 (*in Russian*).

Dunbar C., Machatschki F. Structure of danburite, $CaB_2Si_2O_8$. *Z. Kristallogr.* **1931**. Bd. 76. S. 133–146.

Dusmatov V.D., Popova N.A., Kabanova L.K. The first find of reedmergnerite in the USSR. *Dokl. Acad. Sci. Tadzh. SSR.* **1967**. Vol. 10. N. 10. P. 51–53 (*in Russian*).

El Goresy A., Chen M., Gillet P., Dubrovinsky L. S. Shock-induced high-pressure phase-transition of labradorite to hollandite "($Na_{47}–Ca_{51}–K_2$)" in Zagami and the assemblage hollandite "($Na_{80}–Ca_{12}–K_8$)" + jadeite in L chondrites: constraints to peak-shock pressures. *Meteor. Planet. Sci.* **2000**. Vol. 35. Suppl. P. A51.

Engelhardt W. v., Arndt J., Stöffler D., Müller W.F., Jeziorkowski H., Gubser R.A. Diaplektische Gläser in den Breccien des Ries von Nördlingen als Anzeichen für Stoß wellenmetamorphose. *Contrib. Miner. Petrol.* **1967**. Vol. 15. P. 91–100.

Erd R.C., White D.E., Fahey J.J., Lee D.E. Buddingtonite, an ammonium feldspar with zeolitic water. *Amer. Miner.* **1964**. Vol. 49. P. 831–851.

Fasshauer D.W., Chatterjee N.D., Marler B. Synthesis, structure, thermodynamic properties, and stability relations of K-cymrite, $K[AlSi_3O_8] \cdot H_2O$. *Phys. Chem. Miner.* **1997**. Vol. 24. P. 455–462.

Feldspars and Their Reactions. Ed. by *Parsons I.* Dordrecht: Kluwer Academic Publishers, **1994**. 650 p.

Ferraris G., Ivaldi G. Structural features of micas. *Rev. Miner. Geochem.* **2002**. Vol. 46. P. 117–153.

Ferrero S., Angel R. Micropetrology: are inclusions in minerals grains of truth? *J. Petrol.* **2018**. Vol. 9. P. 1671–1700.

Ferrero S., Ziemann M.A., Angel R., O"Brien P.J., Wunder B. Kumdykolite, kokchetavite and cristobalite crystallized in nanogranites from felsic granulites, Orlica-Snieznik Dome (Bohemian Massif): Not an evidence for ultrahigh pressure conditions. *Contrib. Miner. Petrol.* **2016**. Vol. 171. Paper 3.

Ferrero S., Godard G., Palmeri R., Wunder B., Cesare B. Partial melting of ultramafic granulites from Dronning Maud Land, Antarctica: Constraints from melt inclusions and thermodynamic modeling. *Amer. Miner.* **2018**. Vol. 103. P. 610–622.

Ferroir T., Onozawa T., Yagi T., Merkel S., Miyajima N., Nishiyama N., Irifune T., Kikegawa T. Equation of state and phase transition in $KAlSi_3O_8$ hollandite at high pressure. *Amer. Miner.* **2006**. Vol. 91. P. 327–332.

Filatov S.K., Krivovichev S.V., Burns P.C., Vergasova L.P. Crystal structure of filatovite, $K[(Al,Zn)_2(As,Si)_2O_8]$, the first arsenate of the feldspar group. *Eur. J. Miner.* **2004**. Vol. 16. P. 537–543.

Fintor K., Walter H., Nagy S. Petrographic and micro-Raman analysis of chondrules and (Ca,Al)-rich inclusions of NWA 2086 CV3 type carbonaceous chondrite. *Lunar Planet Sci.* **2013**. Vol. 44. Paper 1152.

Fintor K., Park C., Nagy S., Pál-Molnár E., Krot A. N. Hydrothermal origin of hexagonal $CaAl_2Si_2O_8$ (dmisteinbergite) in a compact type A CAI from the Northwest Africa 2086 CV3 chondrite. *Meteor. Planet. Sci.* **2014**. Vol. 49. P. 812–823.

Fleet M. Tetrahedral-site occupancies in reedmergnerite and synthetic boron albite ($NaBSi_3O_8$). *Amer. Miner.* **1992**. Vol. 77. P. 76–84.

Franz G., Khomenko V., Vishnyevskyy A., Wirth R., Struck U., Nissen J., Gernert U., Rocholl A. Biologically mediated crystallization of buddingtonite in the Paleoproterozoic: Organic-igneous interactions from the Volyn pegmatite, Ukraine. *Amer. Miner.* **2017**. Vol. 102. P. 2119–2135.

Fredrickson R.T., Fredrickson D.C. Communication between cation environments in aluminosilicate frameworks: incommensurately modulated crystal structure of an e-plagioclase. *Acta Crystallogr.* **2016**. Vol. B72. P. 787–801.

Galuskina I.O., Galuskin E.V., Vapnik Y., Prusik K., Stasiak M., Dzierżanowski P., Murashko M. Gurimite, $Ba_3(VO_4)_2$ and hexacelsian, $BaAl_2Si_2O_8$ – two new minerals from schorlomite-rich paralava of the Hatrurim Complex, Negev Desert, Israel. *Miner. Mag.* **2017**. Vol. 81. P. 1009–1019.

Gasperin M. Structure cristalline de $RbAlSi_3O_8$. *Acta Crystallogr.* **1971**. Vol. B27. P. 854–855.

Ghélis M., Gasperin M. Evolution des paramètres dans le système $KAlSi_3O_8$–$RbAlSi_3O_8$. *Compt. Rendu. Acad. Sci. D.* **1970**. Vol. 271. P. 1928–1929.

Ghose S., McMullan R.K., Weber H.-P. Neutron diffraction studies of the $P\bar{1} - I\bar{1}$ transition in anorthite, $CaAl_2Si_2O_8$ and the crystal structure of the body-centered phase at 514 K. *Z. Kristallogr.* **1993**. Vol. 204. P. 215–237.

Gillet P., Chen M., Dubrovinsky L., El Goresy A. Natural $NaAlSi_3O_8$-hollandite in the shocked Sixiangkou meteorite. *Science.* **2000**. Vol. 287. P. 1633–1636.

Goldsmith J.R. A "simplexity principle" and its relation to "ease" of crystallization. *J. Geol.* **1953**. Vol. 61. P. 439–451.

Gorelova L.A., Filatov S.K., Krzhizhanovskaya M.G., Bubnova R.S. High temperature behaviour of danburite-like borosilicates $MB_2Si_2O_8$ (M = Ca, Sr, Ba). *Phys. Chem. Glass. Eur. J. Glass Sci. Technol. B.* **2015**. Vol. 56. P. 189–196.

Gorelova L.A., Pakhomova A.S., Aprilis G., Dubrovinsky L.S., Krivovichev S.V. Pentacoordinated silicon in the high-pressure modification of datolite, $CaBSiO_4(OH)$. *Inorg. Chem. Front.* **2018**. Vol. 5. P. 1653–1660.

Gorelova L.A., Pakhomova A.S., Krivovichev S.V., Dubrovinsky L.S., Kasatkin A.V. High pressure phase transitions of paracelsian $BaAl_2Si_2O_8$. *Sci. Rep.* **2019**. Vol. 9. Paper 12652.

Gorelova L.A., Pakhomova A.S., Krivovichev S.V., Kasatkin A.V., Dubrovinsky L.S. Compressibility of hingganite-(Y): high-pressure single crystal X-ray diffraction study. *Phys. Chem. Miner.* **2020**. Vol. 47. P. 22.

Grew E.S., Belakovskiy D.I., Fleet M.E., Yates M.G., McGee J.J., Marquez N. Reedmergnerite and associated minerals from peralkaline pegmatite, Dara-i-Pioz, southern Tien Shan, Tajikistan. *Eur. J. Miner.* **1993**. Vol. 5. P. 971–984.

Griffen D.T., Ribbe P.H. Refinement of the crystal structure of celsian. *Amer. Miner.* **1976**. Vol. 61. P. 414–418.

Griffen D.T., Ribbe P.H., Gibbs G.V. The structure of slawsonite, a strontium analog of paracelsian. *Amer. Miner.* **1977**. Vol. 62. P. 31–35.

Gurzhiy V.V., Plášil J. Structural complexity of natural uranyl sulfates. *Acta Crystallogr.* **2019**. Vol. B75. P. 39–48.

Gurzhiy V.V., Kuporev I.V., Kovrugin V.M., Murashko M.N., Kasatkin A.V., Plášil J. Crystal chemistry and structural complexity of natural and synthetic uranyl selenites. *Crystals*. **2019**. Vol. 9. Paper 639.

Harlov D.E., Andrut M., Pöter B. Characterisation of buddingtonite $(NH_4)[AlSi_3O_8]$ and ND_4-buddingtonite $(ND_4)[AlSi_3O_8]$ using IR spectroscopy and Rietveld refinement of XRD spectra. *Phys. Chem. Miner*. **2001**. Vol. 28. P. 188–198.

Hautefeuille P., Perrey A. Sur la préparation et les propriétés d'orthose ferrique. *C. R. Acad. Sci. Paris*. **1888**. Vol. 107. P. 1150–1152.

Hsu L.S. Cymrite: new occurrence and stability. *Contrib. Miner. Petrol*. **1994.** Vol. 118. P. 314–320.

Hwang S.L., Shen P., Chu H.T., Yui T.F., Liou J.G., Sobolev N.V., Zhang R.Y., Shatsky V.S., Zayachkovsky A.A. Kokchetavite: A new polymorph of $KAlSi_3O_8$ from the Kokchetav UHP terrain. *Contrib. Miner. Petrol*. **2004**. Vol. 148. P. 380–389.

Hwang S.L., Shen P., Chu H.T., Yui T.-F., Liou J.G., Sobolev N.V. Kumdykolite, an orthorhombic polymorph of albite, from the Kokchetav ultrahigh-pressure massif, Kazakhstan. *Eur. J. Miner.* **2009**. Vol. 21. P. 1325–1334.

Ito J. High temperature solvent growth of anorthite on the join $CaAl_2Si_2O_8$–SiO_2. *Contrib. Miner. Petrol.* **1976**. Vol. 59. P. 187–194.

Jin S., Xu H. Study on structure variations of incommensurately modulated labradorite feldspars with different cooling histories. *Amer. Miner*. **2017**a. Vol. 102. P. 1328–1339.

Jin S., Xu H. Solved: The enigma of labradorite feldspar with incommensurately modulated structure. *Amer. Miner*. **2017**b. Vol. 102. P. 21–32.

Jin S., Xu H., Wang X., Zhang D., Jacobs R., Morgan D. The incommensurately modulated structures of volcanic plagioclase: Displacement, ordering and phase transition. *Acta Crystallogr*. **2019**. Vol. B75. P. 643–656.

Jin S., Xu H., Wang X., Jacobs R., Morgan D. The incommensurately modulated structures of low-temperature labradorite feldspars: A single-crystal X-ray and neutron diffraction study. *Acta Crystallogr*. **2020**. Vol. B76. P. 93–107.

Kanzaki M., Xue X., Amalberti J., Zhang Q. Raman and NMR spectroscopic characterization of high-pressure K-cymrite ($KAlSi_3O_8 \cdot H_2O$) and its anhydrous form (kokchetavite). *J. Miner. Petrol. Sci*. **2012**. Vol. 107. P. 114–119.

Kashaev A.A. The crystal structure of cymrite. *Dokl. Acad. Sci. USSR*. **1966**. Vol. 169. P. 201–203 (*in Russian*).

Khomyakov A.P., Rogachev D.L. Searlesite and reedmergnerite from the Lovozero alkaline massif. *Izv. Acad. Sci. USSR. Ser. Geol*. **1991**. N 11. P. 149–152 (*in Russian*).

Kimata M. Crystal structure of $KBSi_3O_8$ isostructural with danburite. *Miner. Mag*. **1993**. Vol. 57. P. 157–164.

Kimball M.R., Megaw H.D. Interim report on the crystal structure of buddingtonite. In: *The Feldspars. Proceedings of the NATO ASI on Feldspars*. Eds. W.S. MacKenzie and J. Zussman. Manchester University Press, Manchester, **1974**. P. 81–86.

Kotelnikov A.R., Ananiev V.V., Kovalsky A.M., Suk N.I. Synthesis of phosphorus- and arsenic-bearing framework silicates similar to feldspar. *Vestnik ONZ. RAN*. **2011**. Vol. 3. P. 6047 (*in Russian*).

Kotková J., Koda R., Machovi V. Kumdykolite from the ultrahigh-pressure granulite of the Bohemian Massif. *Amer. Miner.* **2014**. Vol. 99. P. 1798–1801.

Kremenović A., Norby P., Dimitrievič R., Dondur V. Time-temperature resolved synchrotron XRPD study of the hexacelsian $\alpha \leftrightarrow \beta$ polymorph inversion. *Solid State Ionics*. **1997**. Vol. 101. P. 611–618.

Krivovichev S.V. Topology of microporous structures. *Rev. Miner. Geochem*. **2005**. Vol. 57. P. 17–68.

Krivovichev S.V. Topological complexity of crystal structures: quantitative approach. *Acta Crystallogr*. **2012**. Vol. A68. P. 393–398.

Krivovichev S.V. Structural complexity of minerals: information storage and processing in the mineral world. *Miner. Mag.* **2013**a. Vol. 77. N 3. P. 275–326.

Krivovichev S.V. Structural and topological complexity of zeolites: An information-theoretic analysis. *Micropor. Mesopor. Mater*. **2013**b. Vol. 171. P. 223–229.

Krivovichev S.V. Which inorganic structures are the most complex? *Angew. Chem. Int. Ed*. **2014**a. Bd. 53. S. 654–661.

Krivovichev S.V. On the algorithmic complexity of crystals. *Miner. Mag.* **2014**b. Vol. 78. P. 415–435.

Krivovichev S.V. Structural complexity and configurational entropy of crystalline solids. *Acta Crystallogr*. **2016**a. Vol. B72. P. 274–276.

Krivovichev S.V. Structural complexity of minerals and mineral parageneses: Information and its evolution in the mineral world. In: *Highlights in Mineralogical Crystallography*. Eds. R. Danisi R. and T. Armbruster. Walter de Gruyter GmbH: Berlin, Germany; Boston, MA, USA. **2016**b. P. 31–73.

Krivovichev S.V. Structure description, interpretation and classification in mineralogical crystallography. *Crystallogr. Rev*. **2017**. Vol. 23. P. 2–71.

Krivovichev S.V. Ladders of information: What contributes to the structural complexity in inorganic crystals. *Z. Kristallogr*. **2018**. Vol. 233. P. 155–161.

Krivovichev S.V., Shcherbakova E.P., Nishanbaev T.P. The crystal structure of svyatoslavite and evolution of complexity during crystallization of a $CaAl_2Si_2O_8$ melt: A structural automata description. *Canad. Miner.* **2012**. Vol. 50. P. 585–592.

Kroll H., Ribbe P.H. Determining (Al,Si) distribution and strain in alkali feldspars using lattice parameters and diffraction-peak positions: a review. *Amer. Miner.* **1987**. Vol. 72. P. 491–506.

Kroll H., Bambauer H.-U., Schirmer U. The high albite-monalbite and analbite-monalbitetransitions. *Amer. Miner.* **1980**. Vol. 65. P. 1192–1211.

Kuehner S.M., Joswiak D.J. Naturally occurring ferric iron sanidine from the Leucite Hills lamproite. *Amer. Miner.* **1996**. Vol. 81. P. 229–237.

Kyono A., Kimata M. Refinement of the crystal structure of a synthetic non-stoichiometric Rb-feldspar. *Miner. Mag.* **2001**. Vol. 65. P. 523–531.

Langenhorst F., Poirier J.P. "Eclogitic" minerals in a shocked basaltic meteorite. *Earth Planet. Sci. Lett.* **2000**a. Vol. 176. P. 259–265.

Langenhorst F., Poirier J.P. Anatomy of black veins in Zagami: Clues to the formation of high-pressure phases. *Earth Planet. Sci. Lett.* **2000**b. Vol. 184. P. 37–55.

Lebedeva Y.S., Pushcharovsky D.Y., Pasero M., Merlino S., Kashaev A.A., Taroev V.K., Göttlicher J., Kroll H., Pentinghaus H., Suvorova L.F., Wulf-Bernodat H., Lashkevich V.V. Synthesis and crystal structure of low ferrialuminosilicate sanidine. *Crystallogr. Rep.* **2003.** Vol. 48. P. 919–924.

Li Q., Yang Z., Liao X., Li D., Cai D., Niu B., He P., Duan X., Jia D., Zhou Y. Insight into hexacelsian-to-celsian transformation in hot-pressed BN/BAS composites. *J. Eur. Ceram. Soc.* **2020**. Vol. 40. P. 1773–1778.

Lindbloom J.T., Gibbs G.V., Ribbe P.H. The crystal structure of hurlbutite: A comparison with danburite and anorthite. *Amer. Miner.* **1974**. Vol. 59. P. 1267–1271.

Linthout K., Lustenhouwer W. Ferrian high sanidine in a lamproite from Cancarix, Spain. *Miner. Mag.* **1993**. Vol. 57. P. 289–299.

Liu L.G. High-pressure phase transformations of albite, jadeite and nepheline. *Earth Planet. Sci. Lett.* **1978**. Vol. 37. P. 438–444.

Liu L.-G., El Goresy A. High-pressure phase transitions of the feldspars, and further characterization of lingunite. *Intern. Geol. Rev.* **2007**. Vol. 49. P. 854–860.

London D. Phosphorus in S-type magmas: the P_2O_5 content of feldspars from peraluminous granites, pegmatites and rhyolites. *Amer. Miner.* **1992**. Vol. 77. P. 126–145.

London D., Cerny P., Loomis J.L., Pan J.J. Phosphorus in alkali feldspars of rare-element granitic pegmatites. *Canad. Miner.* **1990**. Vol. 28. P. 771–786.

Loewenstein W. The distribution of aluminium in the tetrahedra of silicates and aluminates. *Amer. Miner.* **1954**. Vol. 39. P. 92–96.

Luaña V., Costales A., Mori-Sánchez P., Pendás A.M. Ions in crystals: The topology of the electron density in ionic materials. 4. The danburite ($CaB_2Si_2O_8$) case and the occurrence of oxide–oxide bond paths in crystals. *J. Phys. Chem. B.* **2003**. Vol. 107. P. 4912–4921.

Ma C., Krot A.N., Bizzarro M. Discovery of dmisteinbergite (hexagonal $CaAl_2Si_2O_8$) in the Allende meteorite: A new member of refractory silicates formed in the solar nebula. *Amer. Miner.* **2013**. Vol. 98. P. 1368–1371.

Ma C., Tschauner O., Beckett J.R., Rossman G.R., Prescher C., Prakapenka V.B., Bechtel H.A., MacDowell A. Liebermannite, $KAlSi_3O_8$, a new shock-metamorphic, high-pressure mineral from the Zagami Martian meteorite. *Meteor. Planet. Sci.* **2018**. Vol. 53. P. 50–61.

Maeda K., Yasumori A. Toughening of $CaO–Al_2O_3–SiO_2$ glass by dmisteinbergite precipitation. *Mater. Lett.* **2016**. Vol. 180. P. 231–234.

Maeda K., Yasumori A. Nucleation and growth of hexagonal $CaAl_2Si_2O_8$ crystals in $CaO–Al_2O_3–SiO_2$ glass. *Mater. Lett.* **2017**. Vol. 206. P. 241–244.

Maeda K., Iwasaki K., Urata S., Akatsuka K., Yasumori A. 3D microstructure and crack pathways of toughened $CaO–Al_2O_3–SiO_2$ glass by precipitation of hexagonal $CaAl_2Si_2O_8$ crystal. *J. Amer. Ceram. Soc.* **2019**. Vol. 102. P. 5535–5544.

Massonne H.-J. Evidence for low-temperature ultrapotassic siliceous fluids in subduction zone environments from experiments in the system $K_2O–MgO–Al_2O_3–SiO_2–H_2O$ (KMASH). *Lithos.* **1992**. Vol. 28. P. 421–434.

Matýsek D., Jirásek J. Occurrences of slawsonite in rocks of the teschenite association in the Podbeskydí Piedmont area (Czech Republic) and their petrological significance. *Canad. Miner.* **2016**. Vol. 54. P. 1129–1146.

McConnell J.D.C., De Vita A., Kenny S D., Heine V. Determination of the origin and magnitude of Al/Si ordering enthalpy in framework aluminosilicates from *ab initio* calculations. *Phys. Chem. Miner.* **1997**. Vol. 25. P. 15–23.

Megaw H.D. Order and disorder. I. Theory of stacking faults and diffraction maxima. *Proc. Royal Soc. London.* **1960**a. Vol. 259. P. 59–78.

Megaw H.D. Order and disorder. II. Theory of diffraction effects in the intermediate plagioclase feldspars. *Proc. Royal Soc. London.* **1960**b. Vol. 259. P. 159–183.

Megaw H.D. Order and disorder. III. The structure of the intermediate plagioclase feldspars. *Proc. Royal Soc. London*. **1960**c. Vol. 259. P. 184–202.

Megaw H.D. The architecture of the felspars. In: *The Feldpars.* Eds. *MacKenzie W.S., Zussman J.* Manchester University Press, Manchester, UK. **1974**. P. 1–24.

Merlino S. Okenite, $Ca_{10}Si_{18}O_{46} \cdot 18H_2O$: the first example of a chain sheet silicate. *Amer. Miner.* **1983**. Vol. 68. P. 614–622.

Mihailova I., Stavrakeva D. Synthesis of maleevite. *Dokl. Bulg. Acad. Sci*. **2005**. Vol. 58. P. 1069–1074.

Mikhno A.O., Schmidt U., Korsakov A.V. Origin of K-cymrite and kokchetavite in the polyphase mineral inclusions from Kokchetav UHP calc-silicate rocks: evidence from confocal Raman imaging. *Eur. J. Miner*. **2013**. Vol. 25. P. 807–816.

Mills S.J., Hatert F., Nickel E.H., Ferraris G. The standardisation of mineral group hierarchies: application to recent nomenclature proposals. *Eur. J. Miner.* **2009**. Vol. 21. P. 1073–1080.

Milton C., Axelrod J.M., Grimaldi F.S. New minerals, reedmergnerite ($Na_2O{\cdot}B_2O_3 \cdot 6SiO_2$) and eitelite ($Na_2O{\cdot}MgO \cdot 2CO_2$) associated with leucosphenite, shortite, searlesite, and crocidolite in the Green River formation, Utah. *Amer. Miner*. **1955**. Vol. 40. P. 326–327.

Milton C., Chao E.C.T., Axelrod J.M., Grimaldi F.S. Reedmergnerite, $NaBSi_3O_8$, the boron analogue of albite, from the Green River formation, Utah. *Amer. Miner*. **1960**. Vol. 45. P. 188–199.

Minerals. Vol. 1. Framework Silicates, Issue 1. Silicates with broken frameworks. Feldspars. Ed. *By Bokij G. B. and Borutsky B. E. Moscow*: Nauka, **2003**. 583 p. (*in Russian*).

Mittempergher S., Dallai L., Pennacchioni G., Renard F., Di Toro G. Origin of hydrous fluids at seismogenic depth: Constraints from natural and experimental fault rocks. *Earth Planet. Sci. Lett*. **2014**. Vol. 385. P. 97–109.

Mookherjee M., Redfern S.A.T., Swainson I., Harlov D.E. Low-temperature behaviour of ammonium ion in buddingtonite $[N(D,H)_4AlSi_3O_8]$ from neutron powder diffraction. *Phys. Chem. Miner*. **2004**. Vol. 31. P. 643–649.

Mookherjee M., Welch M. D., Le Pollès L., Redfern S.A.T., Harlov D.E. Ammonium ion behaviour in feldspar: Variable-temperature infrared and ^{2H}NMR studies of synthetic buddingtonite, $N(D,H)_4AlSi_3O_8$. *Phys. Chem. Miner*. **2005**. Vol. 32. P. 126–131.

Mori H. Hollandite type $NaAlSi_3O_8$ in shocked meteorites. In: *31st High Pressure Conf. Japan Soc. High Press. Sci. Technol*. Osaka, Japan, **1990.** P. 134–135.

Mori H. Shock-induced phase transformations of the Earth and planetary materials. *J. Miner. Soc. Japan*. **1994**. Vol. 23. P. 171–178.

Morse J.W., Casey W.H. Ostwald processes and mineral paragenesis in sediments. *Amer. J. Sci*. **1988**. Vol. 288. P. 537–560.

Mrose M. Hurlbutite, $CaBe_2(PO_4)_2$, a new mineral. *Amer. Miner*. **1952**. Vol. 37. P. 931–940.

Müller W.F. Phase transitions and associated domains in hexacelsian ($BaAl_2Si_2O_8$). *Phys. Chem. Miner*. **1977**. Vol. 1. P. 71–82.

Müller G. Preparation of hydrogen and lithium feldspars by ion exchange. *Nature*. **1988**. Vol. 332. P. 435–436.

Nadezhina T.N., Pushcharovsky D.Y., Taroev V.K., Tauson V.L., Bychkov A.M. Crystal structure of a low sanidine ferroalumosilicate. *Crystallogr. Rep.* **1993**. Vol. 38. P. 753–758.

Navrotsky A. Energetic clues to pathways to biomineralization: precursors, clusters, and nanoparticles. *Proc. Natl. Acad. Sci. USA*. **2004**. Vol. 101. P. 12096–12101.

Németh P., Lehner S.W., Petaev M.I., Buseck P. Kumdykolite, a high-temperature feldspar from an enstatite chondrite. *Amer. Miner.* **2013**. Vol. 98. P. 1070–1073.

Nestola F., Mittempergher S., Toro G.D., Zorzi F., Pedron D. Evidence of dmisteinbergite (hexagonal form of $CaAl_2Si_2O_8$) in pseudotachylyte: A tool to constrain the thermal history of a seismic event. *Amer. Miner.* **2010**. Vol. 95. P. 405–409.

Newnham R.E., Megaw H.D. The crystal structure of celsian (barium felspar). *Acta Crystallogr.* **1960**. Vol. 13. P. 303–313.

Nickel E.H., Grice J.D. The IMA Commission on New Minerals and Mineral Names: Procedures and guidelines on mineral nomenclature. *Canad. Miner*. **1998**. Vol. 36. P. 17–18.

Ostwald W. Studien über die Bildung und Umwandlung fester Körper. *Z. Physik. Chem*. **1897**. Bd. 22. S. 289–330.

Pakhomova A., Bykova E., Bykov M., Glazyrin K., Gasharova B., Liermann H.-P., Mezouar M., Gorelova L., Krivovichev S., Dubrovinsky L. A closer look into close packing: pentacoordinated silicon in a high-pressure polymorph of danburite. *IUCrJ*. **2017**. Vol. 4. P. 671–677.

Pakhomova A., Aprilis G., Bykov M., Gorelova L., Krivovichev S.V., Belov M.P., Abrikosov I.A., Dubrovinsky L.S. Penta- and hexa-coordinated beryllium and phosphorus in high-pressure modifications of $CaBe_2P_2O_8$. *Nature Commun*. **2019**. Vol. 10. P. 2800.

Pakhomova A., Simonova D., Koemets I., Koemets E., Aprilis G., Bykov M., Gorelova L., Fedotenko T., Prakapenka V., Dubrovinsky L. Polymorphism of feldspars above 10 GPa. *Nature Commun*. **2020**. Vol. 11. P. 2721.

Pautov L.A., Agakhanov A.A., Sokolova E., Hawthorne F.C. Maleevite, $BaB_2Si_2O_8$, and pekovite, $SrB_2Si_2O_8$, new mineral species from the Dara-I-Pioz Alkaline Massif, northern Tajikistan: description and crystal structure. *Canad. Miner*. **2004**. Vol. 42. P. 107–119.

Pekov I.V., Kononkova N.N. Rubidium mineralization in rare-element granitic pegmatites of the Voron'i tundras, Kola Peninsula, Russia. *Geochem. Int.* **2010**. Vol. 48. P. 695–713.

Perraki M., Faryad S.W. First finding of microdiamond, coesite and other UHP phases in felsic granulites in the Moldanubian Zone: Implications for deep subduction and a revised geodynamic model for Variscan Orogeny in the Bohemian Massif. *Lithos*. **2014**. Vol. 202. P. 157–166.

Phillips M.W., Gibbs G.V., Ribbe P.H. The crystal structure of danburite: A comparison with anorthite, albite, reedmergnerite. *Amer. Miner*. **1974**. Vol. 59. P. 79–85.

Rao C., Wang R., Hatert F., Gu X., Ottolini L., Hu H., Dong C., Dal Bo F., Baijot M. Strontiohurlbutite, $SrBe_2(PO_4)_2$, a new mineral from Nanping No. 31 pegmatite, Fujian Province, Southeastern China. *Amer. Mineral*. **2014**. Vol. 99. P. 494–499.

Rao C., Hatert F., Wang R.C., Gu X.P., Dal Bo F., Dong C.W. Minjiangite, $BaBe_2(PO_4)_2$, a new mineral from Nanping No. 31 pegmatite, Fujian Province, southeastern China. *Miner. Mag*. **2015**. Vol. 79. P. 1195–1202.

Redfern S.A.T. Length scale dependence of high-pressure amorphization: the static amorphization of anorthite. *Miner. Mag*. **1996**. Vol. 60. P. 493–498.

Ribbe P.H. Chemistry, structure and nomenclature of feldspars. *Rev. Miner*. **1983**a. Vol. 2. P. 1–20.

Ribbe P.H. Aluminum-silicon order in feldspars; domain textures and diffraction patterns. *Rev. Miner*. **1983**b. Vol. 2. P. 21–56.

Ribbe P.H. The crystal structures of the aluminium-silicate feldspars. In: *Feldspars and Their Reactions*. Ed. by *Parsons I.* Dordrecht: Kluwer Academic Publishers, **1994**. P. 1–50.

Ringwood A.E., Reid A.F., Wadsley A.D. High-pressure $KAlSi_3O_8$, an aluminosilicate with sixfold coordination. *Acta Crystallogr.* **1967**. Vol. 23. P. 1093–1095.

Salje E.K.H. Phase transitions and vibrational spectroscopy in feldspars. In: *Feldspars and Their Reactions*. Ed. by *Parsons I.* Dordrecht: Kluwer Academic Publishers, **1994**. P. 103–160.

Seki Y., Kennedy G.C. The breakdown of potassium feldspar, $KAlSi_3O_8$, at high temperatures and high pressures. *Amer. Miner*. **1964**. Vol. 49. P. 1688–1706.

Shchipalkina N.V., Pekov I.V., Britvin S.N., Koshlyakova N.N., Vigasina M.F., Sidorov E.G. A new mineral ferrisanidine, $K[Fe^{3+}Si_3O_8]$, the first natural feldspar with species-defining iron. *Minerals*. **2019**. Vol. 9. Paper 770.

Shchipalkina N.V., Pekov I.V., Britvin S.N., Koshlyakova N.N., Sidorov E.G. Arsenic and phosphorus in feldspar framework: sanidine–filatovite solid solution series from fumarolic exhalations of the Tolbachik volcano, Kamchatka, Russia. *Phys. Chem. Miner*. **2020**. Vol. 47. P. 1.

Simakin A.G., Eremyashev V.E., Kucherinenko Y.V. New data on dmisteinbergite. *Zapiski RMO* (*Proc. Russian Miner. Soc.*). **2010**. Vol. 139. N 3. P. 102–108 (*in Russian*).

Sims M., Jaret S.J., Carl E.-R., Rhymer B., Schrodt N., Mohrholz V., Smith J., Konopkova Z., Liermann H.-P., Glotch T.D., Ehm L. Pressure-induced amorphization in plagioclase feldspars: A time-resolved powder diffraction study during rapid compression. *Earth Planet. Sci. Lett*. **2019**. Vol. 507. P. 166–174.

Simpson D.R. Aluminum phosphate variants of feldspar. *Amer. Miner.* **1977**. Vol. 62. P. 351–355.

Smith J.V. The crystal structure of paracelsian, $BaAl_2Si_2O_8$. *Acta Crystallogr*. **1953**. Vol. 6. P. 613–620.

Smith J.V. Further discussion of framework structures formed from parallel four-and eight-membered rings. *Miner. Mag*. **1968**. Vol. 33. P. 202–212.

Smith J.V. Feldspar Minerals. I. Crystal Structure and Physical Properties. Berlin: Springer-Verlag, **1974**. 627 p.

Smith J.V. Enumeration of 4-connected 3-dimensional nets and classification of framework silicates. II. Perpendicular and near-perpendicular linkages from 4.8^2, 3.12^2 and 4.6.12 nets. *Amer. Miner*. **1978**. Vol. 63. P. 960–969.

Smith J.V., Brown W.L. Feldspar Minerals. Vol. 1. Crystal Structures, Physical, Chemical and Microstructural Properties. Berlin Heidelberg: Springer Verlag, **1988**. 828 p.

Smith J.V., Rinaldi F. Framework structures formed from parallel four- and eight-membered rings. *Miner. Mag*. **1962**. Vol. 33. P. 202–212.

Smith W.C., Bonnister F.A., Hey M.N. Cymrite, a new barium mineral from the Benallt manganese mine, Rhiw, Carnarvonshire. *Miner. Mag*. **1949.** Vol. 28. P. 676–681.

Sokol A.G., Kupriyanov I.N., Seryotkin Y.V., Sokol E.V., Kruk A.N., Tomilenko A.A., Bul'bak T.A., Palyanov Y.N. Cymrite as mineral clathrate: an overlooked redox insensitive transporter of nitrogen in the mantle. *Gondwana Res*. **2020**. Vol. 79. P. 70–86.

Sorokhtina N.V., Chukanov N.V., Voloshin A.V., Pakhomovsky Y.A., Bogdanova A.N., Moiseev M.M. Cymrite as an indicator of high barium activity in the formation of hydrothermal rocks related to carbonatites of the Kola Peninsula. *Geol. Ore Deposits*. **2008**. Vol. 50. P. 620–628.

Sugiyama K., Takéuchi Y. Unusual thermal expansion of a B-O-bond in the structure of danburite $CaB_2Si_2O_8$. *Z. Kristallogr*. **1985**. Vol. 173. P. 293–304.

Tagai T., Hoshi T., Suzuki M., Kato A., Matsubara S. A new modification of slawsonite, $SrAl_2Si_2O_8$: its structure and phase transition. *Z. Kristallogr. NCS*. **1995**. Vol. 210. P. 741–745.

Taiji M., Yoshiaki G. Synthesis of monoclinic celsian from Ba-exchanged zeolite A. *J. Ceram. Soc. Japan*. **2002**. Vol. 110. P. 163–166.

Takeuchi Y., Donnay G. The crystal structure of hexagonal $CaAl_2Si_2O_8$. *Acta Crystallogr.* **1959**. Vol. 12. P. 465–470.

Takéuchi Y., Haga N., Ito J. The crystal structure of monoclinic $CaAl_2Si_2O_8$: A case of monoclinic structure closely simulating orthorhombic symmetry. *Z. Kristallogr.* **1973**. Bd. 137. S. 380–398.

Taroev V., Göttlicher J., Kroll H., Kashaev A., Suvorova L., Pentinghaus H., Bernodat-Wulf H., Breit U., Tauson V., Lashkevich V. Synthesis and structural state of K-feldspars in the system $K[AlSi_3O_8]$–$K[FeSi_3O_8]$. *Eur. J. Miner.* **2008**. Vol. 20. P. 635–651.

Taylor W.H. The structure of sanidine and other feldspars. *Z. Kristallogr.* **1933**. Bd. 85. S. 425–442.

Teertstra D.K., Cerny P., Hawthorne F.C. Rubidium-rich feldspars in a granitic pegmatite from the Kola peninsula, Russia. *Can. Miner.* **1997**. Vol. 35. P. 1277–1281.

Teerstra D.K., Cerny P., Hawthorne F.C., Pier J., Wang Lu-Min, Ewing R.C. Rubicline, a new feldspar from San Piero in Campo, Elba, Italy. *Amer. Miner.* **1998**a. Vol. 83. P. 1335–1339.

Teertstra D.K., Cerny P., Hawthorne F.C. Rubidium feldspars in granitic pegmatites. *Canad. Miner.* **1998**b. Vol. 36. P. 483–496.

Thompson P., Parsons I., Graham C. M., Jackson B. The breakdown of potassium feldspar at high water pressures. *Contrib. Miner. Petrol.* **1988**. Vol. 130. P. 176–186.

Tomioka N., Kondo H., Kunikata A., Nagai T. Pressure-induced amorphiza- tion of albitic plagioclase in an externally heated diamond anvil cell. *Geophys. Res. Lett.* **2010**. Vol. 37. Paper L21301.

Tschauner O., Ma C. Stöfflerite, IMA 2017-062. CNMNC Newsletter No. 39, October 2017. *Miner. Mag.* **2017**. Vol. 81. P. 1285.

Tschermak G. Die Meteoriten von Shergotty und Gopalpur. *Sitzber. Akad. Wiss. Wien Math.-Naturwiss. Kl. Abt. I.* **1872**. Bd. 65. S. 122–146.

Tschermak G. Beitrag zur Klassifikation der Meteoriten. *Sitzber. Akad. Wiss. Wien Math.-Naturwiss. Kl. Abt. I.* **1883**. Bd. 88. S. 347–371.

Tutti F. Formation of end-member $NaAlSi_3O_8$ hollandite-type structure (lingunite) in diamond anvil cell. *Phys. Earth Planet Int.* **2007**. Vol. 161. P. 143–149.

Tyumentseva O.S., Kornyakov I.V., Britvin S.N., Zolotarev A.A., Gurzhiy V.V. Crystallographic insights into uranyl sulfate minerals formation: Synthesis and crystal structures of three novel cesium uranyl sulfates. *Crystals.* **2019**. Vol. 9. Paper 660.

Vennari C.E., O"Bannon E.F., Williams Q. The ammonium ion in a silicate under compression: infrared spectroscopy and powder X-ray diffraction of $NH_4AlSi_3O_8$-buddingtonite to 30 GPa. *Phys. Chem. Miner.* **2017**. Vol. 44. P. 149–161.

Vergasova L.P., Krivovichev S.V., Britvin S.N., Burns P.C., Ananiev V.V. Filatovite, $K[(Al,Zn)_2(As,Si)_2O_8]$, a new mineral species from the Tolbachik volcano, Kamchatka peninsula, Russia. *Eur. J. Miner.* **2004**. Vol. 16. P. 533–536.

Verstegen J.M. P.J., Ter Vrugt J.W., Wanmaker W.L. Luminescence of Eu^{2+}-activated $SrB_2Si_2O_8$. *J. Inorg. Nucl. Chem.* **1972**. Vol. 34. P. 3588–3589.

Voncken J.H.L., Konings R.J.M., Jansen J.B.H., Woensdregt C.F. Hydrothermally grown buddingtonite, an anhydrous ammonium feldspar ($NH_4AlSi_3O_8$). *Phys. Chem. Miner.* **1988**. Vol. 15. P. 323–328.

Voncken J.H.L., Van Roermund H.L.M., Van Der Eerden A.M.J., Jansen J.B.H., Erd R.C. Holotype buddingtonite: An ammonium feldspar without zeolitic H_2O. *Amer. Miner.* **1993**. Vol. 78. P. 204–209.

Wadoski-Romeijn E., Armbruster T. Topotactic transformation and dehydration of the zeolite gismondine to a novel Ca feldspar structure, *Amer. Miner.* **2013**. Vol. 98. P. 1988–1997.

Wainwright J.E., Starkey J. A refinement of the structure of anorthite. *Z. Kristallogr.* **1971**. Bd. 133. S. 75–84.

Winter J.K., Okamura F.P., Ghose S. A high-temperature structural study of high albite, monalbite, and the analbite → monalbite phase transition. *Amer. Miner.* **1979**. Vol. 64. P. 409–423.

Wietze R., Wiswanathan K. Rubidium-plagioklas durch Kationenaustauch. *Fortschr. Miner.* **1971**. Bd. 49. S. 63.

Wones D.R., Appleman D.E. Properties of synthetic triclinic $KFeSi_3O_8$, iron-microcline, with some observations on the iron-microcline ⇋ iron-sanidine transition. *J. Petrol.* **1963**. Vol. 4. P. 131–137.

Wu X., Meng D., Han, Y. Occurrence of "monalbite" in nature: a TEM study. *Earth Planet. Sci. Lett.* **2004**. Vol. 222. P. 235–241.

Xu H. Direct observation of Ca–Na ordering and structure polarity in Ca-rich intermediate plagioclase feldspar with incommensurate modulated structure. *Amer. Miner.* **2015**. Vol. 100. P. 510–515.

Xu Z., Shull J.L., Kriven W.M. Hot-stage transmission electron microscopy study of phase transformations in hexacelsian ($BaAl_2Si_2O_8$). *J. Mater. Res.* **2002**. Vol. 17. P. 1287–1297.

Xu H., Jin S., Noll B.C. Incommensurate density modulation in a Na-rich plagioclase feldspar: Z-contrast imaging and single-crystal X-ray diffraction study. *Acta Crystallogr.* **2016**. Vol. B72. P. 904–915.

Xu H., Jin S., Lee S., Hobbs F.W.C. Nano-phase $KNa(Si_6Al_2)O_{16}$ in adularia: a new member in the alkali feldspar series with ordered K–Na distribution. *Minerals.* **2019**. Vol. 9. P. 649.

Yamada H., Matsui Y., Ito E. Crystal-chemical characterization of $KAlSi_3O_8$ with the hollandite structure. *Mineral. J.* **1984**. Vol. 12. P. 29–34.

Zhang J., Ko J., Hazen R.M., Prewitt C.T. High-pressure crystal chemistry of $KAlSi_3O_8$ hollandite. *Am. Miner.* **1993**. Vol. 78. P. 493–499.

Zolotarev A.A., Krivovichev S.V., Panikorovskii T.L., Gurzhiy V.V., Bocharov V.N., Rassomakhin M.A. Dmisteinbergite, $CaAl_2Si_2O_8$, a metastable polymorph of anorthite: crystal-structure and Raman spectroscopic study of the holotype specimen. *Minerals.* **2019**. Vol. 9. Paper 570.

ПОЛИМОРФИЗМ ПОЛЕВЫХ ШПАТОВ: РАЗНООБРАЗИЕ, СЛОЖНОСТЬ, СТАБИЛЬНОСТЬ

д. чл. С. В. Кривовичев[a, b, *]

[a] *Центр наноматериаловедения, Кольский научный центр, Российская академия наук, ул. Ферсмана, 14, Апатиты, 184209 Россия*

[b] *Кафедра кристаллографии, Институт наук о Земле, Санкт-Петербургский государственный университет, Университетская наб., 7/9, Санкт-Петербург, 199034 Россия*

**e-mail: s.krivovichev@ksc.ru*

Поступила в редакцию 26.05.2020 г.
После доработки 11.06.2020 г.
Принята к публикации 17.06.2020 г.

Рассмотрены различные аспекты полиморфизма в семействе полевых шпатов с особым акцентом на структурное разнообразие и сложность полиморфов. Семейство полевых шпатов определено как состоящее из минералов и неназванных или носящих условные названия минеральных фаз с общей формулой $M^{n+}[T_4^{k+}O_8]$, где n – средний заряд катиона M^{n+} (n = 1–2; $M^{n+} = Na^+$, K^+, Rb^+, $(NH_4)^+$, Ca^{2+}, Sr^{2+}, Ba^{2+}), k – средний заряд катиона T^{k+} ($k = 4 - n/4$; $T^{k+} = Be^{2+}$, Zn^{2+}, Al^{3+}, B^{3+}, Fe^{3+}, Si^{4+}, As^{5+}, P^{5+}). К семейству полевых шпатов в настоящее время принадлежат 29 минеральных видов. Маскелинит является природным рентгеноаморфным (стеклообразным) полиморфом с плагиоклазовым составом. Все полиморфы полевых шпатов разделяются на две группы: с атомами T в исключительно тетраэдрической координации и те, которые содержат атомы T в нететраэдрической координации. Известны всего четыре топологии тетраэдрических мотивов в полевошпатовых структурах: **fsp** (трехмерные каркасы; полевые шпаты *sensu stricto*; 11 минеральных видов), **pcl** (трехмерные каркасы; парацельзиан; семь минеральных видов), **bct** (трехмерные каркасы, святославит; два минеральных вида), **dms** (двумерные слои; дмиштейнбергит; шесть минеральных видов). Известно три минерала, содержащих атомы T в исключительно октаэдрической координации и кристаллизующиеся в структурном типе голландита. Высокобарический полиморфизм структур с топологиями **fsp** и **pcl** обусловлен их особенностями, определяющими эти топологии как жесткую и гибкую, соответственно. Анализ структурной сложности полевошпатовых структур с использованием теории информации Шеннона указывает на существование следующих общих трендов: (i) структурная сложность понижается с повышением температуры; (ii) кинетически стабилизированные метастабильные фазы топологически более просты по сравнению с термодинамически стабильными фазами; (iii) высокобарическое поведение полевошпатовых структур не имеет ярко выраженных трендов в изменении структурной сложности. Полиморфзм в полевошпатовых структурах включает следующие кристаллохимические явления: (i) изменение координации внутри- и внекаркасных катионов; (ii) топологические реконструкции, включая изменения размерности структурных комплексов; (iii) катионное упорядочение, включая Al/Si и M-катионное упорядочение твердых растворов, приводящее к химической стабилизации отдельных структурных типов и образованию несоразмерно модулированных структур в плагиоклазах; (iv) диспласивные перестройки, включающие повороты тетраэдров и цепочек типа карданных валов; (v) аморфизация. Наблюдаемые кристаллохимические явления контролируются температурой, давлением (включая шоковые воздействия) и кинетикой кристаллизации, приводящей к появлению метастабильных фаз с уникальной структурной архитектурой.

Ключевые слова: полевой шпат, кристаллическая структура, полиморфизм, структурная сложность, фазовый переход, метастабильность, структурная топология, высокие давления, высокие температуры